From the parametric amplification in Electric Force Microscopy to the Scanning Gate Microscoppy of Quantum Rings

Frederico Martins

THÈSE

pour obtenir le grade de

Docteur de l'Université Joseph Fourier - Grenoble 1
Spécialité : Physique / Physique des Materiaux

par

Frederico MARTINS

présentée et soutenue publiquement le 4 Février 2008

De l'amplification paramétrique en microscopie à force électrique à la microscopie à grille locale d'anneaux quantiques

Institut Néel - CNRS / UJF

Composition du jury:

Présidente:	Margarida Godinho
Rapporteurs:	Giancarlo Faini
	Thierry Mélin
Examinateur:	Kunteah Khang
Invité:	Benoit Hackens
Directeurs de thèse:	Joël Chevier
	Serge Huant

Acknowledgment

This manuscript marks the end of a period of four years of my personal research work. It also marks the end of my stay in Grenoble. During this time I met many people that, for a reason of space, I cannot thank individually. Most of these people I will, most probably, never see again. Therefore, I think it is fair to start my acknowledgments by thanking them. They were in many ways my family and my support away from Portugal.

I also have to pay tribute to this city and to this country. The unique young international environment can only be possible in a city like Grenoble and I think that the best way to thank this country is to confess that part of me is now french.

During the period of my thesis I had the pleasure to be part of a team and to work with several people, with whom I obviously share the results. I strongly believe that the good outcome was a result of the excellent relationship within the group. In this section, I will thank these people individually.

The first responsible for this project are the leaders of the group, and simultaneously my thesis advisors, Serge Huant and Joël Chevrier. I wish to thank them for offering me the opportunity to work in such a good environment and for their constant support. In particular, I wish to thank Joël for oppening the door when I first came to Grenoble. To Serge, I wish to thank his patience, his daily guidance and, specially, all the advices and encouragement during the difficult periods.

I am also very grateful to all the people I worked with.

In the beginning of my thesis I worked with Martin Stark. During this period we set the basis of the low temperature microscope. His initial input was fundamental. I thank his friendship, his generosity and his scientific advices.

I also want to thank Thierry Ouisse for his constant scientific support, his culture and his 'difficult' questions. Most of our results were obtained while 'fighting' his questions. Moreover, frequently, it was Thierry himself bringing the solution to the 'difficult' questions.

Many thanks to Jean-François Motte. When nothing works, or

when you do a big mistake, there is always Jeff to save you. His constant good mood, his experience and his dynamism are priceless. He also contributed a lot to the design and to the assembling of the microscope.

Most of the experiments presented here (and also the best results) were done together with Benoit Hackens. We spent (alone) several months working over the night and weekends. During these nights we debated many subjects (not always scientific) and we built a solid friendship. If you can chose one person to work with, that person is Benoit. He is the perfect partner. I thank Benoit for all that he contributed to this thesis.

I would also like to thank Vincent Bayot for his brainstorms and for his very good advises, Marco Pala that never hesitated to collaborate with us and my office mate Hermman Sellier for the scientific debates. The substrate used in our experiments were kindly offered by the research group from the IEMN lab (Lille), Xavier Wallart, Sylvain Bollaert and Alain Cappy.

I am also very grateful to the other students and post-docs that I crossed paths with during my PhD: Michael Nasse, Nicolas Chevalier, Aurellien Cuche, Paolo Actis (l'Italien irreductible), Florian Habrard, Wilfrid Schwartz, Alexis Mosset, Alessandro Siria and Guillaume Jourdan.

Spectial thanks is due to Yannic Sonnefraud, Mario Rodrigues, Michal Hrouzek and Miguel Silveira that are much more than colleagues. They are good friends.

At last, I would like to thank the members of the jury Prof. Margarida Godinho, Dr. Giancarlo Faini, Dr. Thierry Mélin, Prof. Kuntheak Kheng and Benoit Hackens for having accepted the task. To Prof. Godinho I also want to thank for sending me to Grenoble in the first place.

I could not finish without thanking to my very best friend Rodrigo, that is always there no matter what, and to my family. To my family there is not much to say because they know me. Nothing would possible without them. Even far away from home they always care, and I cannot hide that I only feel home when I am with them.

I wish to dedicate this thesis to my parents, my sister, my grandmother and my beautiful nephew.

Résumé

La réduction de taille des dispositifs électroniques apporte de nouvelles exigences scientifiques et techniques. De nouveaux phénomènes apparaissent aux petites échelles et, par ailleurs, l'exploration des propriétés électroniques à l'échelle locale nécessite le développement d'instruments adaptés. Ces deux demandes sont devenues cruciales pour le développement de la 'nano-électronique'.

L'objectif de cette thèse est double : augmenter la sensibilité de détection de charges déposées sur des surfaces et l'imagerie dans l'espace réel des fonctions d'onde électroniques dans des nano-dispositifs enterrés sous la surface libre. Pour atteindre ces objectifs, nous avons concu un microscope à force atomique (AFM) idoine. Ce microscope est décrit dans le premier chapitre de ce mémoire.

Dans un deuxième chapitre, nous décrivons une méthode d'amplification paramétrique pour augmenter la sensibilité de détection de charges déposées sur une surface. Le mouvement du micro-levier AFM est déterminé analytiquement et est confirmé tant par une approche numérique que par l'expérience. Nous concluons qu'avec notre méthode, la limite de bruit thermique peut etre dépassée. Dans le meme chapitre, nous faisons une remarque sur une variante très répandue de la microscopie à force électrique (EFM) : la microscopie à force de Kelvin (KFM). Nous montrons que, meme si elle n'est pas volontairement provoquée, l'amplification paramétrique du mouvement du micro-levier est toujours présente et qu'elle peut notablement modifier la résolution du microscope telle qu'anticipée à travers les approches usuelles.

Dans le dernier chapitre, nous nous intéressons au transport électronique dans des systémes mésoscopiques fabriqués à partir de gaz électroniques 2D. Traditionnellement, l'étude de ce transport est appréhendée par des mesures de conductance à 4 points en fonction de la température. Cette approche procure une information moyennée sur toute la taille du dispositif et, donc, perd l'information locale. Ici, nous complétons cette approche par des mesures dans lesquelles la pointe du microscope AFM est polarisée électriquement de sorte à perturber localement le potentiel vu par les porteurs de charge. Le balayage de

cette pointe au dessus du dispositif permet d'en construire une image de sa conductance. Cette technique est appelée 'microscopie locale à grille ajustable' et est désignée par son acronyme anglo-saxon : SGM. Nous avons ici étudié un système modèle, siège d'interférences quantiques de type Aharonov-Bohm : des anneaux quantiques fabriqués à partir d'hérérostructures à base de GaInAs. Nous couplons nos expériences à des simulations en mécanique quantique et montrons comment la microscopie SGM permet de sonder le transport cohérent et d'imager les fonctions d'onde dans ces anneaux.

Abstract

The continuous size reduction of electronic devices have brought new technical and scientific demands. Firstly, because new peculiar physical effects appear at small scales. Secondly, probing electronic properties at the local scale requires new adapted instrumentation. These two issues have become crucial to the development of the so-called nano-electronics.

The objective of this thesis is two fold: enhancing the sensitivity of charge detection deposed over surfaces and the real-space imaging of the wave-function inside buried open nano-devices. To achieve these goals we have conceived a low temperature Atomic Force Microscope (AFM) adapted to study electrical properties over surfaces. In the first chapter of this thesis we describe the operation of the AFM and the technical options.

In the second chapter, we describe a parametric method to increase the sensitivity of an AFM to deposed charges over a surface. The movement of the AFM probe is described analytically which is confirmed by numerical solutions and experiments. We conclude that with such a method the thermal noise limit can be beaten. In the same chapter, we make a remark concerning a widespread technique: the Kelvin Force Microscopy (KFM). We show that, in this case, and even if it is not intentional, parametric effect is always present which might substantially change the expected resolution calculated from classical approaches.

In the third and last chapter, we address the electronic transport in mesoscopic systems fabricated from two-dimensional electron gases (2DEGs). Traditionally, this kind of samples are characterized with four-point conductance measurements at low temperature. This technique provides information which is averaged over the size of the whole device and, as such, losses the local information. Here, we complement this analysis using the AFM probe as a polarized moving gate that induces a local perturbation of the potential experienced by the 2DEG. As the tip is scanned over the surface, a conductance map is built. This technique is called Scanning Gate Microscopy (SGM). So far, only a limited number of SGM experiments were performed. Here, we use

a model sample fabricated from InGaAs heterostructure: a quantum ring (QR). By coupling experiments and quantum mechanical simulations we conclude that SGM permits probing the coherent transport and imaging the electronic probability density inside the QR.

Contents

Chapter 1

Introduction

Electronic devices are everywhere in our daily life. We can find them inside complex tools like mobile phones or laptops, but also in simple instruments such as home digital thermometers, cloths irons or ovens. Nowadays, industries fight hard to reduce their size.

Nevertheless, it is my experience that these technological and scientific efforts are not quite understood by most of the people. Indeed, if we open, *e.g.*, a laptop we realize that most of the space is taken by the hard disc, the battery, the keyboard and the screen. A less attentive regard would suggest that small circuits are only relevant in applications where dimensions are critical.

This common belief is not accurate, the truth is that smaller circuits consume, in general, less energy and are faster. These two reasons are at least more important than the compactness of the circuits. Indeed, at the end of the last century we became aware that traditional sources of energy not only pollute but are also limited. Nowadays, the scientific community is very active to find solutions. Today it is believed that the only way to keep our lifestyle is to find new renewable clean sources of energy and to build more efficient tools. By efficient we mean doing more operations while consuming less energy.

Therefore, modern electronic nano-devices are dealing with an ever reduced number of current carrying and interacting electrons. The experimental assessment of the number of charges transiting through structures, the localisation of their wave-functions and the manipulation and detection of single charges, all constitute important issues with respect to the long-term development of nano-electronics. The study of their quantum-coherent behaviour is of particular importance since it is anticipated to provide new concepts and new designs of electron devices.

This thesis is dedicated to provide new methods to analyze elec-

tronic nano-circuits. We have addressed two subjects: enhancing the sensitivity of charge detection and real-space imaging of the wave-function inside buried open nano-devices. To achieve this goal, we have established a low temperature atomic force microscope (AFM) where the local metallic nano-probe permits direct access to the local electronic properties. Several examples exist in literature demonstrating the AFM performances concerning charge detection [1][2]. As explained in Chapter 1, we have re-designed the head of a commercial low temperature AFM system [3][4] to be adapted to our experimental needs. In this chapter, we start by explaining the general operation mode of an AFM and the theoretical limitations. Afterwards we present our experimental setup and the modified low temperature AFM. The options are discussed and we analyze its performance. This system is at the heart of the research work presented afterwards.

In Chapter 2 we propose a method to beat the thermal noise limit while detecting excess charges deposed over a surface. This method consists in using a parametric excitation to increase the sensitivity of fixed charges over samples. This effect is not new. It has been known for centuries, *e.g.* the *Botafumeiro* in Santiago de Compostela (13^{th} century) [5], and it has been used in several scientific domains, *e.g* [6]. Here the originality is to make use of this effect to detect charges. We propose an analytical model to describe the movement of the cantilever when the tip probes electrostatic forces under the effect of parametric excitation. These results are crosschecked by numerical solutions and confirmed by experiments. In this chapter we discuss the value of the parameters in which the system should be set so that one can be in the best measurement conditions.

Later, in the same chapter, we make a remark concerning a common method used in charge detection: the Kelvin force microscopy (KFM). We show that in this technique the parametric effect is always present and can even become dominant. Moreover, we found that setting it in certain conditions one can either profit from the parametric effect or lose sensitivity. The complete understanding is therefore important and we conclude that, in most situations, this effect cannot be neglected.

In Chapter 3 we focus on mesoscopic samples based on two-dimensional electron gases (2DEGs) buried under surfaces. Here, we use the AFM probe as a flying gate to locally perturb the electronic current flowing through the device. This recent research technique is know in literature as Scanning Gate Microscopy (SGM). For the time being, only a few number of devices were studied and several aspects remain to be explored. Furthermore, up to now no analysis has been developed permitting a correspondence between features observed in SGM imaging

and the electron wavefunctions inside a nanostructure. In this chapter, our aim is to establish such a correspondence combining experiment, numerical modeling and physical analysis.

To accomplish this objective we have chosen a model sample: a quantum ring (QR), in our case patterned from a InGaAs/InAlAs heterostucture. In this family of devices several experiments have evidenced interferences formed by the electron waves propagating through their arms [7][8][9]. In these experiments, these wave-like properties are probed by macroscopic quantities (typically the overall current) and the interference pattern is revealed by the subtle changes induced by, *e.g.*, applying an external magnetic field or a gate voltage to modulate the electron concentration. In general, even when they are of a spectroscopic nature, transport experiments give information on the electron energy levels rather than direct information about the wave functions or electron probability density in real space [10].

In the same chapter we complete this analysis using SGM. In our experimental images we observed two different perturbation regimes. The first regime corresponds to a region where the tip is 'far' from the QR. In this case, the fine perturbing potential induces a phase shift of the electron wavefunction. This effect is responsible for the appearance of concentric fringes in our experimental images.

The second experimental situation is obtained when the tip is over the QR. In these circumstances, radial fringes are observed. We show from the comparison between experimental results and quantum mechanical simulations that these fringes reveal the electron probability density inside the QR. This result is most relevant because it can provide new insight into the behaviour of electrons in mesoscopic devices and it opens the perspective to design new devices.

Chapter 2

The Low Temperature Atomic Force Microscope

Contents

2.1 Introduction

Gaining local information has been an old ambition in physics, in particular, in solid-state physics. Indeed, a large part of the scientific community has been asking for a long time how the behaviour of 'small' part contributes to the general behaviour of a whole ensemble.

Many theories use bottom-up approaches, *i.e.* they start with the behaviour of a single element and end up with the behaviour of a whole

system. The experimental verification is always a challenge. Add to this the fact that in the real world, impurities, defects and imperfections can be, at the best, reduced to small quantities. But even at these small quantities their effects can be dramatic [11] and the question remains how is each element going to contribute and be averaged in the behaviour of the whole device?

To address this issue an experimental field in solid-state physics emerged: near-field microscopy. Ideally, the approach is to study directly each single element, impurity, imperfection present on a surface. The goal is to study the morphology and the local properties on surfaces and devices on surfaces.

This family of experimental instruments is centered on a probe of 'very small' dimensions that is approached very close to the surface to probe, to perturb or to manipulate the surface. As the probe comes *in situ* to study some properties it should be adapted to the 'natural' ambient of the sample or to the 'natural' ambient of the physical properties under study.

During this thesis a near-field microscope was conceived to be adapted to study the electrical properties of buried semiconductor mesostructures. In our case we built a low-temperature atomic force microscope (AFM) to work in the electric regime (also known in literature as electric force microscope or scanning gate microscope) [12]. This family of instruments have been shown to be very well adapted to probe local electronic properties thanks to the localized electric field created by the sharp probe (*e.g.* [13][14][15][16][17]).

We have chosen to work at low temperatures and under magnetic field, because these kind of structures exhibit many interesting quantum phenomena in these conditions. Working at low temperature brings two additional advantages. Firstly, the thermal noise is decreased by a factor of $\sqrt{300/4} \simeq 8.7$, which implies a gain in force sensitivity [18] and, therefore, a gain in electrical charge detection sensitivity. Secondly, piezoelectric elements and mechanical pieces are very stable at low temperature which increases the overall stability of the instrument and a very small mechanical drift.

In this chapter we are going to describe the development of this tool and the first test we performed with it. The chapter is organized as follows:

- In the first section we describe the general operating principles of an AFM. This section is general for any AFM;
- In the second section we describe the construction of the microscope;

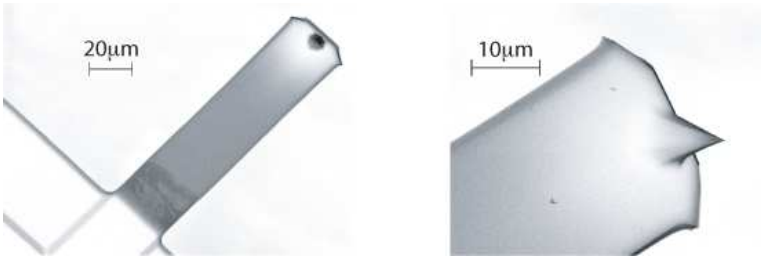

Figure 2.1: Scan electron microscopy image of a standard AFM tip

- In the third section, first tests are described. These tests are used to calibrate the instrument and to characterise its performance.

2.2 Principles of Atomic Force Microscopy

In 1981, Binnig and Rohrer [19] reported the invention of the first near field microscope: the scanning tunneling microscope (STM). For their invention they were awarded the Nobel prize in 1986. In the press release it was stated 'that entirely new fields are opening up for the study of the structure of matter' [20]. Two decades later, the most important scientific magazines confirm that this family of instruments is at the heart of many of the most advanced research in solid state physics. Part of the same family, the AFM invention came a few years later [21]. It has the particularity of being able to probe any metallic or non-metallic samples and to be a very little invasive technique. Here, we describe the principles of operation of an AFM in the dynamic mode and its fundamental limits.

2.2.1 Force Measurement

The heart of an AFM is a very sharpg tip located at the end of a micro-cantilever. A scanning electron microscopy (SEM) micrograph of an AFM tip is shown in Fig. 2.1. In the experimental setup the tip is used as a probe while the cantilever is a spring that measures the force between tip and surface.

In fact this idea is not original in itself as many instruments that we utilise in our daily life take advantage of a spring to measure, for example, the weight of a body (gravitational force). In this section, we describe an analytical approach to measure forces using a spring. Fig. 2.2 represents the conceptual idea of the system used to measure

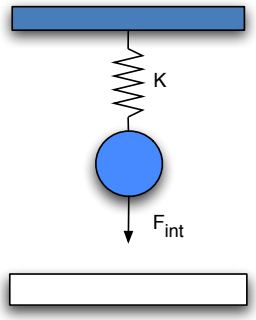

Figure 2.2: Scheme of the spring model. In this model the cantilever is considered as a spring vibrating in a viscous fluid.

a force. In first approximation, we consider a one-dimensional massless spring with an attached mass. The equation of motion is given by:

$$\frac{d^2}{dt^2}z(t) + \frac{\omega_0}{Q}\frac{d}{dt}z(t) + \omega_0^2 z(t) = \frac{F}{m^*} \tag{2.1}$$

where ω_0 is the resonance frequency, Q is the quality factor of the system associated with the internal damping and m^* is the mass of the object. The variable F describes the force acting on the object. Here this force is separated in two contributions:

$$F = F_{\text{int}} + F_{\text{stimulation}} \tag{2.2}$$

where F_{int} is the force of interaction between the object and sample and $F_{\text{stimulation}}$ is an additional force introduced by an excitation signal. In the dynamic mode we use an harmonic periodic signal to measure forces and: $F_{\text{stimulation}} = f\cos(\omega t)$. In this case the equation of the spring model becomes:

$$\frac{d^2}{dt^2}z(t) + \frac{\omega_0}{Q}\frac{d}{dt}z(t) + \omega_0^2 z(t) = \frac{f}{m^*}\cos(\omega t) + \frac{f_{\text{int}}}{m^*} \tag{2.3}$$

At free oscillation (*i.e.* $F_{\text{int}} = 0$) and for steady states the solution is a harmonic oscillation with the same frequency as the stimulation signal:

$$z(t) = A\cos(\omega t + \phi) \tag{2.4}$$

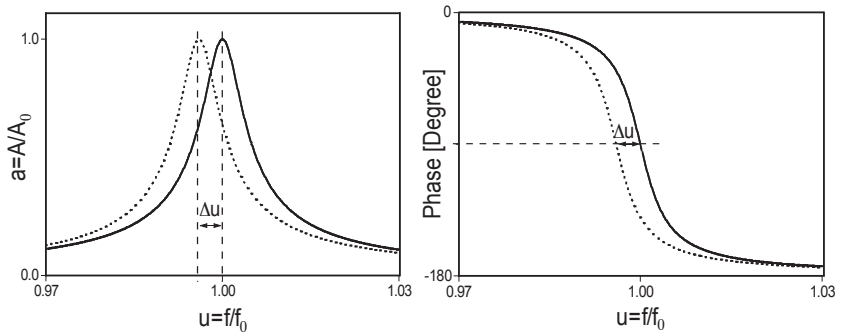

Figure 2.3: Resonance curves under the influence of a force load: a) and b) correspond respectively to the amplitude of oscillation (a) and phase (ϕ) versus the reduced frequency (u). We plot both curves for a perturbed (solid line) and unperturbed (dotted line) oscillator making use of expressions 2.5 and 2.6, respectively. In these images we used $Q = 150$ (typical quality factor for an AFM in ambient conditions)

where:

$$A(\omega) = \frac{A_0}{\sqrt{Q^2\left(1 - (\frac{\omega}{\omega_0})^2\right)^2 + (\frac{\omega}{\omega_0})^2}} \tag{2.5}$$

$$\phi(\omega) = \arctan\frac{\frac{\omega}{\omega_0}}{Q\left((\frac{\omega}{\omega_0})^2 - 1\right)} \tag{2.6}$$

where $A_0 = (fQ)/k$ is the free amplitude at the resonance frequecy. For $F_{\text{int}} \neq 0$, and assuming that the oscillator is perturbed by a small force, the system can be described, in a first approximation, by the first two terms of the Taylor expansion:

$$F_{\text{int}}(z) \simeq F_{\text{int}}(z_0) + F'_{\text{int}}(z_0)(z - z_0) \tag{2.7}$$

In this situation, equation 2.3 can be rewritten as:

$$\frac{d^2}{dt^2}z(t) + \frac{\omega_0}{Q}\frac{d}{dt}z(t) + (\omega_0^2 - \frac{F'_{\text{int}}}{m^*})z(t) = \frac{f}{m^*}cos(\omega t) + C^{te} \tag{2.8}$$

where $C^{te} = \frac{F_{\text{int}}(z_0) + F'_{\text{int}}(z_0)z_0}{m^*}$.

We conclude that, besides a constant term introducing a constant deflection, the new resonance frequency (ω_{eff}) is:

$$\omega_{\text{eff}}^2 = \omega_0^2 - \frac{F'_{\text{int}}(z_0)}{m^*} \tag{2.9}$$

and the shift of the resonance frequency is given by:

$$\Delta\omega = \omega_{\text{eff}} - \omega_0 = \sqrt{\omega_0^2 - \frac{F'_{\text{int}}(z_0)}{m^*}} - \omega_0 \simeq -\omega_0 \frac{F'_{\text{int}}(z_0)}{2k} \tag{2.10}$$

This shift in the resonance frequency of the oscillator is going to be used to detect forces. Analyzing this expression we find directly that for repulsive forces ($F'_{\text{int}}(z_0) < 0$) the shift in frequency is positive ($\frac{\Delta\omega}{\omega_0} > 1$) while for attractive forces ($F'_{\text{int}}(z_0) > 0$) the shift in frequency is negative ($\frac{\Delta\omega}{\omega_0} < 1$). Moreover, we conclude that the dynamic mode is sensitive to the derivative of the force rather than to the force itself. This behaviour can be very useful if one wants to avoid constant forces. Fig. 2.3 represents the amplitude ($a(u)$) and the phase ($\phi(u)$) versus the reduced frequency ($u = \frac{\omega}{\omega_0}$). We plot both curves for $F_{\text{int}} = 0$ and $F_{\text{int}} \neq 0$ making use of expressions 2.5 and 2.6. We used $Q = 150$ (typical quality factor for an AFM cantilever in air) and $\frac{\Delta\omega}{\omega_0} = 0.004$.

In the next section we will describe the topography principles using the spring model. Afterwards, we discuss the resolution and the limitations that can be expected from this method.

2.2.2 Approach-Retract Curves and Topography Images

The question now is to know how we are going to build topographic images making use of the shift in frequency when the tip probes surface forces.

To better understand the whole process we start with the concept of approach-retract curves. In these curves, the purpose is to investigate the distance dependence of the data. We define approach-retract curves as the recorded data (here amplitude and phase for the dynamic mode of operation) while the tip slowly approaches to and retracts from the surface. In this case we assume that the system is at each point in a steady state.

From the previous linear model, we expect that both phase and amplitude should decrease for a cantilever excited at the resonance frequency and if the tip only probes a positive force gradient. In contrast, if the gradient is negative, we should see a decrease of the amplitude and an increase of the phase. Seen from this perspective it becomes

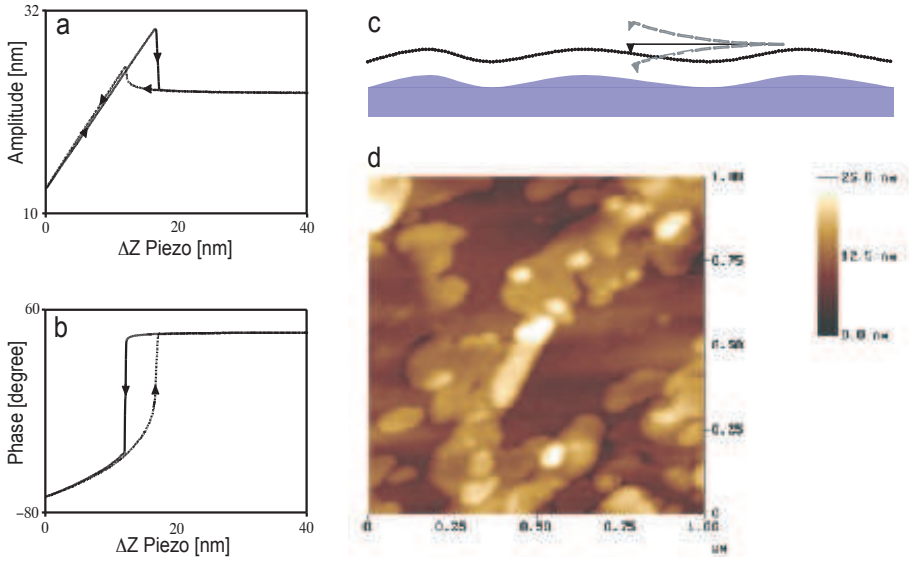

Figure 2.4: In a) and b) we show experimental approach-retract curves taken at ambient conditions where a) is the amplitude and b) the phase. c) is representating the principle of topographic images. As the tip scans over the sample, a SiO_2 surface, a feedback in amplitude is maintained to ensure a constant distance between the tip and the surface. d) is a topographical image taken at ambient conditions

clear that the phase is a sensor capable of distinguishing between contact and non-contact interactions[22].

In Fig. 2.4 we show, as an example, experimental approach-retract curves over a SiO_2 sample. In this case we observe a phase decrease which means that the tip is always probing positive gradient forces.

To build topographic images the basic principle is to have a sensor that guaranties that the tip-surface distance is constant. In the dynamic mode the cantilever is excited by a periodic signal giving the tip an oscillating behaviour at the same frequency. During the scan the amplitude of oscillation (smaller than the free oscillation amplitude) is maintained constant by a feedback loop that serves the scan piezo to approach or to retract from the mean position of the oscillating level. In the meanwhile, the system records, at each x-y position of the sample, the z (vertical) displacement of the piezo needed to maintain a constant amplitude. A two-dimensional image of the sample surface is therefore built up. These constant amplitude images are, in the perspective of the spring model, constant force-gradient images. In fact, if all electrical and mechanical properties are constant all over the sam-

ple (*i.e.* if it is homogeneous and isotropic), then the constant gradient is equivalent to constant distance, and consequently these images are topographic images. An experimental approach-retract curve and a topographic image are shown in Fig. 2.4.

2.2.3 Fundamental Limits

In this section we determine the physical limits of this tool. In our experiments two factors are found to dominate the force sensitivity and the image resolution: the thermal noise and the tip shape. Here we evaluate the magnitude of these parameters.

Thermal Noise in a mechanical oscillator and Minimum Detectable Force

In a mechanical oscillator there is always a natural oscillation provoked by the finite temperature. It is caused by the brownian motion of the molecules of gas surrounding the cantilever and the phonons of the cantilever. The fluctuation dissipation theorem quantifies the amplitude and spectral distribution of this movement. Taking the equation of movement of the lever (Eq. 2.1) and considering $\widehat{z}$ and $\widehat{F}$ the Fourier transform of z and F, respectively, the general solution in the Fourier space is given by:

$$\widehat{z} = \frac{\widehat{F}}{m^*}\left(\frac{\omega_0^2-\omega^2}{\left(\omega_0^2-\omega^2\right)^2-\left(\frac{\omega_0\omega}{Q}\right)^2}+i\frac{\frac{\omega_0\omega}{Q}}{\left(\omega_0^2-\omega^2\right)^2-\left(\frac{\omega_0\omega}{Q}\right)^2}\right) \tag{2.11}$$

Now defining G the transfer function of the oscillator:

$$G = \frac{\widehat{F}}{\widehat{z}} \tag{2.12}$$

the fluctuation dissipation theorem relates the spectrum density of the tip motion, $\langle|\widehat{z}(\omega)|^2\rangle$, to the imaginary part of G, Im$[G]$, by:

$$\langle|\widehat{z}(\omega)|^2\rangle = \frac{k_BT}{\pi\omega}\mathrm{Im}[G] = \frac{k_BT}{\pi k\omega_0 Q}\frac{\omega_0^4}{\left(\omega_0^2-\omega^2\right)^2-\left(\frac{\omega_0\omega}{Q}\right)^2} \tag{2.13}$$

where k_B is the Boltzman constant and T the temperature. Thus the thermal noise excites the lever with a vibration noise N of:

$$N = \sqrt{4\pi B\langle|\widehat{z}(\omega)|^2\rangle} \tag{2.14}$$

where B is the bandwidth of the detection system. The smallest detectable force derivative, $\delta F/\delta z|_{mim}$, is the force gradient that produces

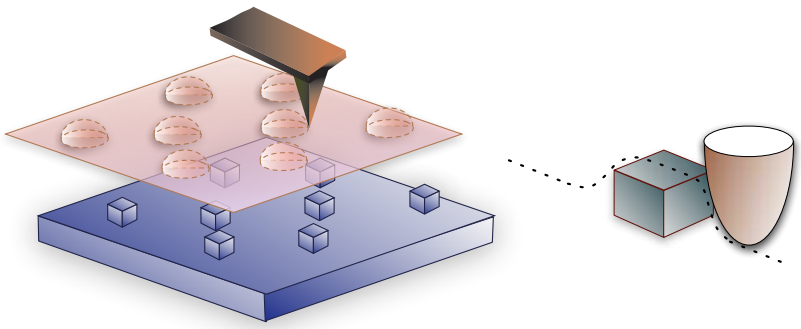

Figure 2.5: Schematic representation of the topographic convolution between the tip and the surface. This phenomenon limits the topographic resolution. In standard conditions, with a tip apex of 10 nm, the lateral resolution is about 20 nm. The vertical resolution is nevertheless maintained and it is, normally, better than 1 nm

a displacement equal to the thermal noise fluctuations. In this case we have $A_0 \Delta a = N$. So, at the resonance frequency, one obtains [23]:

$$\left.\frac{\delta F}{\delta z}\right|_{min} = \frac{1}{A_0}\sqrt{\frac{27 k k_B T B}{Q \omega_0}} \tag{2.15}$$

For a typical AFM using typical values, *i.e.* k=1 N/m, B=300 Hz, resonance frequency of 100 kHz, Q=300 and T=300 K the minimum detectable force gradient is 2×10^{-5} N/m. Another remarkable conclusion is that decreasing the temperature to 4 K allows gaining a factor of $\sqrt{300/4} \simeq 8.7$ in terms of force resolution. So, at ^{4}He liquid temperature, the gradient resolution is 2.3×10^{-6} N/m.

Nevertheless, the thermal noise can be used as an elegant and precise way of determining the spring constant of the cantilever. An experimental thermal noise can be fitted by the Eq. 2.13. The spring constant is the only free parameter.

Image Resolution

Here we make a remark concerning the resolution of an AFM image. In the previous section we mentioned the force resolution. Nevertheless this is not the only parameter. Another crucial parameter is the size and shape of the tip.

In Fig. 2.5 we illustrate this principle. As the tip scans the surface there is a convolution between the tip and the morphology of the

surface. The final result is always a smoothed image reflecting both surface and tip shapes.

To obtain higher image resolution one must use either sharper tips or shorter range forces [24]. Using commercial AFM silicon tips, most of the experiments where atomic resolution is obtained are performed at ultra high vacuum where surfaces are very clean [25]. In general, at ambient conditions the resolution is limited by the tip apex. In this case one obtains a lateral resolution of 10 to 20 nm and a vertical resolution is sub-nanometric.

2.3 Conception of the Low Temperature Atomic Force Microscope

The low temperature AFM was to a large extent designed and manufactured during the period of this thesis. The system was based on a commercial attocube@ system (attoAFM I [3] [4]) to which an improved AFM head was included. Every piece was chosen carefully so that the AFM could operate at low temperature and under a magnetic field. In the next section the chosen options are going to be presented.

2.3.1 Requirements and Overview

This instrument demands three specific properties that are not usually found in commercial AFMs:

- Low temperature operation;
- Ability of operating in the presence of a magnetic field;
- Versatility to host samples with several electrical contacts.

In response to these requirements, the AFM was designed to be mounted in a cage-like structure formed by three bars. This structure is inserted in a tube that is itself going to be inserted in a ^{4}He cryostat. The cryostat is equipped with a superconducting magnet that can deliver a magnetic field up to 9 T at 4.2 K. In Fig. 2.6 we show the project and a sketch of the concept of the microscope while in Fig. 2.7 we show photographs of the experimental setup.

The available space inside the cryostat is limited. In order to be compact, the microscope is built around an optical fibre based interferometer. The cleaved single-mode fibre together with the tip lever form a Fabry-Perot interferometer. This optical detection method was

shown to be able to detect vertical displacement of a cantilever with high sensitivity [26] [27].

The microscope is made of non magnetic materials (mainly Al, Ti and ceramic). These materials were carefully assembled in order to compensate for thermal contractions. These two conditions permitted the AFM head to work from 300 K to 4.2 K and under a magnetic field.

During the construction of the microscope, the flexibility was another key point. The AFM is adapted to host samples that can be simple metallic surfaces or complex devices that might have several electronic contacts. In this respect special care was given to the cabling so that electrical contacts would be reliable without affecting the mechanical stability.

Finally, the displacement of the sample under the tip is done via x-y-z attocube@ inertial motors for the coarse approach [28] and a five electrode scanner tube for a precise and smooth scanning when images are being acquired. The inertial motors have a step-like behaviour permitting simultaneously a precise nano-positioning (resolution of 10 nm at 4 K) and a long range travel in the centimeter range (7 mm) at low temperatures and under magnetic field. A maximum bipolar voltage of 120 V gives to the piezo tube a scan range of 30 μm in x-y directions and a z-range of 3 μm at 300 K. At 4.2 K the scanner loses roughly an order of magnitude making the lateral range limited to 3 μm and the z-range to 800 nm.

The system is equipped with a commercial scanning probe high voltage controller (Dulcinea Control System from Nanotec@ electronica [29]). This electronics is composed of three modules: 1) lock-in amplifier used to demodulate the amplitude of vibration of the cantilever; 2) a proportional-integral feedback system to build topographic images ; 3) and high voltage units to feed the piezo scanner. This electronic system permits the control of the piezoelectric scanner tube when images are being obtained and the simultaneous acquisition of several signals generated inside or outside the electronics.

2.3.2 Microscope Head and Optical Detection

In Fig. 2.8 we show a picture of the AFM head. The system was designed in such a way that the tip can be adjusted in front of the edge of the cleaved fibre to form a Fabry-Perot type cavity [3]. The light is injected into this cavity through the fibre itself and the reflectance of the cavity is collected by the same fibre. The tip is mounted on a stack of two piezos: adjusting piezo and driving piezo.

The fibre is fixed in a holder by means of two teflon pieces and a

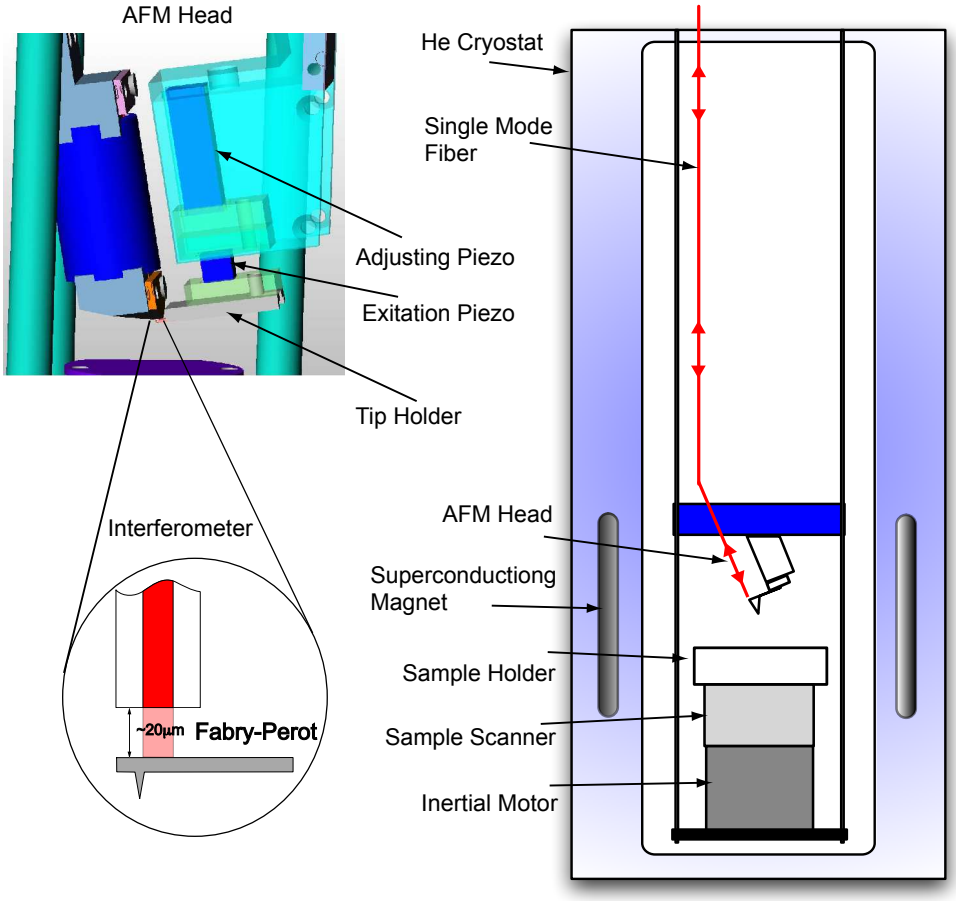

Figure 2.6: Schematic representation of the low temperature AFM. The AFM is inserted inside a commercial ^{4}He cryostat and the optical detection of the lever deflection is done via an optical single-mode fibre that forms an optical cavity with the cantilever (see text). A detail of the project AFM head is also shown.

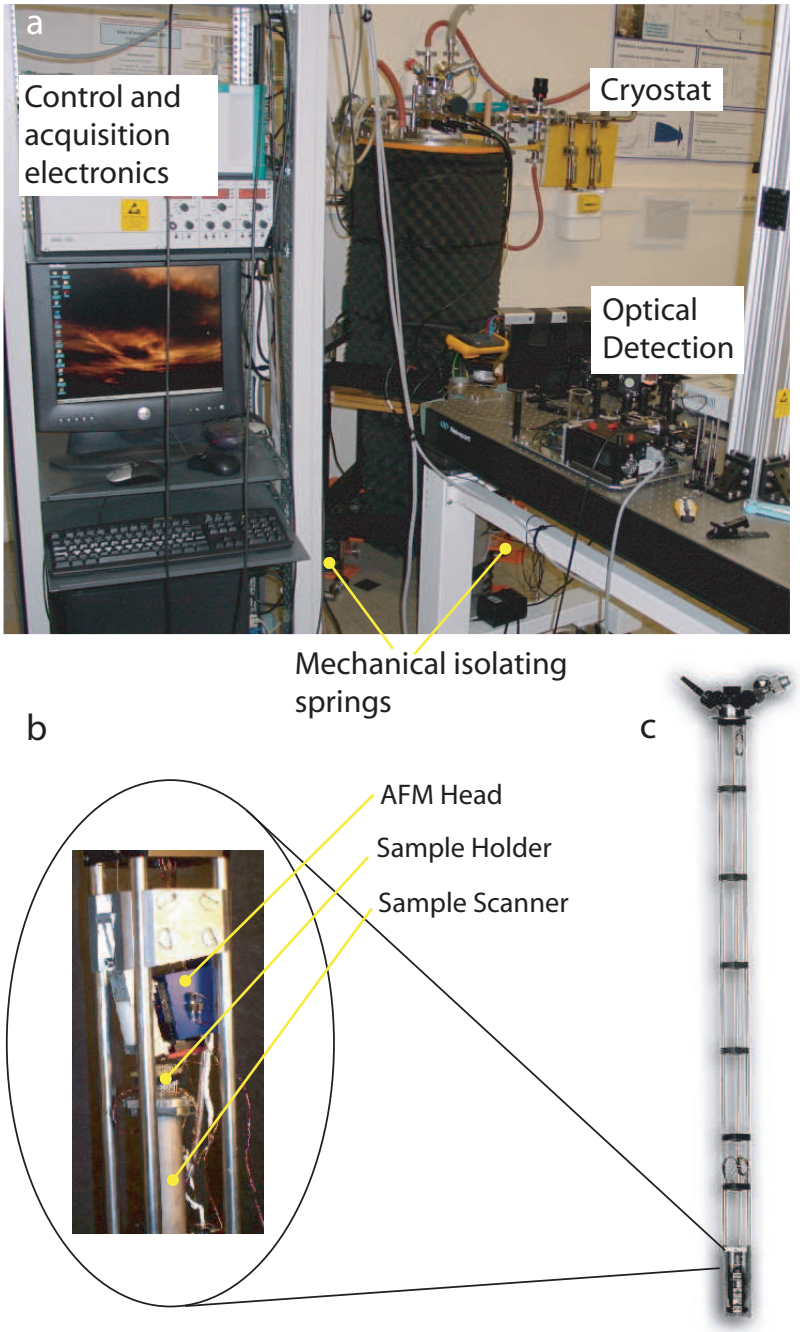

Figure 2.7: Experimental setup. In a) we show an overview of the experiment. In b) and c) we show photographs of the microscope designed to be inserted inside a cryostat.

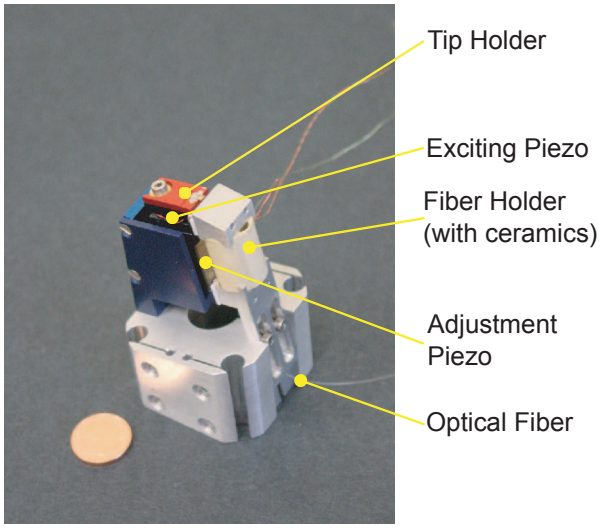

Figure 2.8: Picture of the home made AFM head

small drop of glue next to the fibre edge. To anticipate for differential thermal contractions the fibre holder is equipped with a ceramic with, approximately, the same dimension and the same thermal coefficient as the piezo stack.

The adjustment of the cavity is done manually. First the tip is adjusted in front of the fibre. Afterwards the fibre is approached towards the tip. At the end of the process, the tip-fibre distance should be around some tens of microns.

In Fig. 2.9 we show the theoretical curves of the light reflected by a Fabry-Perot cavity as a function of the tip fibre distance. These curves respect the classic Airy function:

$$\frac{I_R}{I_0} = 1 - \frac{1}{1 + F\sin^2 \frac{\pi D_{Fibre}}{\lambda_{laser}}} \tag{2.16}$$

where I_0 and I_R are the light intensity injected and reflected from the cavity, F is the coefficient of Finesse (which is directly linked with the reflectivity of the mirrors), λ_{laser} is the wavelength of the laser and D_{Fibre} the distance between fibre and cantilever. There are two relevant points in these curves. Firstly, the amplitude of the fringes reduce very strongly with decreasing F. Experimentally we observed that in our experimental setup the coefficient of Finesse is around 0.03. Secondly, two consecutive minima correspond to a displacement of $\lambda_{laser}/2$. This gives us a very accurate length reference for future calibration. Experimental curves will be shown in Fig. 2.10.

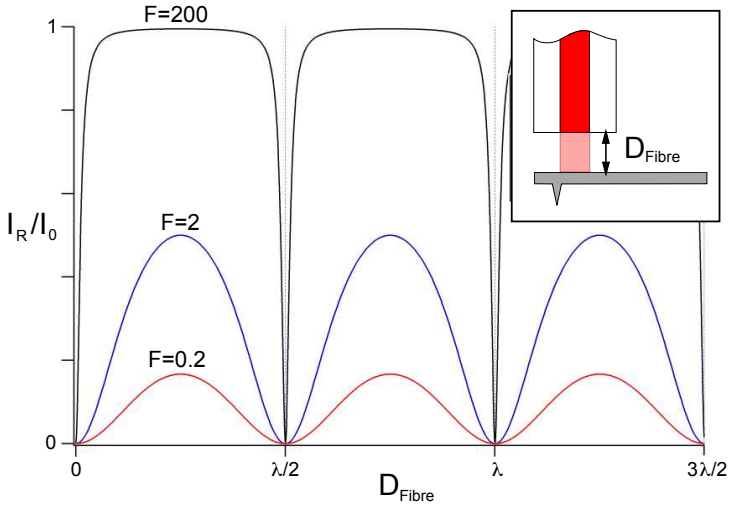

Figure 2.9: Theoretical curves of the light reflected by a Fabry-Perot cavity as a function of the mirrors distance. This curves were calculated for different coefficient of Finesse F. Experimentally it was found that the tip together with fibre form a Fabry-Perrot cavity with a $F \simeq 0.05$.

The fine adjustment is done making use of the adjusting piezo. The tip is positioned at a point where the slope of Fabry-Perot curve is maximal. At this point, if the tip performs a small displacement (*i.e.* much smaller than $\lambda_{laser}/2$), the fluctuations of light are proportional to the amplitude of vibration of the lever. The proportionality factor is the slope of the curve.

This effect permits the calibration of the cantilever deflection. If one wants to do a quantitative measurement with the AFM this is a very important point.

The optical setup is composed by two optical fibres that are sold together, a laser diode and a photodiode detector. The coupled fibres work as a fully fibreed beam splitter and permits the injection of light inside the microscope and the separation of the reflected light. The wavelength of the laser diode laser is 671.4 nm and the single-mode fibre is adapted to this wavelength. The laser is equipped with a temperature stabilized current source and a Faraday isolator to avoid re-injecting light in the laser. Coherence length is announced by the constructor to be around 50 μm.

2.3.3 Cryostat and Mechanical Isolation

The experimental setup includes a commercial liquid ^{4}He cryostat. To avoid a large consumption of He, the cryostat is composed of two concentric reservoirs. The external reservoir is filled with liquid nitrogen and the central reservoir with liquid ^{4}He. The separation between the two reservoirs and the separation between reservoirs and the external environment are maintained in vacuum conditions. The tube, where the microscope is inserted, is poured directly into ^{4}He.

The mechanical isolation from the environment is realized via four big soft springs mounted under the cryostat. Furthermore, the exhaustion cryogenic tubes were chosen to be soft. Using this method, it was found that the remaining mechanical noise came from the evaporation cryogenic liquids.

To avoid a strong mechanical coupling between the cryogenic liquid and the AFM head, the bars from the cage like structure were cut in pieces of different lengths.

2.4 Testing

In the following section we describe the process of setting the microscope at low temperature and tests to ensure the good functioning of the microscope. Afterwards we show typical results obtained with this system and the calibration method we used.

2.4.1 Cooling of the Microscope

Before cooling, the system is pumped down to secondary vacuum to evacuate any trace of water vapor. After this operation, 10 mbar of He are introduced. This small pressure of He is used to thermalize the microscope at low temperature. Then, the entire system is put to low temperature. This procedure is done slowly to ensure no damage due to thermal chocks. Typically, cooling the microscope takes three hours. In the meanwhile, the good functioning of the AFM head is controlled by the Fabry-Perot interference fringes. Experimentally we observe that, because of thermal contractions, the fibre retracts from the tip some 50 micrometers. In Fig. 2.10 we show an interference fringe taken at low temperature and a resonance curve of the cantilever. Using Eq. 2.16 we extract the coefficient of Finesse $F = 0.03 \pm 0.02$. Furthermore, as mentioned earlier, the amplitude of oscillation of the resonance curve, on the right, is determined using the fact that two consecutive fringes are separated by half of a wavelength of the laser. In this case the conversion factor is 1.9 ± 0.2 V/nm.

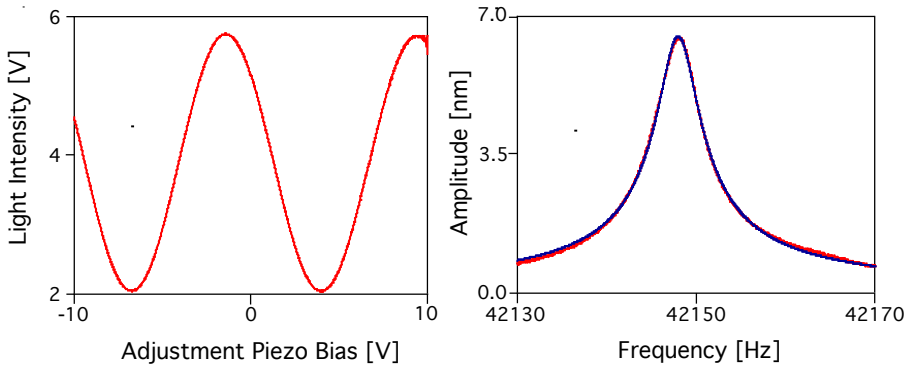

Figure 2.10: On the left we show an experimental Fabry-Perot interference pattern taken at 4.2 K. The fringes are used to calibrate the amplitude of vibration of the cantilever. On the right, we show experimental resonance curve of the AFM cantilever at 4.2 K. This curve is fitted by a lorenzian curve which allows the determination of the resonance frequency (f_R= 42.148 kHz) and quality factor (Q = 9077)

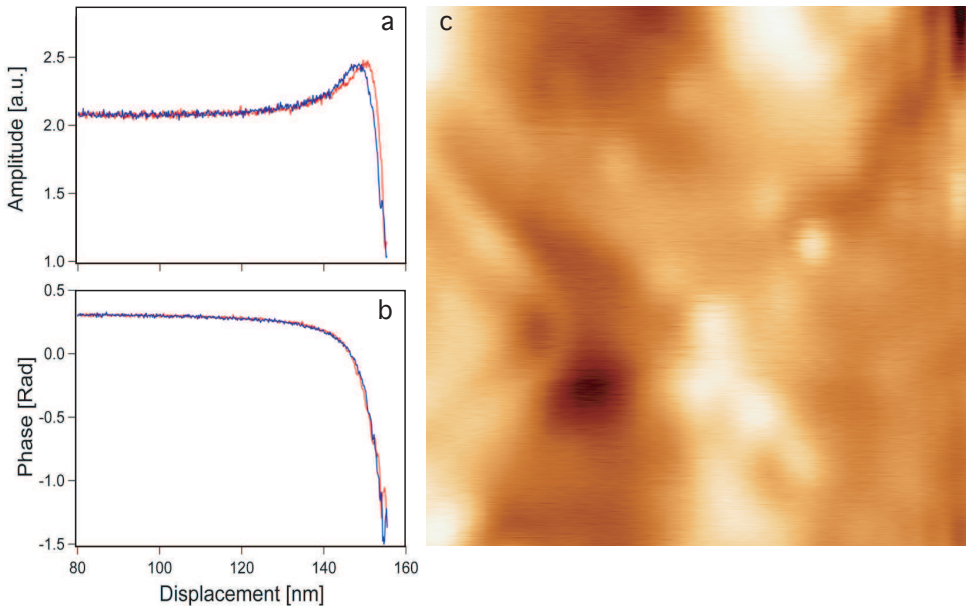

Figure 2.11: (a) and (b) are approach retract curves, amplitude and phase, respectively, done over a gold sample at ^{4}He. In (c) we show a topography obtained in the same conditions

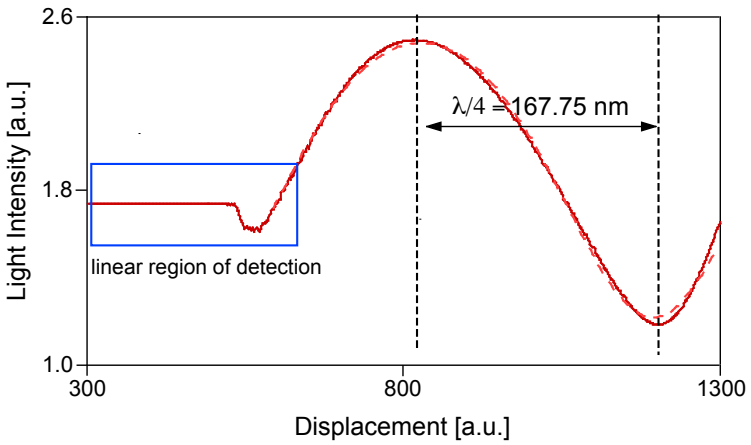

Figure 2.12: Approach curve used to calibrate the vertical displacement of the scanning piezo.

The second step is to approach the sample towards the tip. For that we use the inertial motors. In between each step we make one approach attempt to ensure that we do not touch the sample. Once we get close to the sample we obtain one approach-retract curve as shown in Fig. 2.11 (a-b). Experimentally, this procedure is long due to the non-reproducibility of the inertial motors. Furthermore, occasionally, it was found that the inertial motor blocks. We unblock it by sweeping the amplitude and the frequency of the electrical signal sent to the motors. Typically, once the system is at low-temperature, it takes, in average, one to two days to perform the approach. The very first topographic image obtained with this microscope at 4.2 K is shown in Fig. 2.11(c). The sample is a flat gold surface.

2.4.2 Calibration

In this section we describe the calibration of the system. This step is crucial in the experiments that follow. We begin with the calibration of the vertical displacement. Then, we describe the method used to calibrate the x-y axes. At the end we show the procedure to calculate the spring constant of a cantilever. This last step has to be done each time a new tip is used.

Calibration of the scanner

The calibration of the vertical displacements is illustrated in Fig. 2.12. In this image we record the static deflection of the lever as the tip

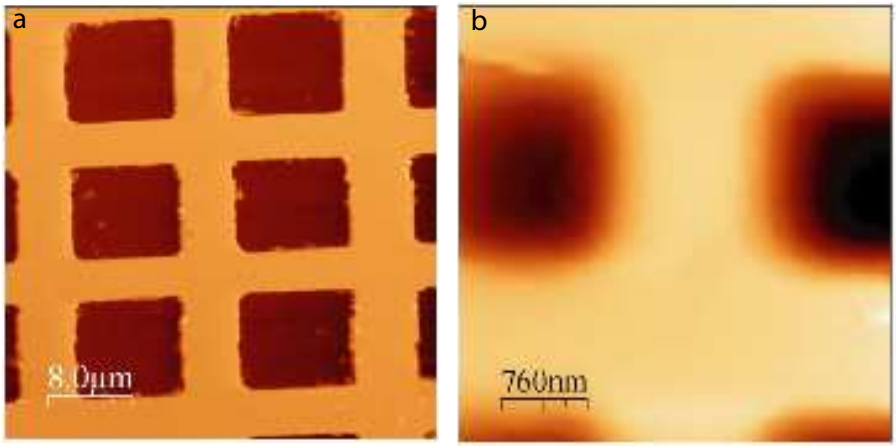

Figure 2.13: Topographic image of the grating used to calibrate the x and y axes at ambient conditions (a) and at low temperature (b). The size this square like holes is give by the manufacture

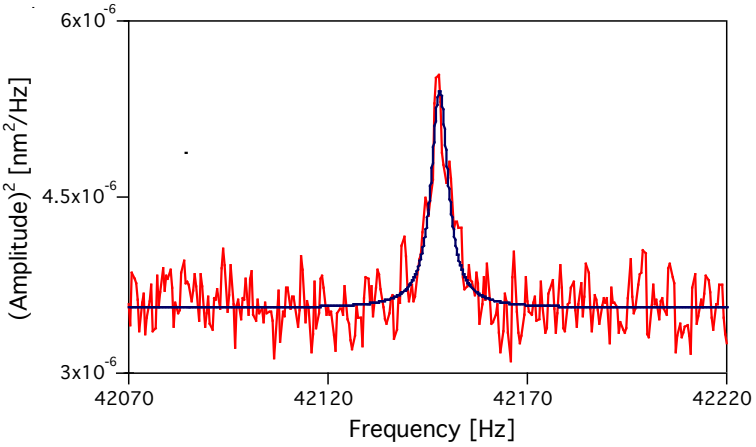

Figure 2.14: Thermal noise of a cantilever at 4.2 K. From the fit it is possible to determine the spring constant $k = 4.37$ N/m

approaches a surface of silicon. For this purpose, the sample can be considered as a hard material and so, once the tip touches the surface, no more indentation is possible and it remains at a fixed point. After touching the surface, the deflection of the cantilever coincide, therefore, with the vertical displacement of the scanner. The interference fringes observed in Fig. 2.12 are a direct measurement of the dilatation of the piezo tube. Assuming that the piezo scanner has a linear response with voltage, we are allowed to calibrate the vertical axes. We obtained a calibration factor of 6.67±0.35 nm/V at 4.2 K.

The calibration of the x and y axes was done via a calibrated sample. In this sample we have several regions with a pattern of square like holes with different dimensions. This dimensions are given by the manufacturer. In Fig. 2.13 we show topographic images for both ambient conditions and liquid ^{4}He temperature. From these images we obtain an horizontal plane piezoelectric factor of 278 nm/V at 300 K and 28.7 nm/V at 4.2 K. In these values, we allow for an error bar of 15%. This error bar is due to the sample uncertainty and to the non linearity of the piezo scanner.

Calculation of the spring constant of the cantilever

The thermal noise spectrum of a cantilever at 4.2 K is shown in Fig. 2.14. This spectrum is most important because it reflects the resolution of this instrument and it permits to calculate the rigidity of the cantilever.

Observing this figure, the first conclusion is that the background noise in our experimental setup (including shot-noise of the laser, and mechanical noise of the environment) is 1.8 pm/$\sqrt{\text{Hz}}$. At the resonance frequency, even at low temperature, the noise level is increased by the thermal noise. The noise level value is 2.3 pm/$\sqrt{\text{Hz}}$.

As described in section 1.2.3, we can determine the spring constant by fitting the experimental data with Eq. 2.13. From the experimental thermal noise we calculate the spring constant as k= 4.37 N/m.

2.5 Summary and perspectives

In this chapter, we have described the working principles and the design of a low temperature scanning probe microscope. We have seen the first tests and the ability of the AFM to operate at low temperature. Furthermore, we have calibrated both the in-plane and vertical axes of the microscope scanner. This microscope has three advantages in comparison with commercial AFMs. Firstly, it can operate inside a

cryostat and in a presence of a magnetic field. Secondly, it permits the determination of the amplitude of vibration of the cantilever. At last, this AFM is versatile to host devices with several electronic contacts.

Nevertheless, we would like to number some possible improvements that could be included while re-designing a new AFM. The improvements concern two aspects, the comfort while manipulating the AFM and the noise level:

- Replacing the ceramics in the fibre holder (described in section 1.3.2) by an inertial motor. This alteration will bring comfort and accuracy while adjusting the Fabry-Perot cavity. Furthermore, it was also found that the fibre retracts some tens of μm while decreasing the temperature leading to a lost of sensitivity or, sometimes, to the complete loss of the optical signal from the cavity. This improvement would completely compensate for this effect. One should notice that there are, nevertheless, two inconveniences when adopting this solution. Firstly, it will increase the fragility of the AFM head. Secondly, six additional electrical contacts are needed inside the cryostat.

- Protecting the driving piezo from undesired torque application. As described previously, the AFM tip is glued in a tip holder that it mounted on top of a pile of piezoelectric elements. We found that successive positioning of the tip eventually breaks the driving piezo. We suggest, *e.g.*, a U-like structure inside which the driving piezo would be glued. On the other hand, concerns with the adjusting piezo do not seem to be justified as it had shown to be must more resistant.

- Finally we would like to propose a damping system to the AFM head. It was found that the springs mounted under the cryostat were very efficient to isolate the AFM from any external sources of mechanical noise. Nevertheless, a source of noise originating from evaporation of cryogenic liquids remains. Solving this problem does not seem to be an easy task, since mechanical springs become rigid at low temperature. It is, however, and important issue if the system is used to measure weak forces.

Chapter 3

Electric Force Microscopy in Parametric Amplification Regime

Contents

3.1 Introduction

In the beginning of this thesis we aimed at investigating and establishing a method to probe charges over a surface. For that purpose, we have developed a theory, confirmed by experiments, that is capable of increasing the sensitivity to detect electrostatic forces. The proposed method uses a parametric amplification regime. Parametric amplification has already been observed in several mechanical systems such

as micro-actuators [30][31]. In an AFM configuration it was used once to experimentally demonstrate thermo-mechanical noise squeezing [32]. Here, we further investigate this technique to detect small charge or potential differences between tip and surface. This model was developed, to a large extent, by a member of our group, Thierry Ouisse, and the results were published in [33] and [34].

Indeed, probing very small charges or electrostatic potential variations has become a key aspect in various fields of solid-state physics [35][23]. In particular, the AFM has proven a powerful tool thanks to its ability to measure small variations of local properties [36][37][38][39][40] [41]. As a specialized technique, Electric Force Microscopy (EFM), a derivate of dynamic force microscopy, is actively investigated for its capacity to explore charge distributions in nanostructures[42]. Typically, EFM is performed as a dynamic method [36]. A sinusoidal electric signal is applied to the investigated substrate at a frequency ω_{el}. The electric force between the sample and the metallized tip results in a modulation of the amplitude oscillations either at ω_{el} or $2\omega_{el}$, depending on whether the constant offset voltage or the alternating part prevails, respectively.

Our experiments demonstrating the existence of such effects were performed at ambient conditions. Nevertheless, we used the low temperature AFM, described in the previous chapter, for three reasons. Firstly, our system is more versatile and 'open ' than typical commercial AFMs permitting full monitoring of the signals applied to the system. Secondly, the optical detection allows amplitude calibration of the tip vibration. Finally, these experiments served to test the stability of the instrument.

An experimental example of the ability of the AFM to isolate electrostatic interaction from topography is shown in Fig. 3.1. In these experiments electrostatic images are taken in two steps (each consisting of one trace and retrace) across each line. First topographic data is taken, as explained in Chapter 1. Then, an alternative electrostatic signal (V_p) is applied and the amplitude and the phase shifts are recorded rising the tip up by a 'lift height'. The second trace and retrace are done with a constant separation between the tip and the local surface topography, with the feedback turned off. This method has been shown to be capable of distinguishing between forces of different ranges (*e.g.* [5]). In fact, when topography is being recorded the dominant interactions are, in general, short-range repulsive interaction and van der Waals forces. In contrast, for a tip at a distance around some tens of nanometers from the surface and applying an alternative electric signal these forces can be neglected. In this case, capacitive forces become

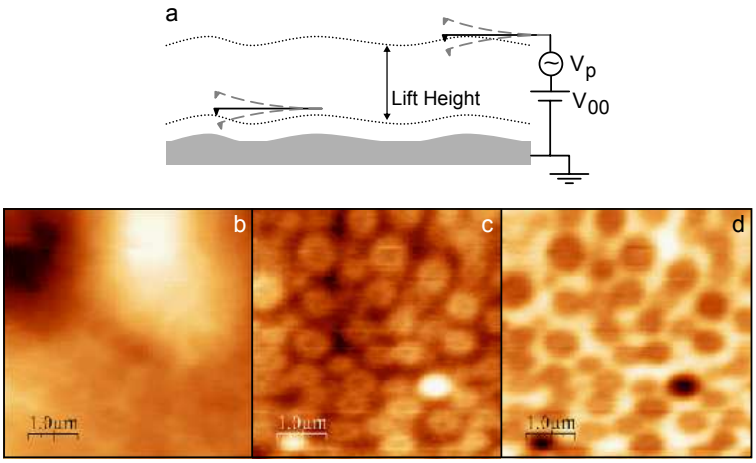

Figure 3.1: Experimental topographic and electrical images taken at ambient conditions with our AFM. a) Scheme of the applied imaging mode where the sample is scanned in a double passage to obtain independently the topography and the electrical measurements at a certain lift height and under an applied voltage (V_p and V_00). b) Topography of a thin film of ITO on the top of which a layer of a mixture of polymer and molten salt was deposited. (c) and(d) are electrical images (amplitude and phase) of the same region at a lift height of 50nm with feedback off.

the most important contribution and so electrostatic images give direct description of the local capacitive interaction, *i.e.* the local charge distribution. Fig. 3.1(b-d) shows experimental topography and electric images (amplitude and phase), respectively, of a thin film of indium tin oxide (ITO) covered by a layer of a mixture of conductive polymer and molten salt. In this sample, the molten salt forms small domains that are surrounded by the polymer. Inside the domains of molten salt the anions and cations are free to orientate while the conjugated polymer behaves as an insulator at small fields. Therefore, if a polarized tip scans the surface we can clearly distinguish between the two materials. These three images are very useful for demonstrating the ability of separating the van der Waals contribution, Fig. 3.1(b), from the capacitive contribution, Fig. 3.1(c-d), and to differentiate the regions of polymer from the domains of ionic salt. Indeed, the images of amplitude and phase are, in first order, strongly correlated. Nevertheless, for a complete understanding of the tip-surface interaction both information are needed [43]. These images were obtained at ambient conditions with our AFM.

In this chapter we explore the frequencies of the electric signal ap-

plied to the tip in the context of a parametrical amplification model. This approach covers as well the case of Kelvin probe force microscopy (KFM), a widely used technique to measure local electrostatic properties of a sample.

To be able to use a parametric regime in EFM first requires a complete understanding of its various effects. Here, our aim is to provide such an understanding. We present a fully analytical approach that is crosschecked with numerical results. We also give some experimental evidence of the model validity. Then, we propose to put it to good use for improving the sensitivity of charge detection or surface potential measurement. We note that in such a system any cantilever excitation and thermo-mechanical noise are amplified in the same way, so that the case of thermal noise has to be discussed separately. But parametric amplification provides the ability to drastically reduce the impact of all other noise sources. And even in the case of thermal noise, we suggest a strategy to beat the conventional limit. These method makes use of the fact that the information that we want to extract does not lie in the raw piezo-electric excitation of the cantilever, which can be made much larger than the thermal noise, but in the amplification gain, which is tunable to a large extent.

The chapter is structured as follows:

- In section 2.2 we describe a numerical method to calculate the instability domains of the cantilever oscillations, whatever is the form of the electric signal applied to the substrate, and to any degree of accuracy. The description of these instability domains leads to the extraction of conditions that are well adapted for charge or voltage detection.

- In section 2.3 we derive a fully analytical solution of the differential equation in the parametric regime with an electrical excitation ω_{el} around twice the natural frequency $2\omega_0$ of the oscillator. We follow the treatment described by Rugar and Grütter some years ago [32]. Nevertheless we obtain contrasting conclusions. The optimal setting of phase and voltage offset for voltage or charge detection are deduced as a function of the main physical parameters of the system. This results are confirmed by experiments. This analysis have permitted us to discuss the impact of thermal noise on the electric measurements. We show that if thermomechanical noise is not the prevailing noise source, the predicted sensitivity for charge detection can be increased by several orders of magnitude in comparison with the usual low frequency detection scheme.

- In section 2.4 we treat the case of ω_{el} around ω_0, which also induces parametric amplification. This electric regime is commonly known in literature as Kelvin force microscopy.

3.2 Determination of the instability Domains of the Cantilever Oscillation

3.2.1 Simple approach

Before describing how we can get advantage of the parametric excitation to amplify the motion of an oscillator we start by determining the conditions that make the dynamics of the cantilever entering into an unstable regime. Here, our goal is to give simple arguments to demonstrate the existence of such instabilities. To do so, we consider a classical example that is treated in several textbooks, *e.g.* [44]: the parametric pendulum.

A medieval example of such a system is the 'Botafumerio' in the Cathedral of Santiago de Compostela, Spain. It consists on a mass of 56 Kg that is hung in a rope of 21 m long. This pendulum is swung at a maximum angular amplitude of 80^o and it is literally used to 'spread smoke' inside the cathedral during special occasions. Impressively, this rite is thought to be part of the liturgies for 700 years, *i.e.* several centuries before the pendulum was studied. A detailed analysis of the movement the 'Botafumeiro' can be found in [5].

Our analysis is much simpler. Our purpose is to demonstrate the existence of unstable regimes. Indeed, when an oscillating system is subjected to parametric amplification it may be driven into an unstable state where non-linear contributions considerably influence the actual motion.

In Fig. 3.2 we sketch the principle of a parametric pendulum. In this case we consider a pendulum that is moved up and down at the the point of the suspension. If the motion of this point is given by $z(t) = -H\cos(2\omega t)$, the equation of motion takes the form:

$$\frac{d^2}{dt^2}\theta + \gamma\frac{d}{dt}\theta + \frac{1}{l}\Big(g + H\omega^2\cos(2\omega t)\Big)\sin(\theta) = 0 \tag{3.1}$$

where I denotes the length of the rope, g the acceleration of gravity, γ the coefficient of friction and H and ω the amplitude and frequency of the excitation, respectively. In this model we neglect the weight of the rope and we consider the point mass approximation.

This system may be seen as the usual pendulum equation,$(d^2/dt^2)\theta + (g/l)\sin(\theta) = 0$, plus two addition terms. The first one, $\gamma(d/dt)\theta$, is

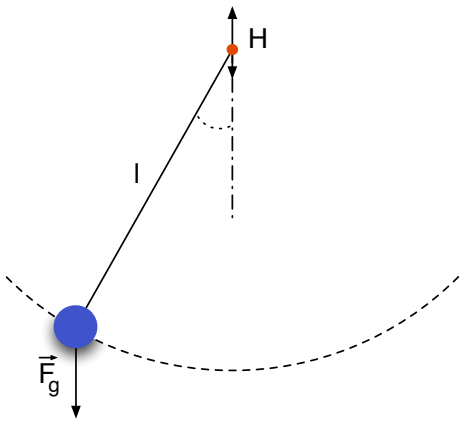

Figure 3.2: Scheme of the a parametric pendulum. We consider a case of pendulum that is moved up and down at the the point of the suspension.

related to damping of the system due to the viscosity of the fluid surrounding the weight. The second term is the driving excitation which, in this case, can be seen as a modulation of the gravitational acceleration g.

In this analysis we use the additional approximation of small angles and so we are allowed to use the approximation: $\sin\theta \sim \theta$. In this regime, and taking $G(t) = g + H\omega^2\cos(2\omega t)$, we can rewrite Eq. 3.1 in the form:

$$\frac{d^2}{dt^2}\theta + \gamma\frac{d}{dt}\theta + \frac{G(t)}{l}\theta = 0 \tag{3.2}$$

In a first approach let us consider that the system is not damped, i.e. $\gamma = 0$. In this case we have:

$$\frac{d^2}{dt^2}\theta + \frac{G(t)}{l}\theta = 0 \tag{3.3}$$

This equation is formally identical to the harmonic oscillator with a resonance frequency of $\omega_0 = \sqrt{g/l}$, except that G depends explicitly on time. For this reason we call this oscillator a parametric oscillator. The solutions of this kind of equations are not trivial. Nevertheless, given that $G(t)$ is periodic this differential equation takes the name of Hill. Furthermore, since $G(t)$ is also circular it can be further reduced to the well known Mathieu equation.

In this parametric regime the solutions of the differential Eq. 3.3 are of the form:

$$\theta = e^{\mu t} u(t) \tag{3.4}$$

where $u(t)$ is a periodic function of time[45]. Instability domains, corresponding to $\mu > 0$, can form in the frequency-amplitude plane of $G(t)$. Inside such instability domains, the oscillation amplitude is considerably increased with respect to the harmonic regime, and this phenomenon is at the origin of the amplification of parametric oscillators, such as for the 'Botafumeiro' .

It is well known that for $H = 0$ we have the solution of the harmonic oscillator: $\theta = \theta_0 \cos(\omega t + \phi)$. Here, we argue that for a reason of continuity, if H is close to 0, the solution of Eq. 3.3, θ, should be approximately given by:

$$\theta \sim e^{\mu t} \cos(\omega t + \phi) \tag{3.5}$$

Substituting Eq. 3.5 in Eq. 3.3 and making zero the terms on ωt we obtain a set of two coupled equations:

$$\Big(\omega_0^2 - \omega^2 + \mu^2 + \frac{H}{l2}\omega^2\Big)\cos\phi - 2\omega\mu \sin\phi = 0 \tag{3.6}$$

$$2\omega\mu\cos\phi + \Big(\omega_0^2 - \omega^2 + \mu^2 - \frac{H}{l2}\omega^2\Big)\sin\phi = 0 \tag{3.7}$$

These two linear homogeneous equations can be further reduced to:

$$\mu^4 + 2(\omega_0^2 + \omega^2)\mu^2 + (\omega_0^2 - \omega^2)^2 - \frac{H^2}{l4}\omega^4 = 0 \tag{3.8}$$

This 4^{th} order equation in μ may be seen as a 2^{th} order equation in μ^2. Simple examination lets us conclude that this equation has two real solutions, one negative and the other positive, corresponding to the domains where the system is stable and unstable, respectively. The solution of Eq. 3.3 is unstable if μ^2 is positive. In this case, for $\mu^2 > 0$, we obtain the following condition:

$$\frac{H}{l} > 2\left|\frac{\omega_0^2}{\omega^2} - 1\right| \tag{3.9}$$

Analogous analysis may be drawn for the case where the damping factor, β, is not zero. Using the variable $y = \theta \exp(\beta t/2)$ we obtain:

$$\frac{d^2y}{dt^2} + \left(\frac{G(t)}{l} - \frac{\gamma^2}{4}\right) y = 0 \tag{3.10}$$

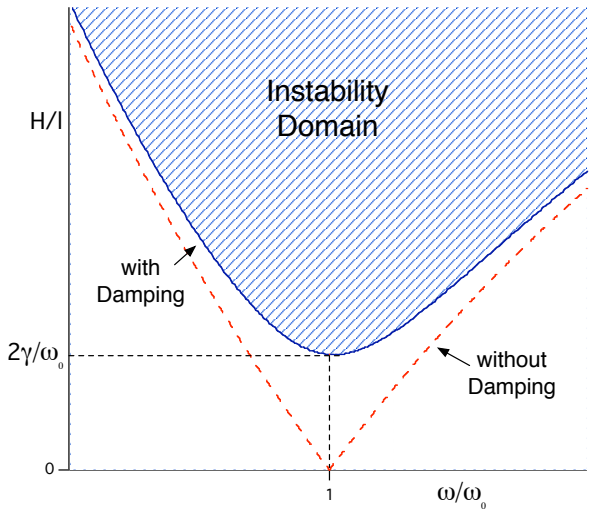

Figure 3.3: Instability domains, calculated using Eq. 3.9 and Eq. 3.13. We see that in the frequency-amplitude plane the instability domains have tongue shape around the resonance frequency ω_0.

which can be further cast into the form:

$$\frac{d^2y}{dt^2} + \alpha(t)y = 0 \tag{3.11}$$

where $\alpha(t) = G(t)/l - \gamma^2/4$ is also periodic and circular. As defined earlier Eq. 3.11 is also a Mathieu equation and the previous calculation can be repeated. We obtain, after some calculation, that in this situation Eq. 3.9 is rewritten in the form:

$$\frac{H^2}{l^2 4} > \left(\frac{\omega_0^2}{\omega^2} - 1\right)^2 + \left(\frac{\omega_0}{\omega}\right)^2 \left(\frac{H}{\omega_0}\right)^2 \tag{3.12}$$

Hence at the resonance frequency the system becomes unstable only if:

$$\frac{H}{l} > \frac{2\gamma}{\omega_0} \tag{3.13}$$

The difference between the two situations can be better seen in Fig. 3.3. In this figure we draw the instability domains, calculated from Eq. 3.9 and Eq. 3.13. We see that in the frequency-amplitude plane the instability domains have tongue shape around the resonance frequency ω_0. It can be demonstrated that similar tongues for the frequencies $\omega = 2\omega_0/n$, with n integer, may be found.

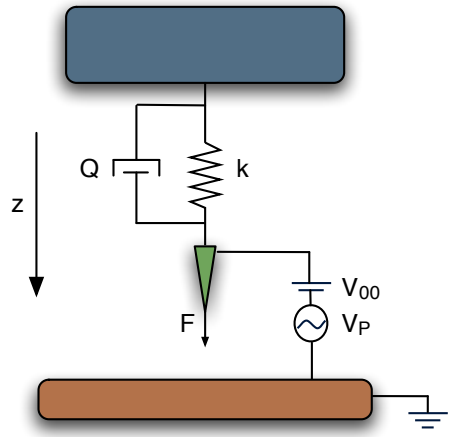

Figure 3.4: Scheme of the our experimental apparatus in the point mass approximation.

3.2.2 Numerical approach

As shown in the previous section, a parametric system may be driven into unstable regime. Here, we will use a numerical approach to explore the instability domains of the parametric system, so that we can find conditions suitable for charge detection.

In Fig. 3.4 we illustrate our model to describe the dynamics of an AFM probe under the influence of an electric field. As in Chapter 1, we model the cantilever as a harmonic oscillator. Indeed, the equation of motion of a cantilever is much more complex [46]. In general, the equation of a flexural cantilever should be taken. In this case, the dynamics of a cantilever is described by a fourth order equation and, when working at high frequencies, the entire spectrum of frequencies should be considered [47]. Nevertheless, the motion of the cantilever may be substantially simplified if the investigated frequencies remain much lower than the second flexural mode of the cantilever[48]. In the case of a rectangular beam the ratio between the two first modes is 6.267 and in order to probe parametric phenomena we use frequencies up to two times the fundamental resonance frequency of the cantilever.

In our model the oscillator is driven by both an external driving force $F_p(t)$ resulting from a piezoelectric bimorph and an electric force $F_{el}(t)$ exerted via the scanned substrate. The substrate is modelled as a metal plane above which a fixed charge Q_F can be located, at a given distance z_1 from the metal plane. The equation of the cantilever

motion is:

$$\frac{d^2}{dt^2}z(t) + \frac{\omega_0}{Q}\frac{d}{dt}z(t) + \omega_0^2 z(t) = \frac{F_{piezo}(t)}{m^*} + \frac{F_{el}(z,t)}{m^*} \tag{3.14}$$

with cantilever displacement $z(t)$, spring constant k_0, mass m^* and quality factor Q. The resonant frequency ω_0 is given by $\omega_0^2 = k_0/m^*$.

The capacitive force F_{el} between tip and surface is given by [49]:

$$F_{el} = \frac{1}{2}\frac{\delta C}{\delta z}(V + \Phi_{ST} + V_C)^2 \tag{3.15}$$

where Φ_{ST} denotes the work function difference between the metal plane and the metallized cantilever and C is the capacitance between the substrate and the cantilever. $V(t)$ represents the voltage applied to the substrate, while V_C is an equivalent voltage which results from the presence of the fixed charge. In the case of a plane-plane geometry, Eq. 3.15 becomes:

$$F_{el} = \frac{\epsilon S}{2}\left(\frac{V + \Phi_{ST} + \frac{Q_F z_1}{\epsilon S}}{z + z_0}\right)^2 \tag{3.16}$$

where ϵ is the dielectric constant of the medium between the metal plate and the tip. The average distance z_0 accounts for the position of the conducting plane set on a defined potential. A development of the electrical force to first order in z turns Eq. 3.14 into:

$$\frac{d^2 z}{dt^2} + \left(\omega_0^2 - \frac{1}{m^*}\frac{\delta F_{el}}{\delta z}\right)z + \frac{\omega_0}{Q}\frac{dz}{dt} = \frac{F_{pieso}(t)}{m^*} + \frac{F_{el}(0,t)}{m^*} \tag{3.17}$$

If the applied voltage V is an arbitrary periodic signal with pulsation ω and period T, the homogeneous equation of motion has thus the form:

$$\frac{d^2 z}{dt^2} + (\omega_0^2 - g(t))z + \beta\frac{dz}{dt} = 0 \tag{3.18}$$

with $\beta = m\omega_0/Q$. Due to the periodicity of V, $g(t)$ is also a periodic function of time. As in the last section we change the variable to $y = z.\exp(\beta t/2)$ and we obtain:

$$\frac{d^2 y}{dt^2} + \alpha(t)y = 0 \tag{3.19}$$

where $\alpha(t) = \omega_0^2 - \beta^2/4 - g(t)$. This equation is formally equivalent to Eq. 3.3. If $\alpha(t)$ is a simple sine function, this equation is a Mathieu equation.

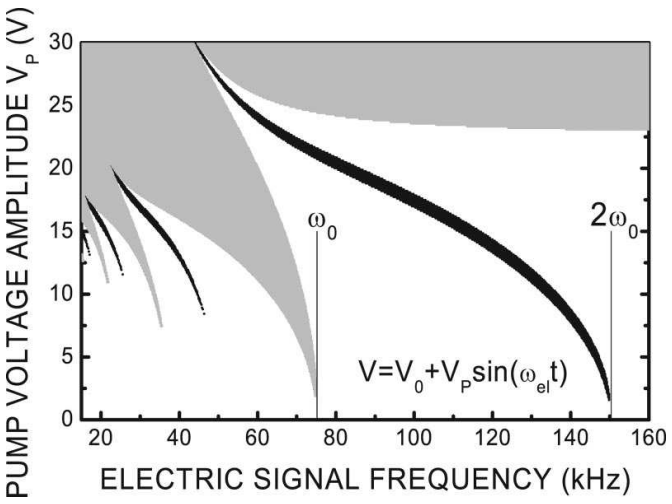

Figure 3.5: Instability domains in the electric signal frequency-pump voltage plane, as calculated by applying the stability criterion to a sinusoidal electric signal. Parameters: S=2.25×10^{-14} m^2, m^* = 10^{-11} kg, k=2.23 N/m, Q=300, 150 fixed elementary charges located under the surface 25 nm and distance tip surface of 50 nm

It is well known that Mathieu equation is formally similar to a one-dimensional Schrödinger equation with a periodic sine potential (replace t by x). Indeed, determining the instability domains of Eq. 3.19 is formally identical to determine the energy band structure of an arbitrary one-dimensional periodic lattice. Moreover, it is of great interest to solve Eq. 3.19 for any arbitrary signal, as electric losses in the substrate changing the signal shape might have to be accounted for, or the use of electric pulses might be favorable.

Fig. 3.5 is a map of the instability domains in the voltage-frequency plane with the set of physical parameters listed in the figure caption. In this calculation we have transposed a method originally proposed by Lee and Kalotas in the case of the Schrödinger equation [50]. This analysis has been done by T. Ouisse. Few more details may be found in [33]. The black domains show the instability areas for a fixed charge equal to 150 elementary charges. In contrast, the superimposed grey domains are calculated for the same structure free of any fixed charge. In both cases the electrical signal is sinusoidal. The grey domains which are only due to the alternative part $V_P\sin(\omega_{el}t)$ of the signal are almost the same in both cases, and superimposed. The highest frequency instability tongue due to V_P is obtained for $\omega_{el} = \omega_0$, since it gives a force component oscillating at $2\omega_0$. In contrast, adding a

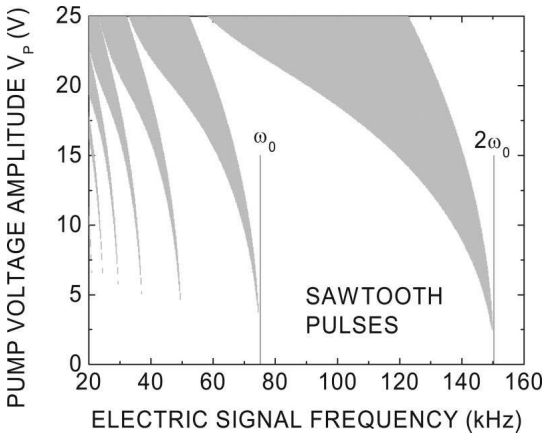

Figure 3.6: Instability domains in the electric signal frequency-pump voltage plane, as calculated by applying the stability criterion to a sawtooth electric signal with a linearly rising part and an abrupt falling part. Here V_P is defined as the amplitude of the sawtooth pulse and the base level is equal to 0 V. Parameters: S=2.25×10^{-14} m^2, m*=10^{-11} kg, k=2.23 N/m, Q=300, no fixed charges.

constant offset through the introduction of the fixed charge gives rise to a force component at ω_{el}, and a new instability tongue thus appears at $\omega_{el} = 2\omega_0$. This is also quite clear in Fig. 3.6, for which the signal is now a sawtooth periodic voltage. For low voltage values the two first instability domains never exactly occur at ω_0 and $2\omega_0$, but rather take place at frequencies located below those values (see Figs. 3.5 and 3.6), because the resonance frequency of the cantilever is lowered by the constant part of the first order term in z of the electrical force. As detailed below, this is a favorable point for charge detection.

To enhance or lower drastically the natural oscillation amplitude of the cantilever A_0 through the action of a fixed charge or substrate voltage, the largest effect will clearly be obtained in the instability domains described above, since in such a case the oscillations are controlled by the non-linear terms in Eq. 3.14. But these oscillations can also become spontaneous and difficult to control if the tip is positioned close to the sample. Hence it is *a priori* preferable to stay out of the instability domain, but sufficiently close to it so as to remain in a parametric amplification regime, which is amenable to analytical calculations. This is for instance the case if one takes a sinusoidal signal with an electrical pulsation $\omega_{el} = 2\omega_0$. As illustrated by Fig. 3.5 for $\omega_{el} = 2\omega_0$, as V_P increases from zero to upper values, one progressively gets closer to

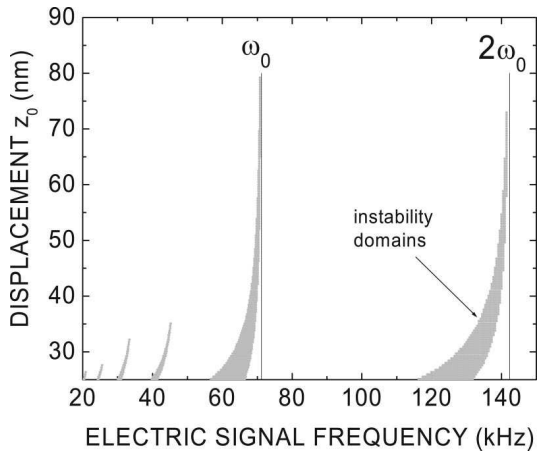

Figure 3.7: Instability domains in the electric signal frequency-pump voltage plane, as calculated by applying the stability criterion to a sawtooth electric signal with a linearly rising part and an abrupt falling part. Here V_P is defined as the amplitude of the sawtooth pulse and the base level is equal to 0 V. Parameters: S=2.25×10^{-14} m^2, m^*=10^{-11} kg, k=2.23 N/m, Q=300, no fixed charges.

the instability domain, up to a voltage above which one begins to go away from it. We thus expect an optimal amplification at a precise V_P value. A similar behaviour is obtained in the frequency-position plane, as shown by Fig. 3.7. We will show that all quantities of interest can be accurately approached by simple analytical expressions.

3.3 Cantilever Oscillation with $\omega_{el} = 2\ (\omega_0 + \Delta\omega)$

3.3.1 Theory

In this section, we derive the gain in amplification obtained in the case of a sinusoidal electrical excitation $V(t) = V_0 + V_P sin(2(\omega_0 + \Delta\omega)t)$, with $\Delta\omega$ small against ω_0. Here, V_0 includes either an offset voltage, a work function difference, a fixed charge or a combination of the three terms. We will follow below an analysis very similar in spirit to that conducted by Rugar and Grütter in ref.[32]. As in [32], we introduce a new complex variable:

$$a = \frac{dz}{dt} + j\omega_1^* z \tag{3.20}$$

$$a^* = \frac{dz}{dt} + j\omega_1 z \tag{3.21}$$

with

$$\omega_1 = \omega_0 \left(\sqrt{1 - \frac{1}{4Q^2}} + \frac{j}{2Q} \right) \tag{3.22}$$

from which the following inverse relations can be obtained:

$$z = \frac{a - a^*}{j(\omega_1 + \omega_1^*)} \tag{3.23}$$

$$\frac{dz}{dt} = \frac{\omega_1 a - \omega_1^* a^*}{\omega_1 + \omega_1^*} \tag{3.24}$$

Substituting Eq. 3.23 and Eq. 3.24 into Eq. 3.14 then yields:

$$\frac{da}{dt} = j\omega_1 a + j\frac{k_p(t)}{m^*}\frac{a - a^*}{\omega_1 + \omega_1^*} + \frac{F_{piezo}(t)}{m^*} + \frac{F_{el}^0(t)}{m^*} \tag{3.25}$$

where $k_p(t)$ is the modification of the spring constant induced by the electrical force and $F_{el}^0(t)$ is the zeroth order term in z of the electrical force, depending on z_0 . Eq. 3.25 is similar to what was already obtained by Rugar and Grütter. However, we will not neglect any term in the first order expression of the electrical force as made in [32]. We state additionally that the piezoelectric stimulation is ensured at a frequency half of the electrical excitation, so that parametric amplification acts on the piezo-electric oscillation:

$$F_{piezo}(t) = F_0 \sin\left((\omega_0 + \Delta\omega)t + \Phi\right) \tag{3.26}$$

Here we note an important difference with the treatment already given in ref.[32]: the authors assume that the frequency ω_0 involved in their equations is not the natural resonance frequency of the free cantilever, but rather the resonance frequency obtained with an offset voltage V_0 and pump voltage V_P already applied between the substrate and the cantilever. In other words, they implicitly include the constant part of $k_p(t)$ in the spring constant of the original system, and neglect the variation of the quality factor, which is also a function of V_0 and V_P. In their case, imposing $\omega_{el} = 2\omega_0$ means that the signal lies exactly below the instability tongue, so that as the pump voltage is increased, the gain continuously grows until spontaneous oscillations appear. They also make the hypothesis that the pump voltage remains negligible in front of the offset voltage, which is maintained constant (as achieved in their experiment). Here, we seek a general solution for an arbitrary frequency around $2\omega_0$, and arbitrary voltages. As a

consequence, our calculation results will also be different from that of ref.[32]. Looking for a steady-state oscillation component of the form $a = a_0 \exp(j(\omega_0 + \Delta\omega)t)$, Eq. 3.25 leads to:

$$j(\omega_1 - \omega_0 - \Delta\omega)a_0 - \frac{ja}{m^*(\omega_1 + \omega_1^*)} \times$$

$$\times \left[\left((V_0^2 + \frac{V_p^2}{2}) a_0 - \frac{V_0 V_p}{j} a_0^* \right] + \frac{F_0}{2m^*} e^{j(\Phi + \frac{\pi}{2})} = 0 \right. \tag{3.27}$$

where:

$$\alpha = \frac{1}{2} \frac{\delta^2 C}{\delta z^2} \tag{3.28}$$

We note that to first order in $1/Q$, $\omega_1^* + \omega_1 \simeq 2\omega_1$ and $\omega_1^* - \omega_1 \simeq j\omega_0/2Q$ [13], we define:

$$\beta_1 = \frac{\omega_0}{2Q} \tag{3.29}$$

$$\beta_2 = \alpha \frac{V_0^2 + \frac{V_p^2}{2}}{2m^*\omega_0} \tag{3.30}$$

$$\beta_3 = \frac{\alpha V_0 V_P}{2m^*\omega_0} \tag{3.31}$$

$$A_0 = \frac{F_0 Q}{m^*\omega_0^2} \tag{3.32}$$

where A_0 is the free amplitude of the cantilever, already defined in Chapter 1 (Eq. 2.5), *i.e.* when $V_0 = V_P = 0$ V. We find after some calculation that a_0 can be expressed as:

$$a_0 = \frac{A_0\omega_0^2}{2Q} \frac{(\beta_1 + \beta_3)\sin\Phi - (\beta_2 + \Delta\omega)\cos\Phi}{\beta_1^2 + (\beta_2 + \Delta\omega)^2 - \beta_3^2} -$$

$$-j \frac{A_0\omega_0^2}{2Q} \frac{((\beta_2 + \Delta\omega)\sin\Phi + (\beta_1 - \beta_3)\cos\Phi)}{\beta_1^2 + (\beta_2 + \Delta\omega)^2 - \beta_3^2} \tag{3.33}$$

so that the oscillation amplitude A at $\omega_0 + \Delta\omega$ is:

$$A = \frac{A_0\omega_0}{2Q} \frac{\sqrt{\beta_1^2 + (\beta_2 + \Delta\omega)^2 + \beta_3^2 - 2\beta_3(\beta_1\cos(2\Phi) + (\beta_2 + \Delta\omega)\sin(2\Phi))}}{\beta_1^2 + (\beta_2 + \Delta\omega)^2 - \beta_3^2} \tag{3.34}$$

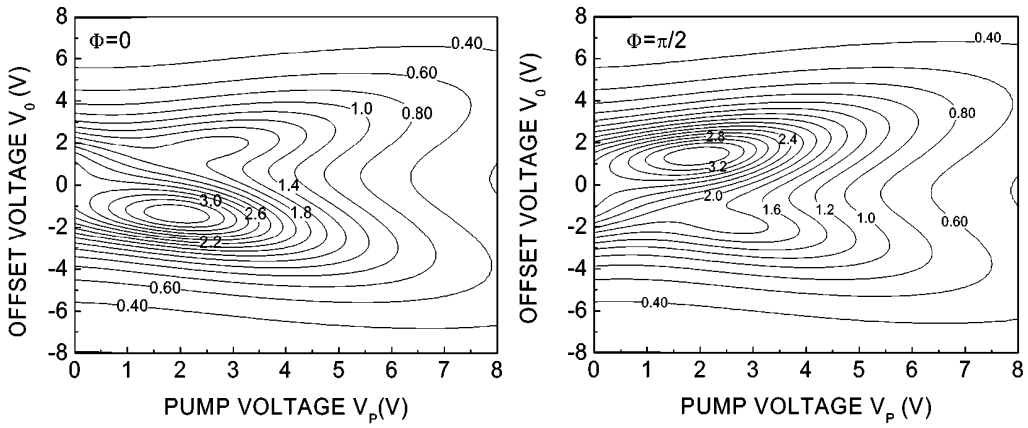

Figure 3.8: Oscillation amplitude in the pump voltage V_P offset voltage V_0 plane, as calculated in Eq. 3.34. The iso-amplitude line values are given in nm (from 0 to 4 nm with 0.2 nm steps). Parameters: $\omega_{el} = 2\omega_0$, $\omega_{piezo} = \omega_0$, S=2.25×10^{-14} m^2, z_0=50 nm, k=2.23 N/m, m^*=10^{-11} kg, Q=300, F_{piezo}=2×10^{-11} N, f_0=75.16 kHz. (a) $\Phi = 0$ and (b) $\Phi = \pi/2$.

(in Eq. 3.34, A is simply obtained from Eq. 3.33 by taking $A = |a_0|/\omega_0$).

We should notice that Eq. 3.34 can be rewritten in the form:

$$A = GA_0 \tag{3.35}$$

where G is a gain that contains the information concerning the electric field (and electric charges) probed by the tip. G is given by:

$$G = \frac{\omega_0}{2Q} \frac{\sqrt{\beta_1^2 + (\beta_2 + \Delta\omega)^2 + \beta_3^2 - 2\beta_3(\beta_1 \cos(2\Phi) + (\beta_2 + \Delta\omega)\sin(2\Phi))}}{\beta_1^2 + (\beta_2 + \Delta\omega)^2 - \beta_3^2} \tag{3.36}$$

It can be easily verified that for $V_0 = V_P = 0$ V and $\Delta\omega$= 0 Hz G becomes unitary. This is consistent with the fact that the parametric excitation intervenes in the form a gain G.

Eqs. 3.34 and 3.36 provide the ability to calculate analytically almost any quantity of interest in the parametric amplification condition $\omega_{el} = 2(\omega_0 + \Delta\omega)$. Formula 3.34 is different from its counterpart derived in [13], since, as we will see below, A does not necessarily go to infinity when increasing V_P. Besides, for arbitrary V_P and V_0 values, the maximum amplitude is in general not obtained for a phase shift $\Phi = \pi/2$, as in [13]. This can be seen in Figs. 3.8 (a) and (b), where the amplitude of the oscillations has been plotted in the (V_0, V_P) plane

for $\Phi = 0$ and $\pi/2$, respectively, and $\Delta\omega = 0$, the other parameters being analogous to that chosen in Fig. 3.5. In many areas the amplitude with $\Phi = 0$ is larger than with $\Phi = \pi/2$.

From Eq. 3.34 it is straightforward to derive that if the condition:

$$\frac{\delta^2 C}{\delta z^2} > \frac{2k}{Q|V_0 V_p|} \tag{3.37}$$

is fulfilled, *i.e.* if the tip position gets close enough to the sample, then the analytical gain goes to infinity if $\Delta\omega$ is comprised in a frequency interval given by the bottom and upper limits written below:

$$\Delta\omega_\infty^\pm = \frac{1}{2m^*\omega_0}\left[-\alpha\left(V_0^2 + \frac{V_P^2}{2}\right) \pm \sqrt{\alpha^2 V_P^2 V_0^2 - \frac{k^2}{Q^2}}\right] \tag{3.38}$$

For a sinusoidal electrical excitation, those two limits analytically define the instability domains described in a more general way in the previous section. In the case of a plane capacitor condition Eq. 3.38 becomes:

$$z < \left(\frac{4\epsilon S Q|V_0 V_P|}{k}\right)^{\frac{1}{3}} \tag{3.39}$$

An important quantity is the maximum negative frequency shift $\Delta\omega_{max}$ which can be imposed without entering into the instability domain during an approach-retract curve. Finding the value of α which minimizes $\Delta\omega_\infty^+$ and re-calculating the corresponding frequency shift leads to:

$$\Delta\omega_{max} = -\frac{\omega_0}{4Q}\sqrt{4\left(\frac{V_0}{V_P}\right)^2 + \left(\frac{V_P}{V_0}\right)^2} \tag{3.40}$$

Formulae 3.37, 3.38, 3.39 and 3.40 give the opportunity to precisely select voltage, position and frequency conditions for which one can get as close as desired to the instability domain. The most favorable conditions for charge or potential detection are such that the gain is maximized without entering into the domain characterized by spontaneous oscillations. The closer to the instability domain the system is driven, the more sensitive is the method. A trade-off has thus to be chosen between gain and stability. For instance, a quite safe but somewhat restrictive measuring protocol might be to choose $\Delta\omega = 0$, because the system never gets unstable and it even lends itself to a full analytical treatment. One must seek the condition for which a small

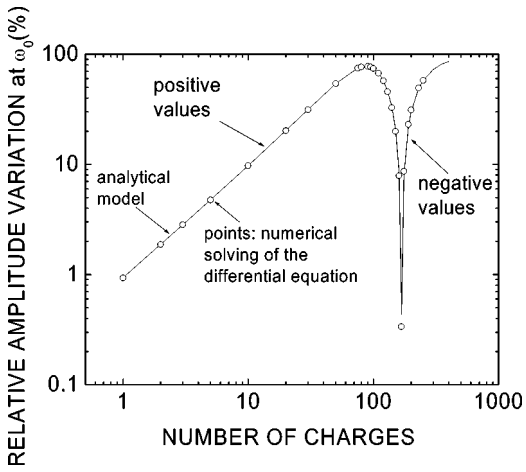

Figure 3.9: Relative variation of the cantilever oscillation amplitude at ω_0 versus the number of elementary charges added to a plane at z_1=25nm from the substrate plane. Points: numerical integration of Eq. 3.14 and solid line: analytical model. Calculation parameters: $\omega_{el} = 2\omega_0$, $\omega_{piezo} = \omega_0$, S=2.25×10^{-14} m^2, z_0=50 nm, $V_P = V_{PC}$=3.0567 V, $\Phi = -3\pi/8$, k=2.23 N/m, m^*=10^{-11} kg, Q=300, F_{piezo}=2×10^{-11} N, f_0=75.16 kHz.

variation in charge or potential (*i.e.* a change in V_0) induces the largest change in the oscillation amplitude, everything otherwise fixed. Hence one must solve $\delta A/\delta V_0 = 0$ or $(\delta A/\delta V_0)/A = 0$ if one is interested in maximizing a relative variation. But before determining this condition, we will first illustrate the precision of the analytical result through a comparison of Eq. 3.34 with a numerical integration of Eq. 3.14.

Using a Runge-Kutta method of order 4, Eq. 3.14 was integrated in a number of realistic situations with arbitrary initial conditions in z and dz/dt, and the calculation was stopped when the oscillations were getting sufficiently close to a steady-state regime (the integration time was in the 50ms range). The relative variation of A versus the number of elementary fixed charges added to the system is plotted in Fig. 3.9, with $\Delta\omega = 0$, z_0=50 nm, z_1=25 nm, V_0=0 V and $\Phi = -3\pi/8$ (as shown later on this Φ value indeed gives the highest variation for $V_0 = 0$ V). It can be seen that the agreement with the numerical calculations is excellent. Even for one elementary charge and a small surface capacitance, the variation in amplitude is around one per cent, and as the charge grows the amplitude variation goes through a maximum, which corresponds to the point closest to the instability domain. In Fig. 3.10 we simulated the variation of the amplitude with vertical displacement z_0. Once again the agreement between numerical simulation and ana-

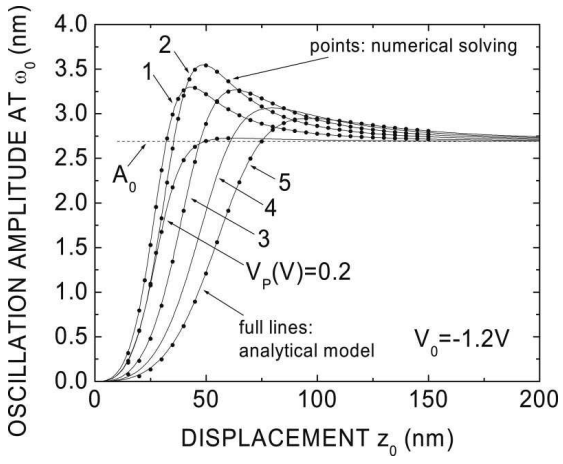

Figure 3.10: : Cantilever oscillation amplitude at ω_0 versus displacement z_0, for various pump voltage values. Points: Fourier component at ω_0 derived from a numerical integration of Eq.(1) and solid lines: analytical model. Parameters: $\omega_{el} = 2\omega_0$, $\omega_{piezo} = \omega_0$, S=2.25×10^{-14}m^2, V_0=-1.2 V, $\Phi = 0$, k=2.23 N/m, m^*=10^{-11} kg, Q=300, F_{piezo}=2×10^{-11} N, f_0=75.16 kHz.

lytical result is excellent. One can appreciate the very specific shape of the curve, which exhibits a maximum when the distance between the tip and the substrate is such that one gets to the point closest to the instability domain. As a matter of fact, all those maxima can be either numerically or analytically calculated, as we will see below.

Fig. 3.11 (a), (b) give the variation of the sensitivity in the (V_0, V_P) plane, for the same parameters as in Fig. 3.8, and for two different phase values. As illustrated by Fig. 3.11 there are always some extrema of sensitivity in the plane; they will give a maximum relative variation of amplitude if one makes a small change of offset voltage or fixed charge. In particular, and as demonstrated below, taking $\Phi = -3\pi/8$ gives rise to one maximum on the line $V_0 = 0$ V. Although in the general case the determination of the extrema requires to solve an algebric equation of order 7 in V_P, one can choose simplifying assumptions, which give the opportunity to find mere analytical expressions for all parameters. Below we will focus on the case $V_0 = 0$ V. Deriving Eq. 3.34 versus V_0 and making $V_0 = 0$ V in the resulting formula leads to the expression

$$\left.\frac{\delta A}{\delta V_0}\right|_{V_0=0} = -\frac{F_0 \alpha V_P}{4m^{*2}\omega_0^2} \frac{-\frac{\omega_0}{Q}\cos(2\Phi) + \frac{\alpha}{2m^*\omega_0}V_P^2 \sin(2\Phi)}{\left(\frac{\omega_0^2}{Q^2} + \frac{\alpha^2}{4m^{*2}\omega_0^2}V_P^4\right)^{\frac{3}{2}}} \tag{3.41}$$

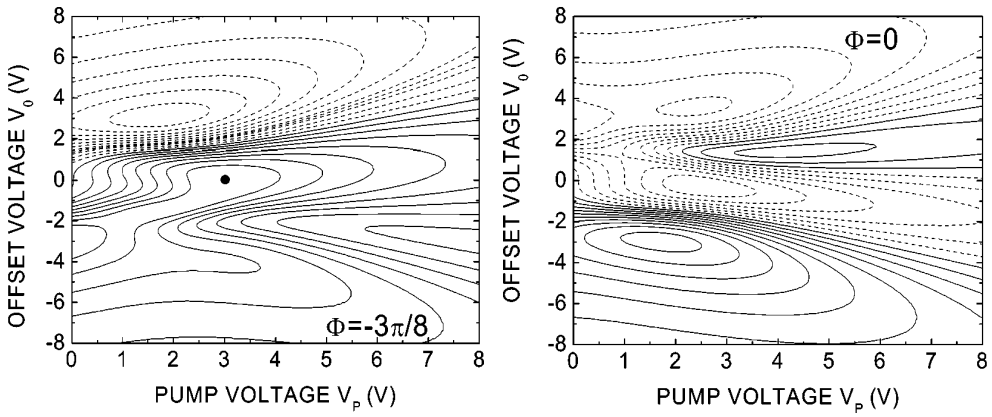

Figure 3.11: Derivative of the oscillation amplitude divided by the amplitude in the offset voltage V_0 pump voltage V_P plane, as calculated from Eq. 3.34. The solid lines are for positive values and the dashed lines are for negative values. Parameters: $\omega_{el} = 2\omega_0$, $\omega_{piezo} = \omega_0$, S=2.25×10^{-14} m^2, z_0=50 nm, k=2.23 N/m, m^*=10^{-11} kg, Q=300, $F_{piezo} = 2 \times 10^{-11}$ N, f_0=75.16 kHz. (a) Φ=-3 π/8 and (b) Φ=0. Taking Φ=-3 π/8 gives rise to a maximum on the line V_0=0 at $V_P = V_{PC2}$ (Eq. 3.46), whose position is indicated by a black point.

Eq. 3.41 exhibits a maximum versus the phase if the relationship below is obeyed:

$$V_P^2 = -\frac{2k}{\alpha Q}\tan(2\Phi) \tag{3.42}$$

Here we note that Eq. 3.42 is also the condition for a maximum sensitivity, *i.e.* a maximum of $(\delta A/\delta V_0)/A$. Substituting V_P in Eq. 3.41 by the expression above, deriving versus Φ and finding the zeroes of the resulting equation gives the conditions for which the phase and the pump voltage maximize $\delta A/\delta V_0$ at $V_0 = 0$:

$$\Phi_{C1} = \frac{\pi}{12} + n\frac{\pi}{2} \tag{3.43}$$

$$V_{PC1} = \sqrt{\frac{2k}{\alpha Q\sqrt{3}}} \tag{3.44}$$

with n integer. $\delta A/\delta V_0$ is then given by

$$\left.\frac{\delta A}{\delta V_0}\right|_{V_0=0}^{max} = \pm\frac{F_0}{2}\left(\frac{Q}{k}\right)^{\frac{3}{2}}\sqrt{\frac{3\alpha\sqrt{3}}{2}} \tag{3.45}$$

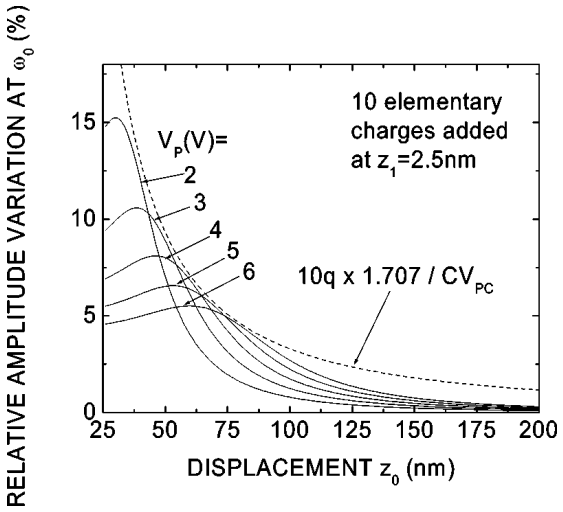

Figure 3.12: Relative variation of the oscillation amplitude at ω_0 calculated for an approach-retract curve without charge and with 10 added elementary charges. The dashed line represents the maximum variation which might be obtained by adjusting the pump voltage versus displacement z_0 according to Eq. 3.51. The two curves almost coincide when z_0 is such that $V_P = V_{PC2}$. Parameters: $\omega_{el} = 2\omega_0$, $\omega_{piezo} = \omega_0$, $S = 2.25 \times 10^{-14}$ m^2, z_0=50 nm, z_1=25 nm V_P=2,3,4,5 and 6 V, $\Phi = \pi/8$, k=2.23 N/m, m^*=10$\times^{-11}$ kg, Q=300, F_{piezo}=2$\times 10^{-11}$ N, f_0=75.16 kHz.

Quite similar conditions are obtained for maximizing $(\delta A/\delta V_0)/A$:

$$\Phi_{C2} = \frac{\pi}{8} + n\frac{\pi}{2} \tag{3.46}$$

$$V_{PC1} = \sqrt{\frac{2k}{\alpha Q}} \tag{3.47}$$

$$\frac{1}{A}\frac{\delta A}{\delta V_0}\bigg|_{V_0=0}^{max} = \pm\sqrt{\frac{\alpha Q}{k}} = \pm\sqrt{\frac{Q}{2k}\frac{\delta^2 C}{\delta z^2}} \tag{3.48}$$

For a given z_0 and $V_0 = 0$, Eq. 3.48 gives the highest possible sensitivity to a small charge or potential change which can be obtained with $\Delta\omega = 0$. Any approach-retract curve with $\Delta\omega = 0$ will give a sensitivity below Eq. 3.48. In the case of a plane capacitor model, this sensitivity varies as $z_0^{-3/2}$. Now suppose that a value of V_P has been fixed and $\Phi = \Phi_{C2}$. There is indeed a given value of z for which $(\delta A/\delta V_0)/A$ is equal to Eq. 3.48. It is worth noticing that this is not the point where a maximum sensitivity is reached in the approach-retract

curve (see Fig. 3.12 for an example). But interestingly enough, this maximum of sensitivity is located close to that value. Easy calculations show that with a fixed V_P and $\Phi = \Phi_{C2}$, the maximum sensitivity of the approach-retract curve is obtained for:

$$\alpha_C = \frac{2(1+\sqrt{2})k}{QV_P^2} \tag{3.49}$$

and then is equal to:

$$\frac{1}{A}\frac{\delta A}{\delta V_0}\Big|^{max}_{V_0=0,\Phi=\Phi_{C2}} = \left(1+\frac{1}{\sqrt{2}}\right)\frac{1}{V_P} \tag{3.50}$$

For a plane capacitor, the tip position for which this maximum is obtained is:

$$z_0^C = \left(\frac{\epsilon SQV_P^2}{2k(1+\sqrt{2})}\right)^{\frac{1}{3}} \tag{3.51}$$

A possible way to measure the equivalent voltage difference between two points or resulting from charge injection into the structure is to measure the maximum difference between the amplitude with and without charge in an approach-retract curve. The equivalent voltage difference ΔV_0^{eq} is simply given by:

$$\Delta V_0^{eq}\Big|_{V_0=0,\Phi=\frac{\pi}{8}} = \frac{V_P}{1.707} Max\left(\frac{\Delta A}{A}\right) \tag{3.52}$$

where $\Delta A/A$ is the relative oscillation amplitude variation between the two approach-retract curves. Note that the lower is V_P, the higher will be the maximum sensitivity but it will then be obtained for a closer distance between the tip and the sample, so that a trade-off must be chosen in order not to get influenced by additional forces and effects (see Fig. 3.12). The ultimate sensitivity of the method depends on this choice.

Finally we will illustrate through Fig. 3.13 the gain brought by the choice $\omega_{el} = 2\omega_0$ in comparison with the usual low frequency modulation of the cantilever oscillation which is obtained for $\omega_{el} < \omega_0$. We take $\omega_{el} = 2\pi\times$10 kHz and all other parameters equal to the ones chosen in Fig. 3.8, and we add a single fixed charge to the system at z_1=2.5 nm. Fig. 3.13 shows the power frequency spectrum of the cantilever oscillations, as calculated from a numerical integration of the equation of movement Eq. 3.14. As can be seen in Fig. 3.13 , there is an eight orders of magnitude difference between the line at 10 kHz and the line

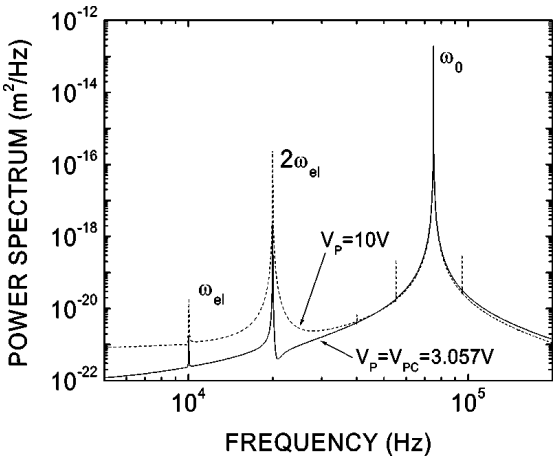

Figure 3.13: Power frequency spectrum of the cantilever oscillations as calculated from a numerical integration of Eq. 3.14 with the same parameters as in Fig. 3.8, but $\omega_{el} = 2\pi\times 10$ kHz, $V_P = V_{PC2}$=3.056 V (solid line) and V_P=10 V (dotted line).

at ω_0, the latter remaining almost unaffected by the electrical signal at 10 kHz. This is to be compared with the one per cent increase in amplitude of the line at ω_0 in the case of parametric amplification (see Fig. 3.8). Thus in this example we predict that the latter method gives a six orders of magnitude improvement in sensitivity in comparison with the former, if one takes into account all noise sources but thermal noise (to be treated in the last section). Increasing V_P so as to improve the sensitivity of the low frequency modulation does not substantially modify this ratio (case V_P=10 V in Fig. 3.13). Besides, we made our comparison in a very restrictive case ($\Delta\omega$=0). If we choose a frequency in between $2(\omega_0 + \Delta\omega_{max})$ and $2\omega_0$, the sensitivity of the parametric method can still be greatly enhanced without suffering from spontaneous oscillations.

3.3.2 Experiments

In this section we report data that are aimed at demonstrating without ambiguity the validity of the parametric amplification model, and at identifying some critical parameters which must be carefully chosen so as to put the method to good use (tip length, cantilever dimensions, etc.). The piezo-electric signal is picked up by an electronic circuit which exactly doubles the input signal frequency, with adjustable phase, offset and level outputs.

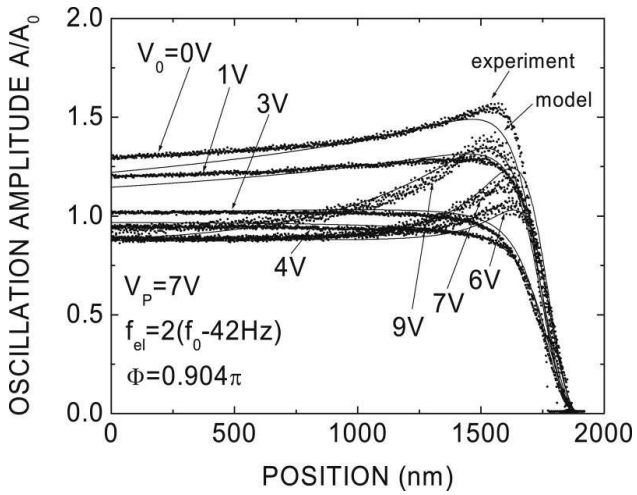

Figure 3.14: Experimental approach-retract curves of a Cu plane in parametric amplification conditions, along with their fit with the analytical model. The fitting parameters are: f_0= 57.402kHz, k=4N/m, Q=200, f_{el}=2(f_0-42Hz), f_{piezo} = f_0-42 Hz, Φ=0.904π. These parameters are either experimentally extracted (ω_0, k, Q) or chosen to be very close to the values given by the tip supplier (cantilever dimensions).

Fig. 3.14 shows typical experimental approach-retract curves, the sample being a flat copper surface, with an electric signal frequency chosen to lie slightly below $2\omega_0$. As it can be seen in Fig. 3.14, application of Eq. 3.48 with parameters either experimentally extracted (ω_0, Q, k) or chosen very close to the parameter values given by the tip supplier (cantilever dimensions, etc.) allows us to obtain very reasonable fits to the experimental curves, whatever is the offset voltage V_0. Here the capacitance is modelled as resulting from the parallel combination of a sphere+cone system (tip) and a plane capacitor (cantilever). For the tip we use the analytical electric force model proposed by Hudlet et al. [51]. It is worth noticing that a perfect fit cannot be obtained for a number of reasons: for instance we do not take into account the 10^o cantilever angle, and the sphere+cone model is only an approximation of the real geometry. Besides, the phase is also fitted because in practice there is a slight, constant de-phasing between the electric signal applied to the piezo-electric bimorph which itself excites the cantilever, and the resulting cantilever oscillation. Even with such an approximate capacitance model it is quite remarkable that the whole set of curves can be fit with only one set of parameters. Close to the sample, the capacitance is dominated by the tip contribution, but far from it the

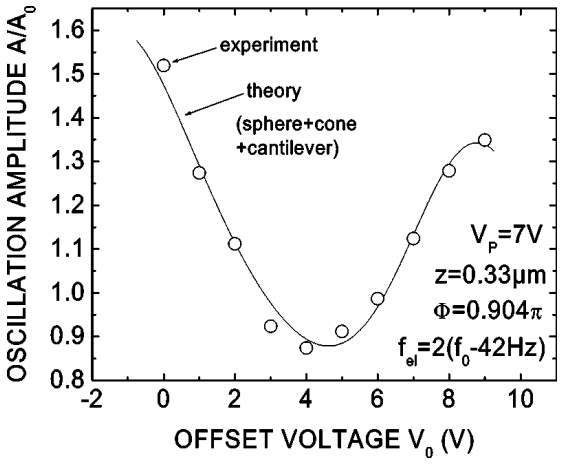

Figure 3.15: Experimental variation of the oscillation amplitude as a function of offset voltage, with the tip positioned at 0.33 μm from the sample surface. Same parameters as in Fig. 3.14.

cantilever influence prevails. Fig. 3.15 gives the variation of the oscillation amplitude versus the offset voltage, now maintaining constant the position of the tip with respect to the sample. It also illustrates the nice agreement which can be obtained between the experiment and model. It is worth noticing that if the parametric effect was ignored, and just taking into account a 'conventional' excitation close to $2\omega_0$, *i.e.* quite far from the resonance, the experimental approach-retract curves should be almost entirely determined by the piezo-electric excitation alone, and should remain almost unaffected by the sinusoidal electrical force. This is obviously not the case in Fig. 3.14.

3.3.3 Sensitivity and Thermomechanical Noise

As already noted by Rugar and Grütter [32], if one is interested in extracting data from the excitation which is parametrically amplified, there is no gain to expect from the usual thermomechanical noise limit, because both the useful excitation and the thermal fluctuations are amplified in the same way. Indeed, this conclusion can be directly extracted from Eq. 3.35 where the parametric excitation intervenes in the form of a gain G. However, in this section we wish to point out that the actual situation is somewhat more subtle, because in our case we do not want to extract information from an arbitrarily small excitation directly imposed upon the cantilever. We rather seek to obtain an information which is contained in G, and not in the excitation to be

amplified. Thus the latter can be made much larger than the thermo-mechanical noise. In this section we briefly discuss this problem, in a rather general way.

Suppose that one wants to determine the value of a physical parameter ν, which enters into the parametric force gradient, and not into the primary excitation. If A_0 is the amplitude of the piezo-electric excitation before amplification, much larger than the thermal noise amplitude A_B at $\omega_0 + \Delta\omega$, and if G is the parametric gain, a small change $\Delta\nu$ in ν leads to an overall oscillation amplitude,

$$A \simeq \left(G + \frac{\delta G}{\delta \nu}\Delta\nu\right)A_0 + GA_B \tag{3.53}$$

The lowest detectable change in ν is obtained when $GA_B = A_0\Delta\nu_{min}(\delta G/\delta\nu)$, *i.e.* increase of the thermal noise is equal to the increase of the amplitude due to the variation of the physical parameter. We obtain therefore:

$$\Delta\nu_{min} = \frac{GA_B}{\frac{\delta G}{\delta\nu}A_0} \tag{3.54}$$

It is clear from Eq. 3.54 that one can enhance the sensitivity just by increasing the piezo-electric excitation, and that ultimately the sensitivity is controlled by the maximum excitation value which can be safely chosen (for instance it cannot exceed the tip-sample distance), and by finding the conditions which maximize the relative variation of the gain with respect to the measured parameter, without entering into the spontaneous oscillation regime. To compare parametric amplification with other methods therefore requires to compare expression Eq. 3.54 with the sensitivity given by the other technique, and not to calculate the smallest, pre-amplified excitation that exceeds the thermo-mechanical noise level. To compare parametric amplification with a conventional technique, one must evaluate the minimum detectable amplitude when the force is now modulated at ω_0. The minimum detectable parameter value ν_{min} is given by $F(\nu_{min})Q/k = A_B$, and this value must be compared to that given by Eq. 3.54. In fact, in the regions where the amplification gain grows very rapidly, *i.e.* at the limit of the instability domains, it is in general always possible to find conditions for which Eq. 3.54 is indeed better than the conventional limit.

3.4 Parametric effects in Kelvin force microscopy

3.4.1 Theory

In this section we complement the previous analysis for the case $\omega = \omega_0 + \Delta\omega$, *i.e.* when the cantilever is excited electrically close to the resonance frequency of the cantilever. This experimental AFM based technique is commonly known as the Kelvin force microscopy (KFM)[52][53]. In this technique, the average distance between the tip and sample z_0 is usually maintained constant via a feedback control of the cantilever oscillation imposed by a piezo-electric bimorph. The electric force F_{el} results from the application of a sinusoidal electric signal V applied between the metallized tip and the substrate at a frequency $\omega = \omega_0 + \Delta\omega$ close to the natural cantilever resonance ω_0. Although it is not ignored that in addition to the ω component, there is also a 2ω force component (F_{el} is proportional to V^2), its effects are usually neglected. However, close to the sample, this 2ω component acts as a pump and induces parametric amplification of the ω component. Depending on the operating point, the oscillation amplitude and sensitivity may substantially depart from the expected ones.

Here, we use a analitical method analog to the one presented in the previous section to describe the parametric effects in a KFM configuration, which is validated through experiments. Furthermore, we also derive the best measurement conditions to enhance the measurement sensitivity.

As in last section, the electric force can be described as $F_{el} = (V^2/2)\delta C/\delta z$, where C is the tip/sample capacitance and $V = V_0 + V_P \sin(\omega t)$. $V_0 = V_{00} + \Delta\Phi$ is the sum of the offset voltage V_{00} and the work function difference $\Delta\Phi$ between the tip and sample. In the conventional modeling, the oscillation amplitude A due to F_{el} is proportional to both V_0 and V_P, and $\Delta\Phi$ is assessed by finding the V_{00} value which cancels the oscillation. The sensitivity can be defined as the minimum voltage V_{min} for which A exceeds the noise amplitude A_N at ω [52], $A(V_{min}) > A_N$, and if V_{min} is small this reduces to $V_{min} = A_N/(\delta A/\delta V_0)$. Hence the best sensitivity is obtained by maximizing $\delta A/\delta V_0$, with V_0 close to zero, or by minimizing the whole quantity $A_N/(\delta A/\delta V_0)$ if A_N also depends on the parameters to be tuned.

In a point-mass approximation and with a first-order development of F_{el} the cantilever equation of motion is:

$$\frac{d^2}{dt^2}z(t) + \frac{\omega_0}{Q}\frac{d}{dt}z(t) + \left(\omega_0^2 - \frac{1}{m^*}\frac{\delta F_{el}(t)}{\delta z}\right)z(t) = \frac{F_P(t)}{m^*} + \frac{F_{el}(0,t)}{m^*} \quad (3.55)$$

$z(t)$, k, m^* and Q are, as described in the last section, the cantilever

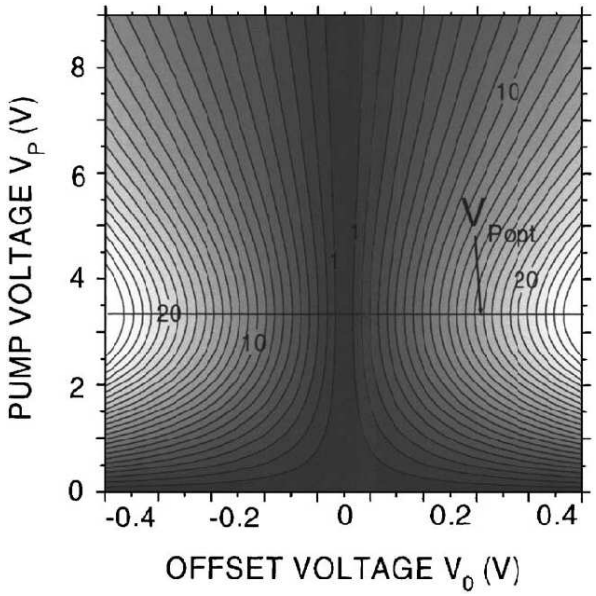

Figure 3.16: Oscillation amplitude in the V_0,V_P plane for a cantilever+tip system and a metal plane, obtained from the parametric Eq. 3.56; capacitance modelled as in [13]. Parameters: cone length 15 μm, apex radius 100 nm, cone angle 5^o, cantilever area 170×30 μm^2, tip sample distance 40 nm, k=2.5 N/m, Q=200, m^*=10^{-11} kg. Iso-amplitude lines from 1 to 25 nm, with a 1 nm spacing.

displacement, the spring constant, the mass and the quality factor, respectively. In Eq. 3.55 the periodic part of the electric force gradient is usually neglected. However, when the tip approaches the sample close enough this assumption is no longer justified, and this periodic term makes the system parametric. Hence the 2ω electric component of the force gradient may induce a parametric amplification of the forced oscillation at ω (degenerate parametric mode [12]). Following the same steps as in the previous section, *i.e.* keeping the time varying terms into the force gradient and introducing normal variables, we obtain that the oscillation amplitude at $\omega = \omega_0 + \Delta\omega$ is given by:

$$A = \frac{1}{k}\frac{2Q\gamma V_0 V_P\sqrt{1+Q^2\left(\alpha(V_0^2+V_P^2/4)/k+2\Delta\omega/\omega_0\right)^2}}{Q^2\Big(\left(\alpha V_P^2/4k\right)^2+\left(\alpha(V_0^2+V_P^2/2)/k+2\Delta\omega/\omega_0\right)^2\Big)-1} \quad (3.56)$$

where $2\alpha = \delta^2 C/\delta z^2$ and $2\gamma = \delta C/\delta z$. From Eq. 3.56 the flat-band voltage condition is still obtained by nullifying the oscillation with V_0. For small V_0, V_P and $\omega = \omega_0$, Eq. 3.56 reduces to the conventional

amplitude [52]:

$$A_{conv} = \frac{-2Q\gamma V_0 V_P}{k} \tag{3.57}$$

However, A can also substantially differ from A_{conv}. In particular, for small z_0 and large V_P, Eq. 3.56 gives:

$$A \simeq -\frac{8V_0 \frac{\delta C}{\delta z}}{3V_P \frac{\delta^2 C}{\delta z^2}} \tag{3.58}$$

which means that the amplitude can decrease with increasing V_P or when the tip gets closer to the sample (for a plane capacitor A is then proportional to z_0). This is in complete contrast with the conventional model. Besides, from Eq. 3.56, A becomes infinite if $V_P > V_{PC} = (4k/Q\alpha)^(1/2)$ and if $\Delta\omega$ is comprised in the interval given by:

$$\Delta\omega_\infty^\pm = \frac{-\alpha(V_0^2 + V_P^2/2) \pm \sqrt{\alpha^2 V_P^4/16 - k^2/Q^2}}{2m^*\omega_0} \tag{3.59}$$

As in the previous example ($\omega_{el} = 2\omega_0$) the actual motion will remain finite and it will be limited by the higher order terms neglected in Eq. 3.55. But outside the instability domain defined by $V_P > V_{PC}$ and Eq. 3.59, Eq. 3.56 is a good approximation of the real amplitude. The instability domain is not suited for KFM, because spontaneous oscillations can easily set in. But getting close to it enhances the parametric effect and substantially modifies the oscillation amplitude. This is usually the case when the tip gets close to the sample, as required for a local detection. Outside the instability domain, one can face two different situations: either $V_P < V_{PC}$ and $\omega_0 - \Delta\omega_\infty^- < \omega < \omega_0 + \Delta\omega_\infty^+$, or ω is located outside the frequency interval defined by Eq. 3.59. In the latter case, due to the parametric effect, $\delta A/\delta V_0$ does not grow indefinitely with V_P, but is maximized for a value which can be straightforwardly derived from Eq. 3.56, and is given by a fourth degree polynomial equation. Although its analytical expression is complicate in the general case, for V_0 close to zero and $\omega = \omega_0$ it reduces to:

$$V_{POPT} = 2\Big(-1 + \frac{2}{\sqrt{3}}\Big)^{1/4}\Big(\frac{k}{q\alpha}\Big)^{1/2} \tag{3.60}$$

This is illustrated by Fig. 3.16, which shows the oscillation amplitude calculated from Eq. 3.56 in the V_0,V_P plane, for a realistic parameter set and $\omega = \omega_0$. Both A and $\delta A/\delta V_0$ are higher on the line $V_P = V_{POPT}$. The parametric effect induces a profound departure from

the conventional analysis, for which the amplitude is proportional to both V_P and V_0, and the iso-amplitude lines are simple hyperbolae. Hence, in contrast to a widespread belief, the sensitivity does not continuously improve with increasing V_P, as suggested by the common (and incorrect at high V_P) amplitude formula (Eq. 3.57). Indeed, without a careful parameter choice, the real amplitude can be either better or worse than usually expected. For realistic systems, V_{PC} is in the range of a few volts. One can also choose to work in the potentially unstable frequency domain, below ω_0. Then, as long as V_P is smaller than V_{PC}, the frequency ω_M which leads to a maximum amplitude A_M is derived by maximizing Eq. 3.56. A good approximation (to a few per cent) is obtained by minimizing the denominator in Eq. 3.56. In this case we obtain:

$$\omega_M = \omega_0 - \alpha \frac{V_p^2/2 + V_0^2}{2m^*\omega_0} \tag{3.61}$$

$$V_M = \frac{8\gamma V_0 V_P (V_P^4 + V_{PC}^4)^{1/2}}{\alpha(V_{PC}^4 - V_P^4)} \tag{3.62}$$

This case is illustrated by Fig. 3.17, which depicts the variation of the amplitude with frequency for the parametric and conventional models, respectively. From the numerical solving of the differential equation using the full electric force expression $F_{el} = (V^2/2)\delta C/\delta z$ (points in Fig. 3.17), it is clear that only the parametric approach correctly captures the cantilever motion.

From the above analysis we can now suggest optimised KFM measurement conditions. If the noise limit is not imposed by thermo-mechanical noise, the fluctuations are not affected by parametric amplification, and the best sensitivity is achieved with the parameters which maximize $\delta A/\delta V_0$. Hence two KFM measurement strategies can be considered: first, one can choose a conservative approach which avoids the instability domain, with a given tip-sample distance and ω close to ω_0. Then, one must apply the optimum pump voltage $V_{POPT} = 1.254(k/Q\alpha)^{1/2}$, which only depends on the capacitance coupling between the probe and the sample and the cantilever properties. A second strategy is to work at frequencies below ω_0 and belonging to the potentially unstable range defined by Eq. 3.59. Then V_P must be kept below V_{PC}, and it is preferable to work at $\omega = \omega_M$. Such an approach is more difficult to manage, for one must avoid to enter into the instability domain, but the closer to it (*i.e.* the closest is V_P to V_{PC}), the better is the sensitivity. And this sensitivity can be made much larger than the conventional one. However, if thermo-mechanical

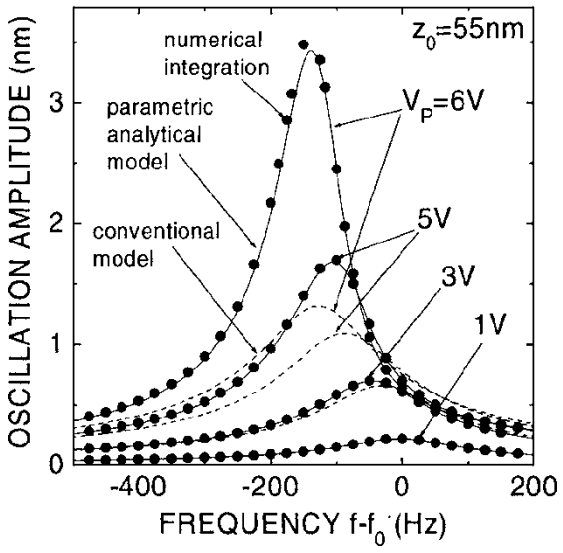

Figure 3.17: Resonance curves estimated either from a numerical integration of the full differential movement equation (points), the analytical parametric model (solid lines) or the conventional amplitude formula (dashed lines) for a tip close to the sample; plane capacitor model. Q=300, k=2 N/m, f_0=53.3 kHz, z_0=55 nm, capacitor area 0.1×0.1 μm^2.

fluctuations prevail, the noise amplitude at ω can be represented as $A_{th} = A_{th1}\sin(\omega t) + A_{th2}\cos(\omega t)$, where A_{th1} and A_{th2} are random amplitudes which vary slowly with respect to ω [32]. A_{th1} has the same phase as the electric signal and is amplified with the same parametric gain G. Hence the signal/noise ratio is not expected to change with the parametric effect, and remains the same as in a conventional analysis.

3.4.2 Experiments

To experimentally evidence this parametric effect we stabilized the tip close to the sample, and we measured the resonance curves while varying V_P. Typical results are shown in Fig. 3.18, obtained with an AFM set-up already described in the last section, and a degenerate Si substrate covered with Au. Fig. 3.18 represents the resonance amplitude A_M versus V_P, for z_0 = 55 nm (i.e. the maximum in the experimental amplitude versus frequency curves). The variation is strongly nonlinear. Following section 2.3.2, we modeled the tip-sample with a sphere + cone geometry, in parallel with a plane capacitor corresponding to the whole cantilever. The cantilever dimensions were that given by the

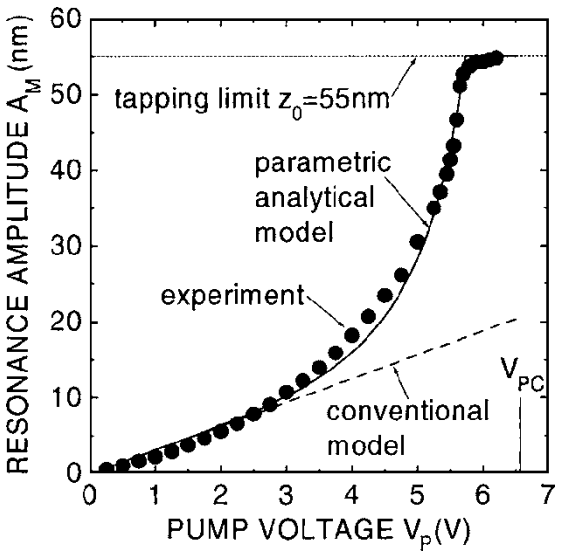

Figure 3.18: Experimental variation and fit to the resonance amplitude versus pump voltage, under ambient conditions. V_0=-80 mV, extracted parameters: k=7.3 N/m, Q=208, f_0=54.09 kHz; capacitance modelled as in [13] with tip and cantilever dimensions as given by the tip supplier, fitted apex radius r=0.34 μm.

tip supplier. k, Q and ω_0 were experimentally extracted. The apex size was adjusted (typically a few tens of nanometers). The analytical expression 3.56 gives an excellent fit to the data. Here the offset from the flat band condition is kept rather small ($V_0 \simeq$ -80 mV). Nevertheless, parametric amplification results into premature tapping around V_P=5.7 V. Without the parametric effect, tapping would have been expected at $V_P \simeq 17.5$ V. For distances larger than a few μm, the amplitude is again linear with V_P. Although such points are usually not detailed in the literature, this might explain the usual practice of operating with relatively small V_P values, which here is justified by the concern for avoiding premature tapping due to parametric amplification. Using small V_P values reduces the sensitivity, but allows one to avoid abrupt variations in amplitude. In contrast, close to the sample, working with $\omega < \omega_0$ avoids the amplitude vanishing which may result from the parametric effect. From the above analysis, it is clear that for optimizing KPFM measurements close to the sample parametric effects must imperatively be taken into account, either for avoiding or using them.

3.5 Summary and Conclusions

In this chapter we have shown that parametric amplification of a piezoelectric excitation by an electrical force may considerably enhance the sensitivity of AFM tip oscillations to small changes in charge or offset voltage between the tip and sample. Furthermore, in most interesting cases the amplification gain is amenable to accurate analytical calculations, and thus this method could lead to practical applications in EFM microscopy.

Nevertheless, here, we restricted ourselves to two Fourier components of the oscillation (ω_0 and $2\omega_0$), but in most cases the spectrum is much richer and all other components may also include useful information, and can be analytically calculated.

We want to stress that even if parametric amplification with $\omega_{el} = 2(\omega_0 + \Delta\omega)$ is not used, this phenomenon is not an academic problem, but is very relevant in practice. The force resulting from an alternating electric signal intrinsically contains two frequencies, the value of the latter being exactly twice that of the former. Hence in EFM with sinusoidal electric excitation close to ω_0 there is always parametric amplification, and its effects must be carefully analyzed, depending on the measurement conditions.

This study made us conclude that, in contrast to a widespread belief, the ω component of the cantilever oscillation is not at all independent of the 2ω component of the electric force. We found that in KFM, the parametric effect prevails and determines the oscillation amplitude whenever the tip gets close to the sample. Furthermore, in the case of $\omega = 2\omega_0$, we also showed that calculating the thermo-mechanical noise limit is not as simple as with conventional techniques.

Chapter 4

Scanning Gate Microscopy of Quantum Rings

Contents

4.1 Introduction

In the last two decades there has been a great interest in the electronic properties of the so-called mesoscopic systems [9][54]. This field was motivated by the technological need for reducing the size of the electronic circuits. This field tries to find answers to two questions:

- What are the novel physical properties when the size of electronic circuits is reduced?

- How can we take advantage from this new physical properties to build new electronic devices?

The mesoscopic physics deals, therefore, with systems that are much larger than single atoms but whose electronic properties differ from macroscopic samples. The word mesoscopic is derived from the greek and denotes this characteristic. 'Mesos' means 'middle' or 'intermediate' while 'skopien' means 'to look'. Indeed, new peculiar transport properties appear at small dimensions, that are normally masked for large samples. In this kind of devices signatures of electron interferences, such as Aharonov-Bohm (AB) interferences, that we are going to see later, are observed.

Traditionally the study of these structures is done via macroscopic measurements such as conductance measurements. While powerful when coupled to statistical theories, this approach fails to provide a spatially resolved image of the electronic properties.

The first attempt to obtain two dimensional images of electronic systems used scanning tunneling microscopy (STM). With the STM atomic resolution was achieved. Furthermore, only a few years after the STM invention electron interferences could be visualized in real space inside artificially confined surface structures. These structures are known in the literature as "quantum corrals" [55].

However, since they rely on the measurement of a current between a tip and the sample, STM techniques are useless when the system of interest is buried under an insulating layer, as in two-dimensional electron gases (2DEGs) confined in semiconductor heterostructures. To circumvent this obstacle, a new method was developed: the Scanning Gate Microscopy (SGM) [56][57][58][59].

In SGM experiments, instead of injecting a current, the tip is used to perturb capacitively the sample. The principle is to use the tip as a flying gate to perturb locally the potential experienced by electrons within a device[60][61]. Changes in the electronic properties are measured indirectly by recording the conductance of the sample at every perturbed point.

During this thesis we used a low temperature AFM, described in chapter 1, to study the electronic transport inside a model system widely known in literature: an open quantum ring (QR) [62][63]. These experiments together with quantum mechanical simulations have permitted us to understand the mechanisms behind the formation of SGM conductance images. We intend to develop an experimental technique parallel to STM that would permit to probe the electron density in devices buried a few nanometers under a surface.

This section is organized as follows:

- In section 3.2, we briefly introduce the readers to the electronic transport inside a quantum ring and to the Aharonov-Bohm effect;
- In section 3.3, previous SGM experiments found in literature are summarized and our experiments are situated in the SGM field;
- Samples and experimental setups are described in section 3.4;
- In section 3.5, experimental results are analyzed and compared with quantum mechanical simulations.

At the end, conclusions are drawn and future perspectives are anticipated.

4.2 Electronic Interferences inside a Mesoscopic Structure

2DEGs are among the most popular mesoscopic systems and their basic properties are very well documented in many reference books (*e.g.*[64]). They form at heterointerfaces in layer semiconductor structures. Fig. 4.1 represents the energy diagram at the bottom of the conduction band in a typical heterostructure, as a function of the distance from the surface. There we can notice a triangular-shaped well at the interface between the two materials, originating from large differences between their band gaps and the alignment of the Fermi levels in the two materials. Electrons from nearby impurities are transferred to the well where they form a thin conducting film (the 2DEG), leaving the charged impurities behind them. With such a method extremely high electron mobilities can be reached. Additionally, the confinement of the electron systems to a very thin plane implies that electrons occupy a discrete number of energy levels, or subbands. In the case sketched in Fig. 4.1 only the lowest subband is populated.

In these kind of structures three fundamental characteristic lengths rule the regime of the electron transport: the Fermi wavelength λ_F, the electron mean free pass l_m and the phase coherent length L_ϕ. Mathematical derivations and formal definitions of l_m and L_ϕ can be found in many mesoscopic textbooks (such as Datta [64]). Here, we will simply explain intuitively the concepts behind these length-scales:

- λ_F is the wavelength of the electrons that contribute to the conduction inside the device. The energy of these electrons is the Fermi energy and λ_F may be calculated from the electron density (per unit of area), n_s: $\lambda_F = \sqrt{2\pi/n_s}$.

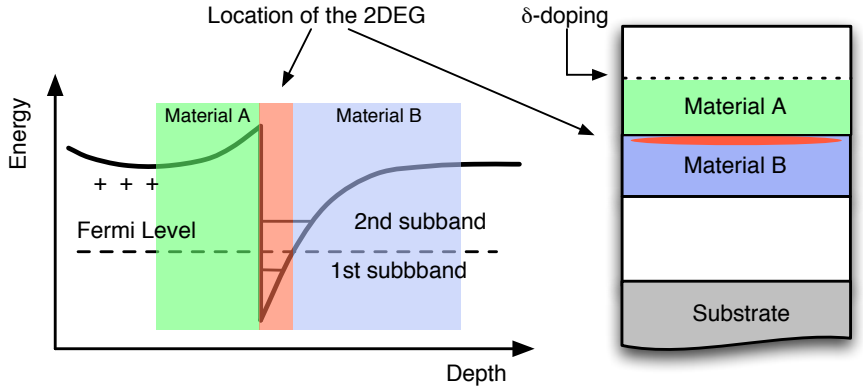

Figure 4.1: On the left we illustrate the profile of the heterostructure confining potential (sketched on the right) along the direction perpendicular to the wafer surface. Electrons given by the doping layer are transfered to the well forming, this way, a 2DEG.

- l_m reflects the irregularities in crystals that lead to scattering of the electron waves. It is defined as the average length that an electron travels before loosing its initial momentum.
- L_ϕ is directly related to the wave nature of electrons. It characterizes the phase randomization. It is defined as the average length over which an electron travels before loosing its initial phase. One should notice that an electron can change its momentum without loosing its phase coherence.

L_ϕ, λ_F and l_m are, in general, distinct and can have very different values depending on the materials and the temperature. Advances in processing technics permit, today, to produce (almost) arbitrary small samples. In our experiments the size of the device was made to be smaller than L_ϕ. In this case, the wave-like behaviour of electrons emerges and interference phenomena coming from different trajectories inside the device will eventually happen. Typical examples of these inference phenomena are universal conductance fluctuations and Aharonov-Bohm effect. In the next section we are going to describe the AB effect, which was observed in our experimental data.

4.2.1 Aharonov-Bohm effect

The original figure of the experiment proposed by Aharonov and Bohm is shown in Fig. 4.2 (a).

Their purpose was to demonstrate that 'contrary to the conclusions of classical mechanics, there exist effects of the potentials on charged particles, even in region where fields (and therefore the forces on the particles) vanish' [65]. The experiment consists in an electron beam that is split into two parts each going on opposite sides of a solenoid and then recombine to interfere. In this article it was shown that the magnetic potential provokes a phase shift of the electron wave function going through the upper (ϕ_1) and lower (ϕ_2) arms. The phase shift ($\Delta\phi$) is given by:

$$\Delta\phi = \phi_1 - \phi_2 = 2\pi\frac{e}{h}\int_S \mathbf{A}\, d\mathbf{x} = 2\pi\frac{e}{h}\Phi \tag{4.1}$$

where Φ is the magnetic flux associated with the vector potential $\mathbf{A}$ crossing the ring. As a consequence, two consecutive maxima are obtained when Φ is increased by a factor of h/e which implies a periodical oscillation of the sample conductance as a function of the magnetic field.

A particular case is obtained when the magnetic field is perpendicular to the ring surface. In this case Φ is simply the product between the magnetic field (B) and the surface within the trajectories of the electrons (S). The periodicity (T_B) is, therefore, given by:

$$T_B = \frac{h}{e\ S} \tag{4.2}$$

This means that if one knows the diameter of the trajectories it is possible to predict the periodicity of the AB effect with respect to the magnetic field.

In Fig. 4.2 (b), we show the first experimental observation of this effect in a conductor [7]. In this case, the ring was fabricated in a polycrystalline gold film of 38 nm thickness with a diameter of 764 nm. Experimental results show clear periodic oscillations of h/e.

In the same article Aharonov and Bohm predicted a similar effect using an electric potential, *i.e.* the electrical potential would also tune the phase of the electron wave function inside the ring. This particular phenomenon is known as the electric Aharonov-Bohm effect. In this case the phase shift $\Delta\phi$ provoked by an electric potential V is given by:

$$\Delta\phi = 2\pi\frac{eVt}{h} \tag{4.3}$$

where e is the elementary electric charge, h the Planck's constant and t the time during which electrons interact with the electric potential.

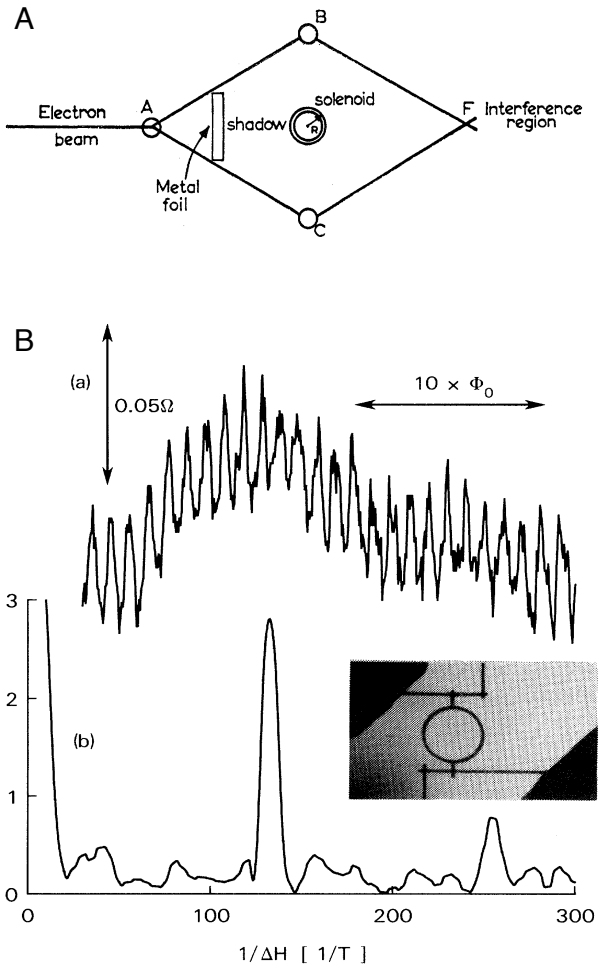

Figure 4.2: (A) is the original figure of the experiments proposed by Aharonov and Bohm [65] to demonstrate electronic interferences in a split coherent electron beam. In (B) we show the first experimental observation made in an electronic system [7].

The experimental verification in a metallic sample was done by Washburn *et. al.* [8], where the electric field was created by means of a lateral gate to the ring.

We underline that this effect can only be visible if electrons have a wave-like behaviour. In other words, electrons must be in the coherent regime. This effect is therefore a clear signature of the presence of electrons in the coherent regime. Later in this chapter, in the part devoted to the analysis of our experimental results, we use this effect as a reference.

Nowadays this kind of phenomena still interests greatly the scientific community. The objective is to build integrated electronic interferometers. Phase-controlled devices could be employed in complex coherent circuits, where phase manipulation would be exploited for complex operations [66][67].

4.3 Scanning Gate Microscopy

The SGM was born as a variation of EFM. In the last decade, AFM proved to be a very well adapted tool to study surface electric charges [22][13][14][68]. The key ingredient in this success is the localized electric field created by the sharp tip. In most experiments, such as EFM, the AFM probe is used to simultaneously perturb and measure the properties of the sample surface.

Instead, in SGM experiments, the tip is used only to perturb the sample [69]. It consists in mapping the conductance of the system as the polarized tip scans at a constant distance above the 2DEG.

Prior to our experiment, two experiments have demonstrated the ability to probe electronic transport in buried 2DEG.

The first experiment in this field was performed by Topinka *et. al.* in Harvard [56][70][71][72]. In this article, the ability of SGM to image coherent electron flow in a quantum point contact was demonstrated. The central result is illustrated in Fig. 4.3. In this experiment, use was made of a quantum point contact patterned from a GaAs/AlGaAs heterostructure that was mounted in an AFM and cooled to 1.7 K. The sample conductance versus the gate voltage on the quantum point contact measurements show clear plateaus at multiples of 2 e^2/h (the quantum of conductance). At each plateau, SGM measurements were done. The images show the first three electron modes flowing through the constriction. This observation was possible because the AFM tip functions as a local interrupter. This regime, although very successful, is limited to open 2DEG.

A further step in the study of mesoscopic devices was performed

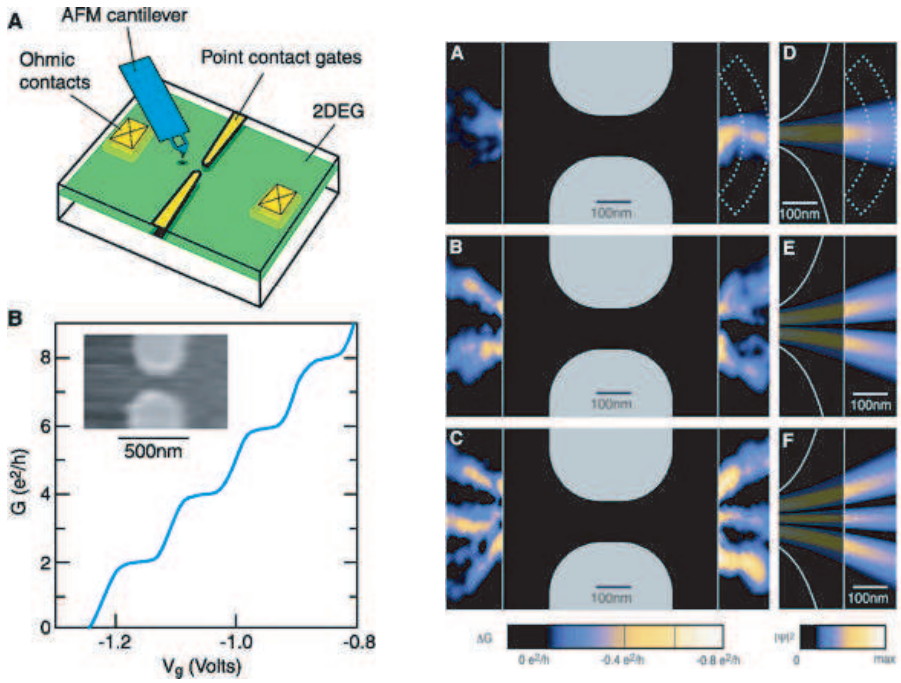

Figure 4.3: SGM experiments on a quantum point contact reported in reference [56]. On the left, (A) schematic diagram of the experimental setup and (B) conductance G versus gate voltage V_g showing clear plateaus at integer multiples of 2 e^2/h. On the right (A to C) are images of the electron flow from the quantum point contact of three increasing widths corresponding to (A) the first conductance plateau, (B) the second plateau and (C) the third plateau. These experimental results are compared with calculated wavefunctions in (D to F).

by Crook *et. al.* [73]. In this case, the system was a quantum billiard also patterned in a GaAs/AlGaAs substrate. To observe interferences the AFM probe was used in a weak perturbation regime. Illustration of the device together with the main results are shown in Fig. 4.4. Fig. 4.4 (a) and (b) are SGM conductance images of the quantum billiard in a magnetic of 42.0 and 39.1 mT, respectively. Image (c) is a high-pass filtered image of (b). These experiments demonstrate that the system is chaotic in the sense that a small change in the magnetic field, for example, strongly modifies the conductance on an arbitrarily small scale. Using geometrical considerations and a fractal analysis, the authors linked the SGM images with scarred wave functions inside a quantum billiard predicted by Akis *et. al.* in [74].

In our experiment, as we are going to see later, we studied smaller

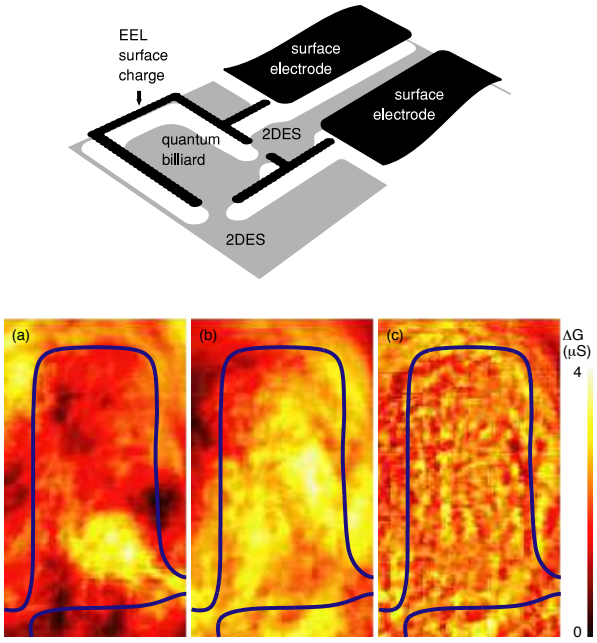

Figure 4.4: The experiment of Crook *et.al.* [73]. On the top, illustration of the 1.4 by 2.9 μm^2 quantum billiard. (a) and (b) are SGM conductance images of the quantum billiard in magnetic fields of 42 and 39.1 mT. (c) is a high-pass filtered image of (b) showing the scarred wave function inside the quantum billiard.

samples (quantum rings) where this chaotic behaviour is no longer observed. The stability of QRs contributed to the understanding of the evolution of the SGM images as the experimental parameters are swept. Furthermore, the fact that is system is not chaotic permitted us to compare experimental results with simulations.

4.4 Experiment

4.4.1 Quantum Ring

During our experiments two rings were used, which we label R1 and R2. The rings were patterned from an InGaAs/InAlAs heterostructure. This heterostructure was produced by molecular beam epitaxy (MBE) in the IEMN ('Institut d'Electronique de Microélectonique et de Nanotechnologie', Lille, France [75]) cleanrooms in the group of Alain Cappy, Sylvain Bollaert and Xavier Wallart. A scheme of the structure substrate is shown in Fig. 4.5. In this quantum structure,

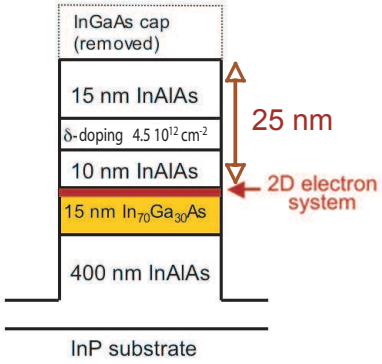

Figure 4.5: Schematic layer structure of our heterostructure.

the 2DEG is formed at the interface between InAlAs and InGaAs. It is located at 25 nm below the surface. At low temperature (4.2 K), the electron density and mobility are 2×10^{16} m^{-2} and 10 m^2/Vs, respectively. The 2DEG is filled with electrons from a doping layer situated a few nanometers above with a doping concentration of 4.5×10^{16} m^{-2}.

The rings were drawn in UCL ('Université catholique de Louvain', Louvain-La-Neuve, Belgium[76]) using e-beam lithography followed by wet etching. This procedure was done by B. Hackens (for more details see [77]). Scanning electron microscopy images of rings R2 and R1 are shown in Fig. 4.6 (a-b), respectively. The inner and outer diameters of R1 are 200 and 600 nm while in R2 the inner and outer diameters are 240 and 614 nm.

In order to test the QRs we performed magneto-conductance measurements of each ring at 4.2 K. The corresponding curves are shown under the micrographs in Fig. 4.6 (c-d). The conductances G of R1 and R2 are around 5.9 and 2.6×2 e^2/h, respectively. Since the conductance is larger than a quantum of conductance (2 e^2/h), which is the conductance for a single-mode electron flux propagating through a perfect ballistic wire, it implies that several quantum modes are populated in the device openings.

Superimposed on a broad background, periodic AB oscillations are clearly visible (inset of Fig. 4.6 (c) and (d)). This effect is better shown in the fast Fourier transform (FFT) of the magneto-conductance of R2 and R1 (displayed in Fig. 4.6 (e) and (f), respectively). This demonstrates that, at this temperature, the electronic transport through the QRs has a coherent contribution, *i.e.* electrons have a wave-like behaviour permitting electrons to interfere. Furthermore, the FFT of the magneto-conductances show several peaks where each peak corre-

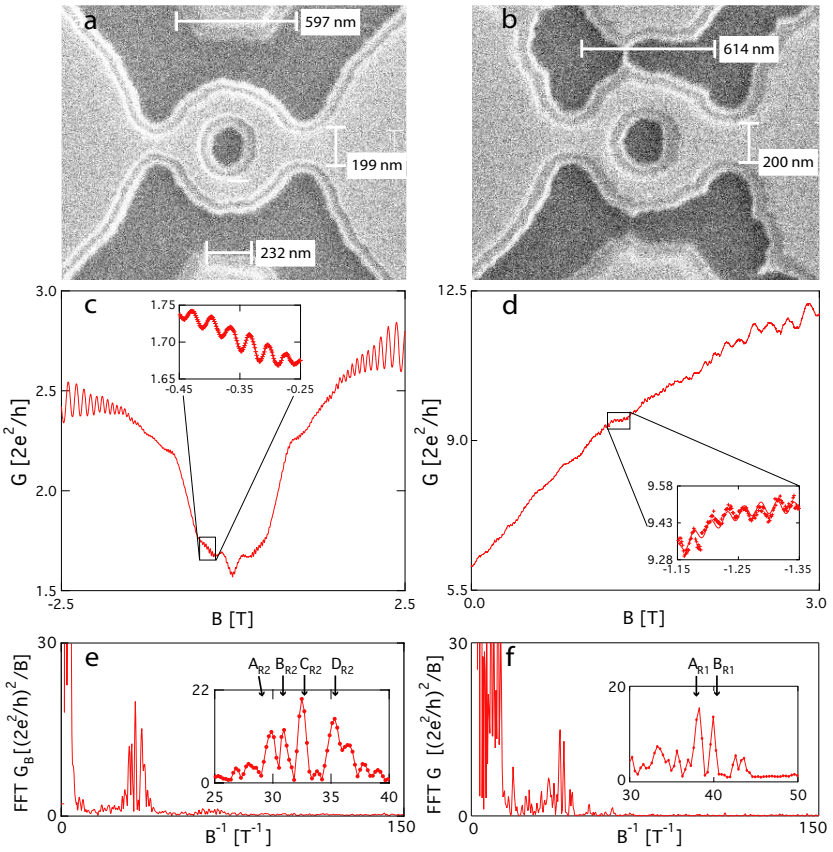

Figure 4.6: (a)-(b) show R2 and R1 electron micrographs, respectively. (c) and (d) are the corresponding magneto-conductance curves of R2 and R1. In the insets we evidence Aharonov-Bohm oscillations that are superimposed on the broad background. (e)-(f) are the fast Fourier transforms of the magneto-conductance shown in (c) and (d), respectively. The insets in (e) and (f) evidence the existence of several peaks corresponding to several circular electron trajectories inside the QRs.

sponds to a well defined circular electron trajectory inside the QRs. Concerning R1 we observe two peaks A_{R1} and B_{R1} with a corresponding periodicity of 26.1 mT and 25.0 mT. In the case of R2 we can distinguish four peaks A_{R2}, B_{R2}, C_{R2} and D_{R2} with a periodicity of 33.3 mT, 32.2 mT, 30.8 mT and 28.3 mT, respectively. Using Eq. 4.2 and the peaks developed in the FFTs of rings R1 and R2 we determine the corresponding radius of these trajectories (r_{R1} and r_{R2}, respectively). With this method we obtain that r_{R1}=[224 nm, 229 nm] and r_{R2}=[199 nm, 202 nm, 207 nm, 216 nm] which closely matches the interior of the QRs.

In the same magneto-conductance curves we can also see Shubnikov-de Haas oscillations. They start developing at a magnetic field larger than $\sim$ 2 T, *i.e.* as the cyclotron radius (calculated at 1μm for 2 T and a carrier concentration of 2×10^{16} m^{-2}) shrinks below the width of the QRs arms and openings. In this case the electrons move along the edges of the device and Shubnikov-de Haas oscillations develop.

4.4.2 Experimental Setup

Fig. 4.7 illustrates our imaging technique. A voltage V_{tip} is applied to the tip, which scans along a plane parallel to the 2DEG at a typical tip-2DEG distance (D_{tip}) of 50 nm. Due to the capacitive tip-2DEG coupling, a local perturbation is generated in the potential experienced by electrons within the QR, which, in turn, alters their transmission through the device. By recording the QR conductance as the tip is scanned over the QR and its vicinity, we build a conductance map $G(x, y)$ that reflects changes in electron transmission.

While mounting the experimental setup special care was given to the electronic noise. As shown in magneto-conductance curves in the last section, the noise level should be better than 1/1000 so that coherent effects, such as AB oscillations, may be observed. In particular, while cabling special attention was given to avoid mass-loops, which are known to increase the noise level, while connecting the several instruments. Nevertheless this action was not sufficient, it was found that the common mass of the institute was largely polluted by other instruments and other computers (of other experiments). As a consequence most of the measurements presented in this section were performed during quiet periods, *i.e.* weekends and nights.

The contact resistances to the QR are shortcut using a classical four-contact measurement. To avoid low frequency electrical noise we use an analog lock-in amplifier. We generate an alternative current (I) in the lock-in, typically around 1 kHz, that is injected in the ring. The resistive behaviour of the QR provokes a voltage drop (V) at the

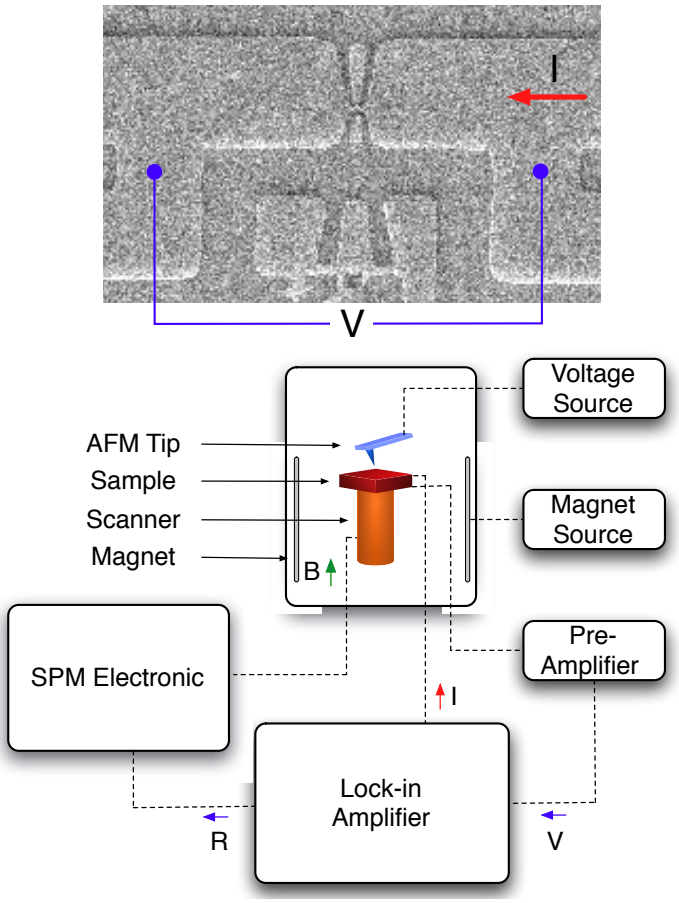

Figure 4.7: On the top we show a SEM micrograph of the quantum ring (R1) and a representation of the experimental method. A scheme of the experimental apparatus is shown below. A biased tip is used to perturb the QR while the conductance is being measured using a 4-contact technique. In the experiments the resistance of the QR is measured with a lock-in amplifier and then transfered to the SPM electronics which also controls the sample scan under the tip.

same frequency (typically some tens of microvolts). V is pre-amplified and thereafter read by the lock-in. In order to avoid heating of the electronic system by Joule effect, the current injected in the sample should fulfill the condition $eV << k_BT$. At 4.2 K we obtain that the voltage drop should be $V << 0.33$ mV. With a typical resistance of our samples of 5 kΩ the current is, in general, limited to 60 nA.

In these experiments we use, in the lock-in, a typical time constant of 100 ms. This fact limits the scan frequency of the tip over the QR. For an image of 128×128 points we use a scan frequency of 0.04 Hz (i.e., roughly 200 ms per point) and so each SGM image takes 53 minutes to build.

In Fig. 4.8 we show images at different zooms of the sample mask together with the QR. Fig. 4.8 (a) and (b) are micrographs of the sample using an optical microscope and a SEM, respectively. In Fig. 4.8 (c) and (d) we show AFM topographical images of the QR at 300 K and 4 K, respectively. In these images we can observe the four electrical contacts to the QR. Furthermore, the sample is surrounded by a surface of 200×200 μm^2 of arrows guiding towards the QR. These arrows were patterned together with the QR following the same procedure of e-beam lithography followed by wet etching.

In these experiments we follow the following routine:

- The QR is mounted at ambient conditions and electrical contacts to the sample are tested by means of measuring the resistance of the QR.
- The QR is centered under the AFM tip. At ambient condition we have optical access to the sample and we simply use a binocular microscope to perform the coarse approach.
- Afterwards, the whole system is cooled using the procedure described in section 1.4.1.
- Once at 4.2 K, the optical access to the sample is no longer available. Therefore, to approach the tip towards the sample we use the technique described in section 1.4. As stressed in the same section, this procedure lasts for one to two days.
- We locate the ring and build a topography image. Typically, it was found that, due to thermal contractions, the QR is misaligned some hundreds of μm. The ring is re-centered using the arrows drawn on the surface that guide towards the QR. This surface of 200×200 μm^2 should be, in principle, larger then the misalignment. Nevertheless, due to an unexpected large misalignment, it

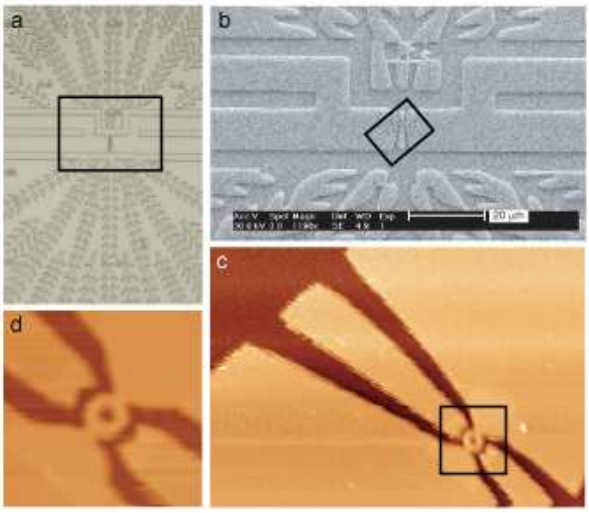

Figure 4.8: Images of the sample mask together with the QR. (a) is a micrograph of the sample using an optical microscope. (b) is a SEM image zooming over the rectangle marked in (a). In (c) and (d) we show further zooms using AFM topographical images of the QR at 300 K and 4 K, respectively. In these images we can observe four electrical contacts to the QR and a surface of 200×200 μm^2 of arrows guiding towards the QR.

happened sometimes that the arrows region was lost during the microscope cooling. In this case, we had to scan the surface of the entire sample, leading to a loss of two to three days.

- We fit a plane on the topographic image and afterwards the tip is left scanning the surface along this plane some tens of nanometers (typically 50 nm) away from the surface. To verify the parallelism between the scan plane and sample we let the tip scanning a few nanometers away from the surface while recording the fluctuations of amplitude. The parallelism is achieved when this image of the amplitude fluctuations is symmetrical.
- The laser and the alternative excitation of the lever are turned off.
- The QR ring is left stabilizing for one hour. This is necessary since the semiconductor material is very photosensitive and is disturbed by the laser beam injected into the cavity for the topography acquisition.

This strategy takes in average one week to be performed. After this procedure, we are ready to collect images of the QR conductance. In

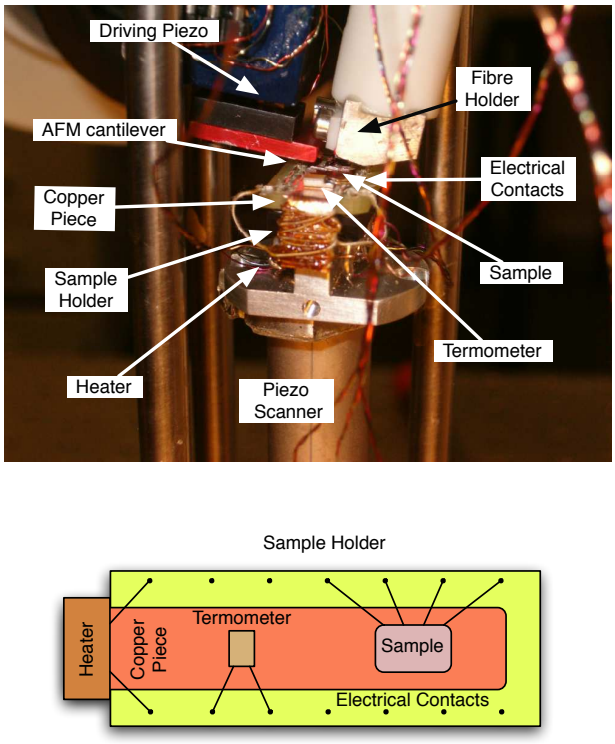

Figure 4.9: On the top, photograph of the experimental setup taken just before being cooled. In this case the system was also equipped with a thermometer and heater. On the bottom, scheme of the heating process. All three elements (heater, thermometer and sample) are glued to the same copper piece to guaranty an homogeneous temperature between them.

the next sections we are going to show and analyze the experimental results.

Heater and Thermometer

During these experiments we used a system to heat the sample. Indeed, many electronic properties are very sensitive to temperature variations [78]. By following their temperature characteristic many effects can be compared and identified.

With this in view we conceived a system adapted to enter the AFM that would simultaneously permit to heat and to measure the temperature of the sample. A photograph of the experimental setup taken just before its cooling is shown in Fig. 4.9. A schematic representation of the setup is shown at the bottom of Fig. 4.9. This system is com-

posed of three elements, all glued to the same copper piece to guaranty an homogeneous temperature. The copper piece is thereafter glued to the sample holder. The heater is a resistive wire that dissipates, by Joule effect, energy to the sample. A good thermal coupling between the sample and the thermometer is guarantied by gluing both of them with silver paint to the copper piece. The thermometer was chosen to have a high sensitivity in a temperature range of 1 K to 100 K. For this purpose we equipped our experimental setup with a CERNOX^{TM} temperature sensor made of a thin-film resistance of zirconium oxy-nitride [79].

4.5 Experimental results

As already explained, in our experiments, conductance maps are recorded while scanning the biased tip of a cryogenic AFM above the quantum ring and its vicinity. In this section we analyze the well developed patterns observed in these images. These results are presented in the following way:

- In section 3.5.1, we analyze the raw SGM data and we propose a high-pass filter adapted to isolate coherent effects.
- Afterwards, in section 3.5.2, we distinguish different types of fringes on the filtered images (concentric outside the ring region and radial inside the ring region). To evidence this different behaviour we sweep the tip voltage and a DC current injected in the QR.
- In section 3.5.3., we observe that the AFM probe induces a phase shift on the electrons crossing the ring. This effect is interpreted in terms of an electric Aharonov-Bohm effect produced between the tip and the rings arms.
- In section 3.5.4 we include quantum mechanical simulations to demonstrate that the images obtained by SGM have a strong relation with the electronic probability density inside the QR. This has permitted us to investigate the origin of concentric fringes. These results are compared with the experimental data shown previously.

At the end we summarize the achievements obtained in this experiment. The results presented in this section have recently been published in two publications [80] and [81].

4.5.1 SGM image Filtering

A typical example of a conductance map, measured in R1, is shown in Fig. 4.10. These G maps reveal a rich pattern of conductance fringes superimposed on a broad and slowly varying background.

The first contribution to the map is a broad background structure extending beyond the limits of the QR. The associated conductance scale is typically 2 e^2/h, *i.e.* almost an order of magnitude larger than the amplitude of the AB oscillations of Fig. 4.6 (c-d), indicating that the background does not originate from coherent effects. Moreover, we observe experimentally that its overall shape is strongly affected by successive illuminations of the sample which are known to affect the configuration of ionized impurities, but remains insensitive to the magnetic field B. This indicates that this background is not due to coherent effects which are known to be very B-sensitive, but related to a global shift of the electric potential in the whole quantum ring as the tip approaches the quantum ring.

A closer look to the conductance map reveals that the broad background is decorated by a more complex pattern of smaller-scale features, particularly visible in the central part of the image. We isolate these features by applying a high-pass filter, shown in Fig. 4.10 (f), on the raw conductance map. Fig. 4.10 (g) is obtained by applying such filtering on Fig. 4.10 (a).

Fig. 4.10 describes the successive steps followed to choose the cut-off frequency (f_{cut}) of the filter that we apply to our raw conductance maps. First, as we change V_{tip}, we notice that the background of the conductance map remains essentially unchanged, while the position of the small-range features is significantly affected. Therefore, after averaging over a sufficient number of conductance maps acquired with different V_{tip} (in this case seven images), the small-range features are averaged away, leaving only the background (Fig. 4.10 (b)). Thereafter, we compare the fast Fourier transform (FFT) of the averaged image (Fig. 4.10 (d)) with a typical FFT of a raw conductance map (Fig. 4.10 (c)). To better distinguish the two frequency ranges, in Fig. 4.10 (e) we show the folding of Fig. 4.10 (c) and (d) in one axe. In this figure we can clearly distinguish between two frequency ranges. The low-frequency range, where the two FFTs are essentially identical, corresponds to the broad background structure in the real-space conductance map. The high-frequency range, where the spectral content is much reduced in the averaged FFT, is related to the small-range features that we want to isolate. The cut-off frequency f_{cut} is chosen at the transition between both ranges, i.e. f_{cut}= 4 μm^{-1}. The image of the filter, in the Fourier space, is shown in Fig. 4.10 (f).

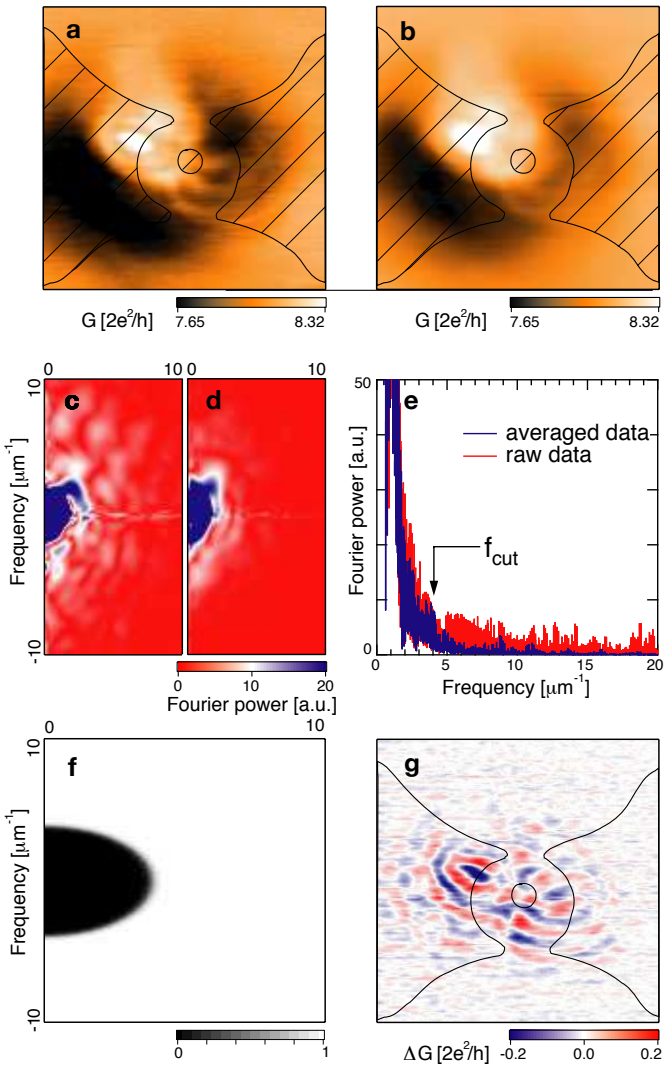

Figure 4.10: Image filtering technique. (a) conductance of the QR as a function of the tip position with V_{tip}=0.3V, tip-2DEG distance of 50nm and B=2T. (b) is the average of seven SGM images taken for different V_{tip}. (c) and (d) are the fast Fourier transform (FFT) of (a) and (b), respectively. In (e) we compare the FFTs by folding the FFT of the averaged image (d) and the FFT of a single image (c) in a plane. The cut-off frequency (f_{cut}) is chosen to isolate the high-frequency fringes superimposed to the background. From (a), using the high-pass filter with f_{cut}=4 μm^{-1} shown in (f), we obtain the image (g).

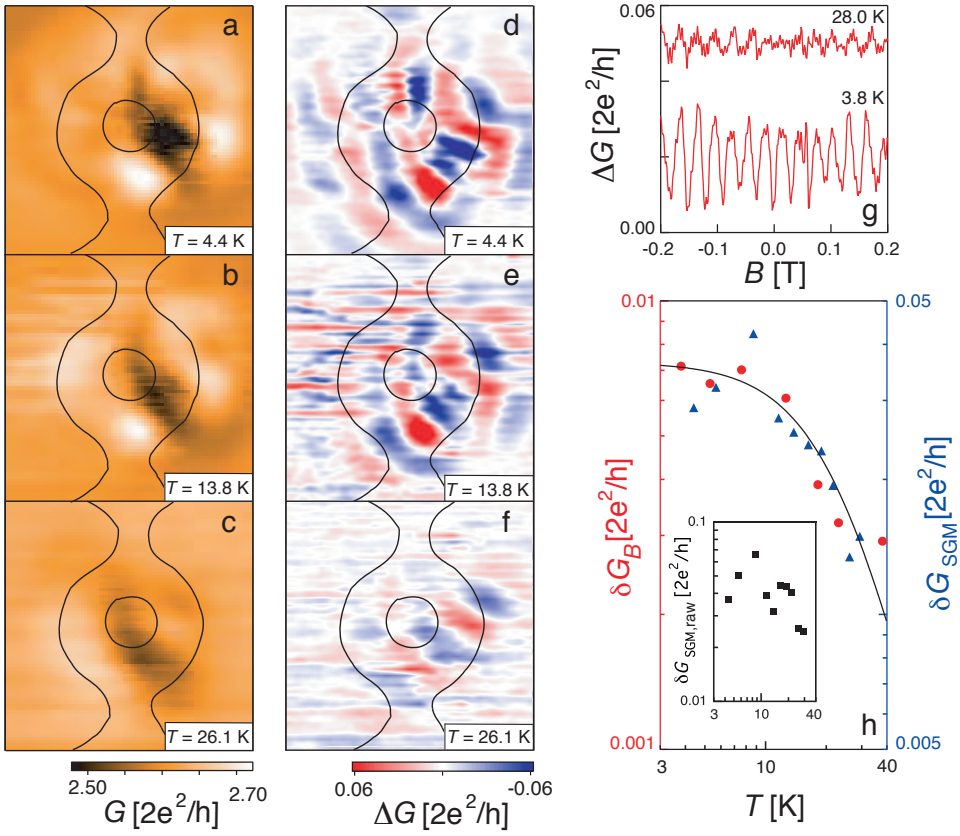

Figure 4.11: Comparison between the temperature dependence of the non-filtered SGM maps (a-c), filtered SG maps (d-f) and AB interference fringes (g). (g) is ΔG vs B at 3.8 K and 28.0 K in R2. (d-f) are $\Delta G(x, y)$ filtered maps of raw maps in (a-c), respectively, measured on sample R2 at $V_{\text{tip}} = 0$V, $D_{\text{tip}} = 50$ nm, $B = 0$ T and $T = 4.4$, 13.8 and 26.1 K, respectively. (h) Red circles: standard deviation of the magneto-conductance curves δG_B vs T (left axis); blue triangles : standard deviation over the ring region of filtered SGM images δG_{SGM} vs T (right axis). The black line is a guide to the eye. The inset shows the standard deviation over the ring region of original SGM maps $\delta G_{\text{SGM raw}}$ vs T.

Another aspect of filtering the experimental images is to avoid artifacts created by the borders of the image. In order to avoid these effects before filtering the raw image, the raw image is extended by 256 points per axe. This extension is done by taking the value of the last point of each line of the image. After applying the filter to the FFT of the raw data we perform the inverse FFT and, at the end, we zoom up the center of the image (128 per 128 points).

An additional argument for filtering the images is shown in Fig. 4.11. Fig. 4.11 (d-f) show high-pass filtered ΔG maps of Fig. 4.11 (a-c), respectively, measured on R2 between $T = 4.4$ and 26.1 K.

In Fig. 4.11(d-f), we note a decay of the ΔG fringe amplitude with increasing T, but the fringes pattern remains essentially unchanged. We define δG_{SGM}, the standard deviations of the filtered conductance maps, calculated on a 400 nm diameter circle centered on the QR, and δG_B, the standard deviation of AB oscillations in G vs B. We can compare the T-dependences of SGM images and AB effect (Fig. 4.11(h)). δG_B and δG_{SGM} clearly follow the same T-dependence: a strong decay above $T \sim 10$ K, and a saturation at lower T, consistent with the intrinsic saturation of τ_ϕ previously reported in similar confined systems [24]. This suggests that the of the AB effect and the central pattern of fringes in ΔG maps are intimately related and find a common origin in electron wavefunction interferences. This will be further discussed later on.

Here, we want to stress that similar examination was performed with the raw data. In the inset of Fig. 4.11(h) we show the evolution of amplitude of the fringes from the raw data $\delta G_{\mathrm{SGM\ raw}}$ with temperature. In contrast with the filtered images, this curve follows a very distinct temperature evolution from δG_B and δG_{SGM} indicating that the background does not share the same coherent origin. Therefore, the filtering technique is very powerful in extracting coherent effects from raw data.

In the remaining of this chapter, we focus on high-pass filtered images, and try to uncover the origin of the oscillations visible in the data.

4.5.2 Fringes analysis

In Fig. 4.12 (a-c) we show a sequence of SGM conductance maps for a tip-surface distance D_{tip} of 50 nm, 70 nm and 90 nm. In this sequence we observe that the amplitude of the fringes decreases as D_{tip} increases. Nevertheless, the fringes are maintained in all the three images. This effect can be better observed in Fig. 4.12 (d-e). In Fig. 4.12 (d) we plot the circular profile under the ring region of images shown in Fig.

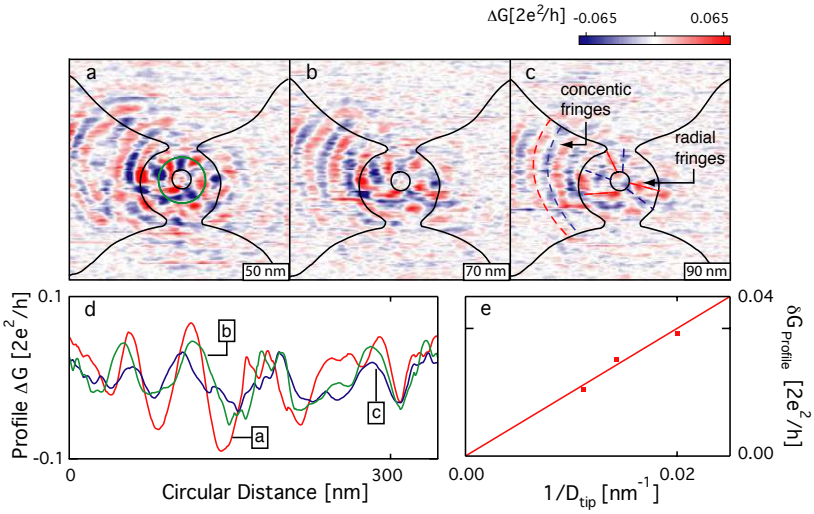

Figure 4.12: (a-c) sequence of SGM conductance map for a tip-surface distance D_{tip} of 50 nm, 70 nm and 90 nm. (d) profiles of images (a-c) over a circle inside the ring region. In (e) $\delta G_{\text{Profile}}$ denotes the standard deviation of each profile vs D_{tip}. The line correspond to a distance dependence of $1/D_{\text{tip}}$. In this set of images we used $V_{\text{tip}} = 0.3\ V$ and $B = 1\ T$

4.12 (a-c). Afterwards, the standard deviation is calculated for each circular profile and plotted versus D_{tip} in Fig. 4.12 (e). This result demonstrates the stability of the SGM images over a QR, *i.e.* there is no sign of chaotic behaviour. Furthermore, the typical spatial periodicity of the oscillations ($\sim$ 100 nm) is much larger than the electron Fermi wavelength in our sample (λ_F $\sim$18 nm). These two evidences are in contrast with previous experimental studies of Crook *et. al.*, shown in section 3.3, and tells us immediately that the 'standing electron wave' pattern observed is not the relevant mechanism to explain our observations.

As shown in Fig. 4.12 (c) the fringe pattern depends on the scanned region. While fringes are predominantly radial when the tip is located directly above the ring, i.e. δG fringes emerge from the centre of the QR towards its perimeter, they become concentric when the tip moves away from the QR with a larger amplitude on the left side of the QR. It is worth mentioning that this left-right imbalance is observed whatever the direction of the magnetic field or the probe current. Therefore, it is related to an asymmetry of the QR or tip shape, and is not a signature of the Lorentz force which could also lead to an imbalance of

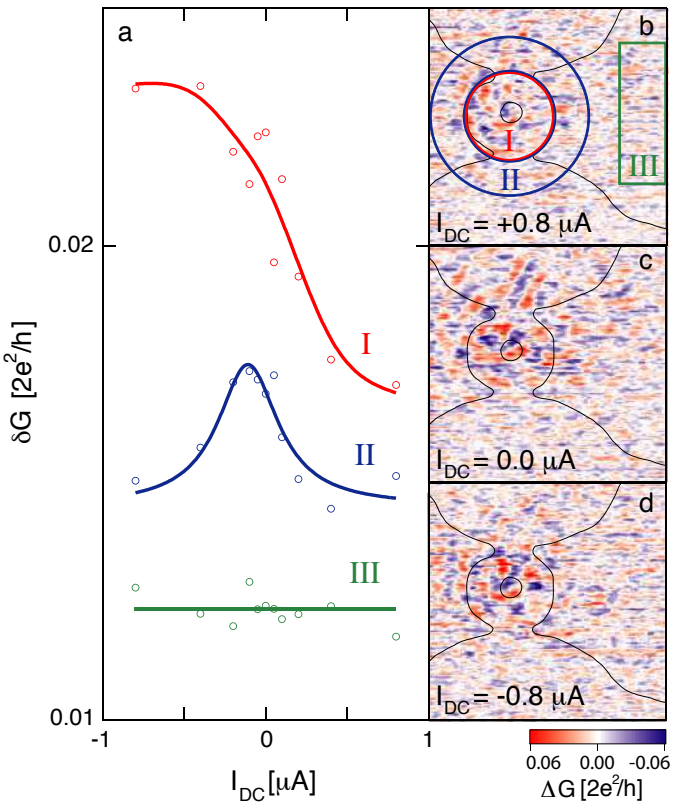

Figure 4.13: Evidence for a different behaviour of the standard deviation of radial and concentric fringes. (a) δG (standard deviation of ΔG) as a function of the probe current I_{DC}, calculated in different areas (I-III) of the filtered conductance maps, indicated in (b). (b-c) filtered conductance maps recorded at B=5.95 T, for different probe currents : +0.8 μA (b), 0.0 μA (c) and -0.8 μA (d).

the electron injection in the two arms of the QR.

Fig. 4.13 shines light on a difference behaviour between radial and concentric fringes. In this figure, we study the effect of the probe current I_{DC}, a DC current passing through the QR, applied in addition to the AC current used to perform the conductance measurement. Increasing the absolute value of I_{DC} is equivalent to raising the electron excess energy relative to the Fermi energy. Fig. 4.13 (c) is the conductance map recorded at I_{DC}= 0 μA, while Fig. 4.13 (b) and (d) were recorded, respectively, for a large positive (+0.8 μA) and negative (-0.8 μA) probe current, bringing the electron system out of thermal equilibrium by more than 1 meV. The data can be better understood if

one divides the scan in three regions : the area enclosed in the QR where radial features are predominant (I), the ring-shaped area in the vicinity of the QR where concentric fringes dominate (II) and finally an area situated far from the QR where the influence of the tip vanishes (III). We first note that concentric fringes (region II) are strongly reduced at large bias disrespect of its sign. Region I, on the other hand, exhibits a very different behaviour depending on current direction: while radial fringes die out at large positive bias, they are strengthened and rearranged when bias is reversed. A more quantitative picture of these differences is presented in Fig. 4.13 (a), showing the evolution of δG, the standard deviation of δG, calculated over regions I-III, as a function of I_{DC}. As region III exhibits no dependence on I_{DC}, it serves as a reference for the noise level. Region II shows a decrease of δG at large bias, which is symmetric in I_{DC}. Since coherent effects are extremely sensitive to electron excess energy, which enhances the electron-electron scattering rates[82], this observation points towards a coherent origin for the concentric fringes. By contrast, δG in region I shifts gradually from one level to another as current is reversed.

For the time being, this asymmetric behaviour is not completely understood. We should, nevertheless, point out two aspects. Firstly, this different behaviour indicates that there exist two perturbation regimes in which the QR can be brought while being scanned by the tip.

Secondly, this set of images was obtained at 5.95 T. This constitutes the maximum magnetic field strength used in these experiments. Furthermore, the presence of Shubnikov-de Haas oscillations (see section 3.4.1) shows that at this high magnetic field the cyclotron radius is smaller than the dimensions of the ring and therefore the conduction of the electrons through the ring is done, in part, by edge states.

In order to support better this argumentation, that radial and concentric fringes do not share the same origin, we do an analogous analysis using a further parameter: the tip-2DEG bias (V_{tip}). In Fig. 4.14 we compare the evolution of the fringes amplitude in the different regions of the SGM images. Fig.4.14 (a) is a SGM image obtained for $V_{tip} = 2$ V. As done previously, we distinguish three regions on the SGM scans: region I is the area of the QR; region II corresponds to the vicinity of the QR where concentric fringes are observed; region III is situated in an area where the influence of the tip vanishes and is used as reference. A quantitative comparison of the fringes behaviour is shown in Fig. 4.14 (b) where we plot the standard deviation of the conductance (δG_{SGM}) in each region as a function of V_{tip}. The fringes amplitude in region I exhibits a fast quasi-linear increase with V_{tip}, while the fringes amplitude in region II remains essentially constant.

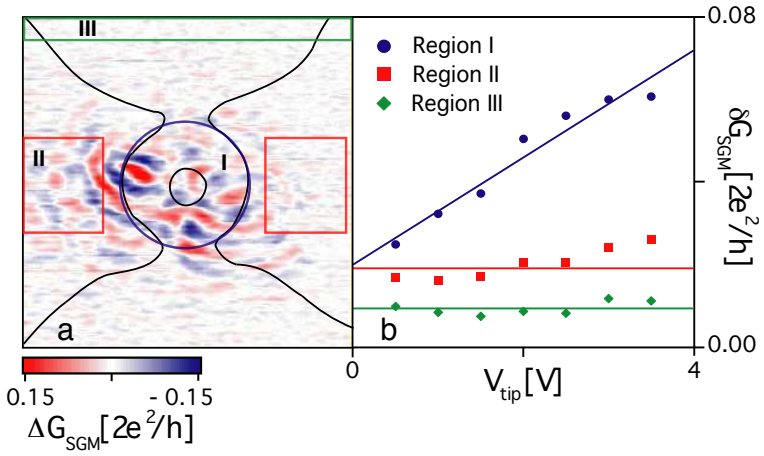

Figure 4.14: (a) Filtered SGM image of the conductance variations recorded for $V_{tip} = 2.5$ V, $D_{\text{tip}} = 50$ nm, $T = 4.2$ K, $B = 2$ T. (b) Standard deviation of the conductance in different regions versus tip bias. Region I corresponds to the ring area. Region II corresponds to the fringes on both sides of the ring. Region III is taken as reference.

4.5.3 Electrical AB effect in the SGM images

In this section we clarify the origin of the outside concentric fringes. For this purpose we sweep the magnetic field in order to tune the phase of interfering electrons.

Fig. 4.15 (a-c) show conductance maps measured at B = 1.5 T, 1.513 T and 1.526 T, covering a complete Aharonov-Bohm cycle, i.e. the magnetic flux enclosed in the area of the QR changes by one flux quantum. Qualitatively, the pattern of concentric and radial oscillations is surprisingly similar on this set of images. This apparent weak sensitivity to magnetic field strongly contrasts with the results of experiments performed on large open quantum dots on the experiments of Crook *et. al.*. This is a sign of the regular behaviour of the electron motion in QR, in opposition to the chaotic behaviour characterising large open quantum dots. In quantum rings, the magnetic field acts in a more subtle way. This sequence of images reveal a continuous movement of fringes upon varying B. A quantitative analysis of the concentric fringes evolution is obtained by computing the average of the horizontal conductance profiles situated in regions α and β on Fig. 4.15 (a) (delimited by the dashed lines). Fig. 4.15 (d-e) show the evolution of these profiles over an Aharonov-Bohm cycle. On the left of the QR (region α), the oscillation pattern smoothly moves leftwards

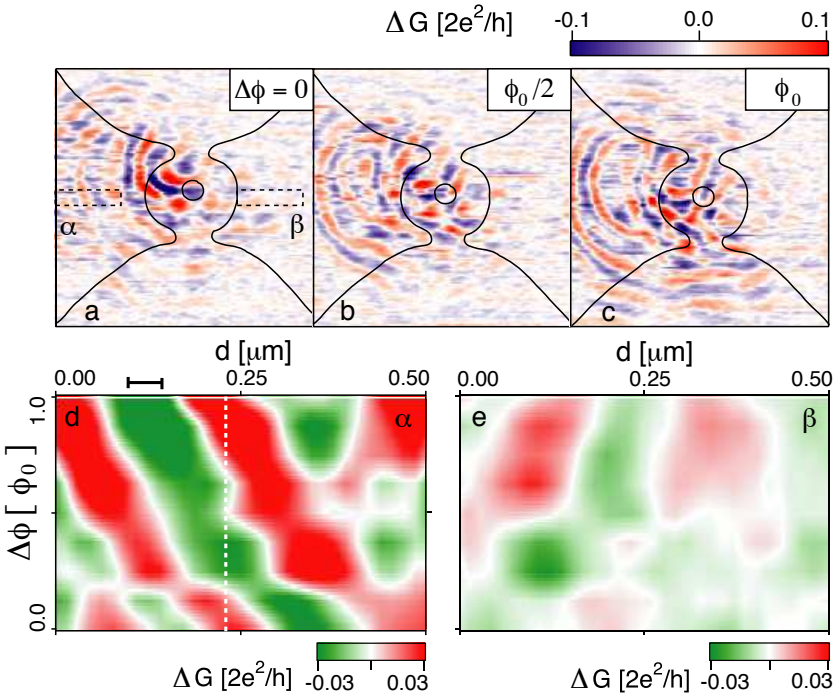

Figure 4.15: Evolution of filtered conductance maps along an AB cycle. (a-c) filtered conductance maps recorded at increasing magnetic fields between B=1.5 T and 1.526 T (over one AB cycle), showing a continuous and mostly periodic evolution of the pattern of fringes. In the vicinity of the ring, the fringe pattern undergoes a cyclic evolution over the sequence: starting at the position of a conductance maximum at the beginning of the cycle, one observes a minimum at the middle of the cycle, and a conductance maximum again at the end of the cycle. (d-e) average of horizontal conductance profiles in region α and β (on both sides of the QR, defined by the dashed rectangles on (a)), plotted as a function of the phase difference $\Delta\phi$, in units of the Aharonov-Bohm period ϕ_0. The evolutions of the patterns are opposite in the two regions (leftwards on (d), and rightwards on (e)), indicating that the cyclic evolution of the fringes is not a measurement artefact due to a movement of the QR during the measurement (the maximum value of this movement corresponds to the error bar above (d)).

by one period as the Aharonov-Bohm phase - ϕ - changes by one flux quantum : ϕ_0. Symmetrically, on the right of the QR (region β) the oscillation pattern moves rightwards by one period as ϕ moves from 0 to ϕ_0 (see dashed line on Fig. 4.15 (e)). We interpret this behaviour as a scanning-gate induced electrostatic Aharonov-Bohm effect. Indeed, as the tip approaches the QR, either from left or right, the electrical potential mainly raises on the corresponding side of the QR. This induces a phase difference between electron wavefunctions travelling through both arms of the ring, which causes the observed oscillations. Since the magnetic field applies an additional phase shift to electron wavefunctions, the V-shaped pattern on Fig. 4.15 (d-e) corresponds to iso-phase lines for the electrons. This observation ensures that our data are directly related to the Aharonov-Bohm effect (and not to a displacement of the QR during the AB cycle) and that concentric fringes originate from an interference effect of coherent electrons. We finally note that the observed oscillations are reminescent of those reported in QRs with biased side gates [8][**?**]. However, our experiment brings direct spatial information on interference effects, as we take advantage of the possibility to scan a much more localized tip-induced perturbation across the sample.

Similar behaviour can be observed without applying a magnetic field. In the previous section we compared the amplitude variation with V_{tip}. Here we complement this observation. A closer inspection of these images shows that the tip bias also affects the position of the outside fringes. When V_{tip} is raised, the outside concentric fringes are shifted away from the ring region. This effect is clearly evidenced in Fig.4.16(d) and (e) where we plot the sequence of averaged profiles versus V_{tip} for two regions (α and β) on both sides of the QR. These regions were chosen for their fringes visibility. We interpret this behaviour as the result of an electric field induced phase shift of the electron wave functions. This phase shift changes the interference condition between the electrons flowing in the two different arms of the ring, and thus the transmission through the device.

The expansion of the outside fringes, combined with the insensitivity of their amplitude to the tip bias, are a clear indication that they originate from a pure interference phenomenon. Therefore, in this regime, we can directly compare the phase shifts induced by the tip electric field and by the external magnetic field. In our experiment a phase shift of π is obtained for a tip bias variation (ΔV_{tip}) of 1.75 V, while using the magnetic field the same value is obtained with 13 mT.

Comparing both experiments we can estimate the lever arm of the gating effect, *i.e.* the ratio between the electron gas potential and the

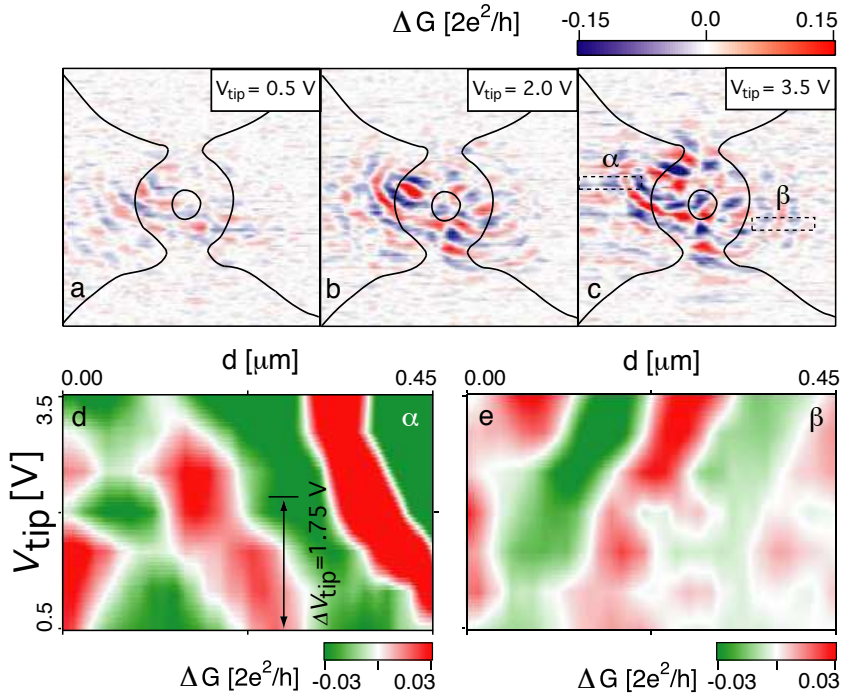

Figure 4.16: Evolution of filtered conductance maps for different V_{tip}. (a-c) SGM images for tip bias of 0.5 V, 2 V,and 3.5 V, respectively. (d-e) Sequence of profile plots versus tip bias. Each horizontal line corresponds to a vertical average of the conductance map in region α (d) and β (e), drawn on Fig. 3(c). The translation of the fringes to the left in (d) and to the right in (e) is due to a pure electric Aharonov-Bohm effect.

applied tip voltage. In a simple model where a potential difference ΔV_{gas} is applied between the two arms of the QR of length L, using Eq. 4.3 the phase shift $\Delta\Phi$ of the electron wave functions writes:

$$\Delta\Phi = \pi \frac{e\,\Delta V_{gas}}{E_F} \frac{L}{\lambda_F} \tag{4.4}$$

Using $E_F = 100\,\text{meV}$, $\lambda_F = 20\,\text{nm}$, and $L = 600\,\text{nm}$, which we believe to be close to experimental conditions, we obtain $\Delta V_{gas} = 3.3\,\text{mV}$ for a phase shift of π, and therefore a lever arm ($\Delta V_{gas}/\Delta V_{tip}$) of about 0.002. This low value reflects a large electrostatic screening, due to the large electron density in the 2DEG.

4.5.4 Imaging electronic wave function

To investigate it further on the SGM imaging mechanism, we compare experimental images with simulations. These simulations were performed by Marco Pala in the scope of these experiments.

Indeed, the origin of the radial fringes observed within the QR area can be better understood by means of quantum mechanical simulations of the electron probability density at the Fermi energy in our QR [83]. Fig. 4.17 shows typical patterns of electron probability density $|\psi^2|$ obtained by summing the patterns obtained for each populated quantum channel. While the precise position and number of fringes is sensitive to the Fermi energy, simulations typically reveal radial fringes emerging from the centre of the QR. Since the scattering probability of ballistic electrons is proportional to the density probability, the conductance of the QR should be mostly affected when the tip is located above a region where $|\psi^2|$ is at maximum, and hence show radial fringes. The typical conductance map shown in Fig. 4.18 is consistent with this picture: not only are there radial fringes, but their number and typical lateral length scale are very similar to those in the electron probability density computed for our QR. This similarity, together with the experimental data shown earlier, are clear indications that we are actually locally probing electron flow as the tip of our microscope scans above the quantum ring area.

Simulations

The device conductance and the wave functions at the Fermi energy are calculated in the scattering matrix formalism and using the Landauer-Büttiker formalism, with the same method as in [83]. The ring is subdivided into slices perpendicular to axis x between both openings in the QR. The Schrödinger equation is numerically solved in each slice along y for each 1D channel and the plane wave solutions along x are matched between each slice as prescribed in [84], giving the scattering matrix between two slices. The overall scattering matrix and wave functions are computed by composing the matrices of all slices. The geometry (topology and dimensions) of the ring in the simulation is comparable to that of our real sample, taking the depletion length at device edges into account ($\sim$35 nm), *i.e.* the inner and outer radii of the ring are 140 nm and 265 nm, respectively, and the width of the openings is 120 nm. The electron Fermi energy is adjusted close to the value extracted from the 2DEG measurements, and the number of quantum modes contributing to the QR conductance is chosen such that the calculated conductance through the QR closely matches the

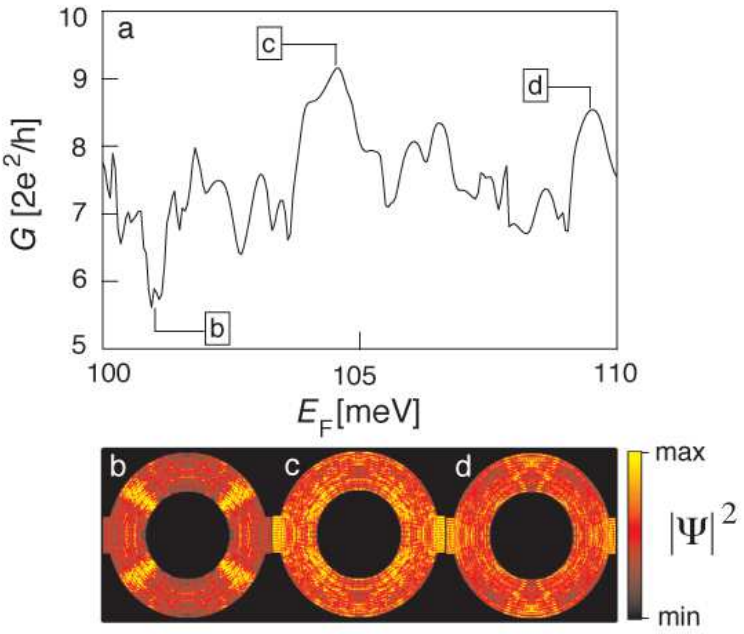

Figure 4.17: (a) Calculated conductance G vs Fermi energy E_{F} in a QR with inner and outer radii of 140 and 265 nm. (b-d) Electron probability density $\Psi^2(x, y, E_{\mathrm{F}})$ in a QR at $E_{\mathrm{F}} = 104.6$, 109.5 and 101 meV, respectively.

experimental value.

When E_{F} is varied, the configuration of resonant states within the QR and their coupling to the reservoirs change [74]. As a consequence, the calculated conductance G exhibits fluctuations as a function of E_{F}, one of the hallmarks of transport in open mesoscopic systems. This is illustrated in Fig. 4.17(a), showing the calculated G as a function of E_{F} around the measured $E_{\mathrm{F}}^{\mathrm{2DEG}}$ value in the unpatterned heterostructure. Figs. 4.17(b-d) show typical patterns of $|\Psi|^2(x, y, E_{\mathrm{F}})$ in our QR, for $E_{\mathrm{F}} = 101.0$, 109.5 and 104.9 meV, respectively. Small-scale concentric oscillations are visible within the whole QR area in Figs. 4.17(b-d), whose characteristic spatial periodicity is related to the Fermi wavelength λ_{F}. On a scale larger than λ_{F}, $|\Psi|^2(x, y, E_{\mathrm{F}})$ is rather homogeneous in Figs. 4.17(c-d), while it exhibits four strong radial fringes in Figs. 4.17(b).

In analogy with the experiment, we have included in the simulation a moving perturbation potential mimicking the tip effect, and then calculated the conductance of the QR for each position of the perturbation. Fig. 4.18(c) shows such a simulated conductance map $G(x, y)$, obtained for $E_{\mathrm{F}} = 101$ meV, using the Gaussian potential $V(x, y)$ as

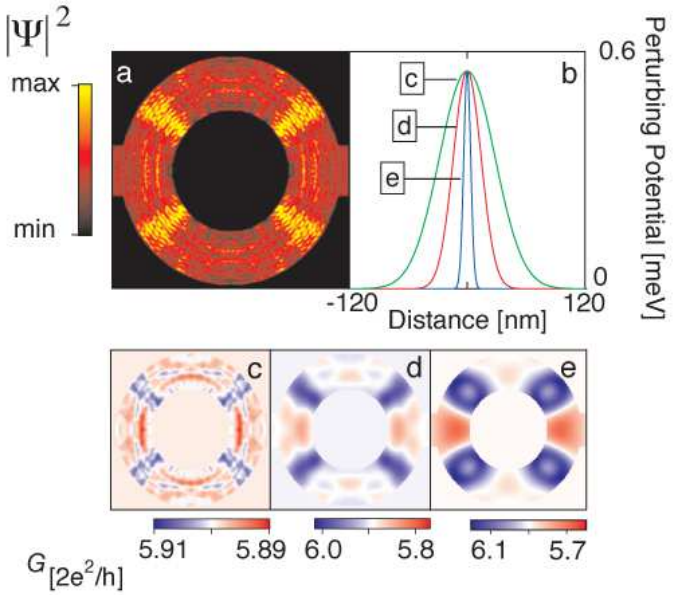

Figure 4.18: (c-e) Simulated conductance maps $G(x, y)$ for an electron probability density with a Fermi energy of $E_F = 101$ meV (a). The gaussian perturbing potential used to build each image is shown in (b). (c-e) are obtain for $V_m = E_F/200$ and $\sigma = 5$, 20 and 40 nm, respectively.

the moving perturbation,

$$V(x, y) = V_m \times \exp\left\{-\left[\frac{(x - x_0)^2 + (y - y_0)^2}{2\sigma^2}\right]\right\} \tag{4.5}$$

with $V_m = E_F/200$, $\sigma = 5$ nm and (x_0, y_0) the local position of the tip. Most importantly, a careful examination of Fig. 4.18(d-e) reveals that all the features visible in the simulated $|\Psi|^2(x, y, E_F)$ are also visible in the calculated G map. This striking correspondence reveals that SGM can in principle be used to map the unperturbed electron probability density.

Enlarging now the width of the perturbing potential causes the smallest SGM features to disappear . As σ overcomes λ_F, concentric fringes completely vanish. Nevertheless, at the scale of the radial fringes, the correspondence between $G(x, y)$ and $|\Psi|^2(x, y, E_F)$ is maintained (Fig. 4.18(d)) although the aspect of the four radial fringes changes (Fig. 4.18(e)). Most importantly, the size of the smallest features in the simulated G maps is roughly correlated to σ. Based on Figs. 4.18 (c-e), this allows us to infer a lower bound for $\sigma \sim$ 20-30 nm.

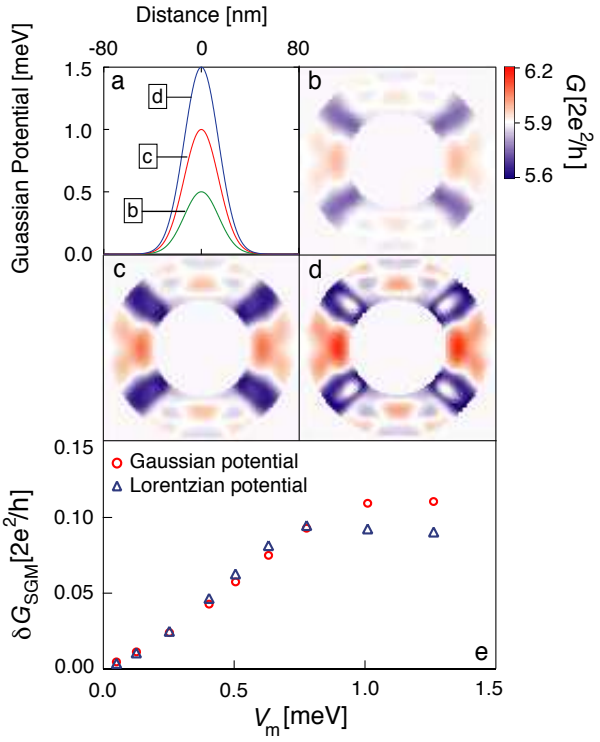

Figure 4.19: (a) Gaussian perturbing potential used to build simulated G maps (c-e), *i.e.* calculated for E_{F}= 101 meV, σ = 20 nm and V_{m} = 0.5, 1.0 and 1.5 meV, respectively. (e) Fringe amplitude δG_{SGM} on simulated G maps as a function of the maximum of gaussian potential (with $\sigma = 20$ nm) and as a function of the maximum of Lorentzian potential.

To come closer to a complete description of our experiments, we now examine the effect of the perturbation amplitude. As V_{m} is increased, keeping $\sigma = 20$ nm, we observe that the SGM fingerprint remains qualitatively independent of V_{m}, and that its amplitude increases linearly with V_{m} [Figs. 4.19(a-c)]; a behaviour consistent with the observations related in Fig. 4.14. Above $V_{\mathrm{m}} \sim 0.8$ meV, qualitative changes in the SGM pattern appear together with a deviation from the linear evolution of δG_{SGM} vs V_{m} [Fig. 4.19(c)], a value for which differences between $G(x, y)$ and $|\Psi|^2(x, y, E_{\mathrm{F}})$ start to emerge. Fig. 4.19(e) also shows that the evolution of δG_{SGM} vs V_{m} is weakly affected by the exact shape of the perturbation, *e.g.* Lorentzian or Gaussian.

The consistency between the simulated behaviour of δG_{SGM} vs V_{m} and the experimental data in Fig. 4.14 leads us to conclude that, at low V_{tip} (below $\sim$ 2 V), the central part of our SGM maps directly reveals

the main structure of $|\Psi|^2(x, y, E_{\mathrm{F}})$ in our quantum rings.

This means that we can attribute the pattern of conductance fringes in Fig. 4.14(a-c) and Fig. 4.19(c-d) to wavefunctions.

Chapter 5

Conclusion

In this thesis three aspects have taken our attention. The first concerns the the AFM instrumentation. We have implemented a system adapted to study electric properties of semiconductor structures. To do so, we have chosen to work at 4 K and to have the possibility of working under a magnetic field.

Working at low temperatures bring two advantages. The first one concerns the resolution and stability of the instrument. The thermal noise is decreased by a factor of $\sqrt{300/4} \simeq 8.7$, which implies a gain in force sensitivity and electrical charge detection sensitivity. Furthermore, working inside a cryostat, where the temperature gradients are very small, limits the mechanical drift of piezoelectric elements. The second reason is, indeed, mandatory. The coherent effects studied in the Chapter 3 can only be observed at these low temperatures.

The second aspect studied in this thesis is related to charge detection. In Chapter 2, we presented a method to take advantage of a parametric effect to measure electrical excess charges over a surface. We have studied two particular situations. When the electric excitation is driven close to twice the natural frequency ($\omega_{el} = 2\omega_0 + \Delta\omega$) and at $\omega_{el} = \omega_0 + \Delta\omega$. We have shown that in both cases a parametric effect is present. It results from the fact that an alternative electrostatic force (ω) has, intrinsically, a component at 2ω. In this chapter we presented an analytical model to show the presence of this effect. The model was verified by numerical solutions and experiments. This analytical approach is particularly useful to derive the best measurement conditions.

However, these techniques have not been implemented yet. Concerning the two approaches, the method $\omega_{el} = 2\omega_0 + \Delta\omega$ seems to have two significant advantages. Firstly, as shown in the same chapter, it can beat the thermal noise limit. Secondly, in this situation the parametric

effect intervenes in the form of a gain what may simplify the operation of setting the system in the maximal sensitivity and the subsequent interpretation of the experimental data.

This study made us conclude that, in contrast to a widespread belief, the ω component of the cantilever oscillation is not at all independent of the 2ω component of the electric force. This remark is particularly relevant in the case of $\omega_{el} = \omega_0 + \Delta\omega$ which is largely known in literature (KFM). We conclude that parametric effect prevails and determines the oscillation amplitude whenever the tip gets close to the sample.

In the last chapter we have addressed the electronic transport in a model sample, the quantum ring. The most significant contribution concerns the demonstration of the ability of mapping the electron wave function inside a buried 2DEG. This constitute the most relevant result of this thesis. We show that SGM may be seen as the analog of STM for imaging the electronic the local density of states (LDOS) in open mesoscopic systems buried under an insulating layer, or the counterpart of the near-field scanning optical microscope that images the photonic LDOS in confined nanostructures [85].

In our experimental conductance maps of the QR we observed reproducible structures. Using quantum mechanical simulations of the electron probability density, including the perturbing potential of the tip, we could reproduce the main experimental features and demonstrate the relationship between conductance maps and electron probability density maps.

Furthermore, this experiment clearly shows the capability of SGM to image and to control electrons buried under a surface: in such an experimental setup, the electron phase can be tuned using a flying gate. This kind of instrument can therefore be used to modify *in situ* the properties of coherent electronic devices.

We believe that, with this experiment, we showed that the combination of AFM with transport measurements is very powerful for investigating electron interferences in real space at the local scale inside buried mesoscopic devices. One can envision to use the technique to test electronic devices based on real-space manipulation of electron interferences, such as the electronic analogs of optical or plasmonic components (resonators, Y-splitters, ...). *In situ* control over the electron potential would provide a mean to design new ballistic devices with desired characteristics (beam splitters, multiterminal devices...). Additionally, taking advantage of the controllable spin-orbit coupling effects in InGaAs structures or other materials (InSb, magnetic semiconductors, ...), the technique may also serve to image the spin dynamics of

carriers within low-dimensional structures. Therefore, our study not only provides a distinctive real-space visualization of the particle-wave duality of electrons, but also paves the way for a wealth of experiments probing the local behaviour of charge carriers inside a large variety of open mesoscopic systems.

Nevertheless these themes are far from being exhausted. In this thesis we only hope to have made a small contribution to this wide research field.

Bibliography

[1] T. Melin, H. Diesinger, D. Deresmes, and D. Stievenard. Probing nanoscale dipole-dipole interactions by electric force microscopy. *Phys. Rev. Lett.*, 92(16):166101, 2004.

[2] L. J. Klein and C. C. Williams. Single electron tunneling detected by electrostatic force. *Appl. Phys. Lett.*, 79(12):1828–1830, September 2001.

[3] M. Vogel, B. Stein, H. Pettersson, and K. Karrai. Low-temperature scanning probe microscopy of surface and subsurface charges. *Appl. Phys. Lett.*, 78(17):2592–2594, 2001.

[4] http://www.attocube.com/ Nov, 2007.

[5] Juan R. Sanmartin. O botafumeiro: Parametric pumping in the middle ages. *Am. J. of Phys.*, 52(10):937–945, 1984.

[6] F. Hai A. Y. Wong, M. V. Goldman and R. Rowberg. Parametric excitation from thermal fluctuation at plasma-drift wave frequencies. *Phys. Rev. Lett.*, 21(8):518–522, Aug 1968.

[7] R. A. Webb, S. Washburn, C. P. Umbach, and R. B. Laibowitz. Observation of $\frac{h}{e}$ Aharonov-Bohm Oscillations in Normal-Metal Rings. *Phys. Rev. Lett.*, 54(25):2696–2699, Jun 1985.

[8] S. Washburn, H. Schmid, D. Kern, and R. A. Webb. Normal-metal Aharonov-Bohm effect in the presence of a transverse electric field. *Phys. Rev. Lett.*, 59(16):1791–1794, Oct 1987.

[9] R. A. Webb Boris L. Altshuler, P. A. Lee. *Mesoscopic Phenomena in Solids*. North-Holland, 1991.

[10] L. Eaves F. W. Sheard N. Miura P. B. Wilkinson, T. M. Fromhold and T. Takamasu. Observation of 'scarred' wavefunctions in a quantum well with chaotic electron dynamics. *Nature*, 380(6575):608–610, 1996.

[11] M. Freitag, A. T. Johnson, S. V. Kalinin, and D. A. Bonnell. Role of single defects in electronic transport through carbon nanotube field-effect transistors. *Phys. Rev. Lett.*, 89(21):216801, Nov 2002.

[12] Franz J. Giessibl. Advances in atomic force microscopy. *Rev. Mod. Phys.*, 75(3):949–983, Jul 2003.

[13] R. Dianoux, H. J. H. Smilde, F. Marchi, N. Buffet, P. Mur, F. Comin, and J. Chevrier. Kinetic roughening of charge spreading in a two-dimensional silicon nanocrystal network detected by electrostatic force microscopy. *Phys. Rev. B*, 71(12):125303–7, 2005.

[14] R. Stomp, Y. Miyahara, S. Schaer, Q. Sun, H. Guo, P. Grutter, S. Studenikin, P. Poole, and A. Sachrajda. Detection of single-electron charging in an individual inas quantum dot by noncontact atomic-force microscopy. *Phys. Rev. Lett.*, 94(5):056802–4, 2005.

[15] A. E. Gildemeister, T. Ihn, M. Sigrist, K. Ensslin, D. C. Driscoll, and A. C. Gossard. Measurement of the tip-induced potential in scanning gate experiments. *Phys. Rev. B*, 75(19):195338–7, 2007.

[16] T. Vancura, S. Kicin, T. Ihn, K. Ensslin, M. Bichler, and W. Wegscheider. Kelvin probe spectroscopy of a two-dimensional electron gas below 300 mk. *Appl. Phys. Lett.*, 83(13):2602–2604, 2003.

[17] T. D. Krauss and L. E. Brus. Charge, polarizability, and photoionization of single semiconductor nanocrystals. *Phys. Rev. Lett.*, 83(23):4840–4843, Dec 1999.

[18] J. Rychen, T. Ihn, P. Studerus, A. Herrmann, and K. Ensslin. A low-temperature dynamic mode scanning force microscope operating in high magnetic fields. *Rev.of Sci. Inst.*, 70(6):2765–2768, 1999.

[19] G. Binnig, H. Rohrer, Ch. Gerber, and E. Weibel. Surface studies by scanning tunneling microscopy. *Phys. Rev. Lett.*, 49(1):57–61, Jul 1982.

[20] http://nobelprize.org/ Nov, 2007.

[21] G. Binnig, C. F. Quate, and Ch. Gerber. Atomic force microscope. *Phys. Rev. Lett.*, 56(9):930–933, Mar 1986.

[22] R. Dianoux, F. Martins, F. Marchi, C. Alandi, F. Comin, and J. Chevrier. Detection of electrostatic forces with an atomic force

microscope: Analytical and experimental dynamic force curves in the nonlinear regime. *Phys. Rev. B*, 68(4):045403, Jul 2003.

[23] Y. Martin, C. C. Williams, and H. K. Wickramasinghe. Atomic force microscope–force mapping and profiling on a sub 100-[A-ring] scale. *J. of Appl. Phys.*, 61(10):4723–4729, 1987.

[24] G. Ten Brinke V. Koutsos, E. Manias and G. Hadziioannou. Atomic force microscopy and real atomic resolution. simple computer simulations. *Europhys. Lett.*, 26(2):103–107, 1994.

[25] F. Ohnesorge and G. Binnig. True Atomic Resolution by Atomic Force Microscopy Through Repulsive and Attractive Forces. *Science*, 260(5113):1451–1456, 1993.

[26] C. Schonenberger and S. F. Alvarado. A differential interferometer for force microscopy. *Rev.of Sci. Inst.*, 60(10):3131–3134, 1989.

[27] T. J. Tayag, E. S. Kolesar, B. D. Pitt, K. See Hoon, J. Marchetti, and I. H. Jafri. Optical fiber interferometer for measuring the in situ deflection characteristics of microelectromechanical structures. *Optical Eng.*, 42(1):105–111, 2003.

[28] C. Meyer, O. Sqalli, H. Lorenz, and K. Karrai. Slip-stick step-scanner for scanning probe microscopy. *Rev.of Sci. Inst.*, 76(6):063706, 2005.

[29] http://www.nanotec.es/ Nov, 2007.

[30] B. Turner K. Napoli, M. B. Mathematical modeling, experimental validation and observer design for a capacitively actuated microcantilever. *Proc. of the Am. Cont. Conf.*, 5:3732, Jun 2003.

[31] E. I. Butikov. Parametric excitation of a linear oscillator. *Eur. J. of Phys.*, 25(4):535–554, 2004.

[32] D. Rugar and P. Grütter. Mechanical parametric amplification and thermo-mechanical noise squeezing. *Phys. Rev. Lett.*, 67(6):699–702, Aug 1991.

[33] T. Ouisse, M. Stark, F. Rodrigues-Martins, B. Bercu, S. Huant, and J. Chevrier. Theory of electric force microscopy in the parametric amplification regime. *Phys. Rev. B*, 71(20):205404, 2005.

[34] T. Ouisse, F. Martins, M. Stark, S. Huant, and J. Chevrier. Signal amplitude and sensitivity of the Kelvin probe force microscopy. *Appl. Phys. Lett.*, 88(4):043102, 2006.

[35] K. L. McCormick, M. T. Woodside, M. Huang, M. Wu, P. L. McEuen, C. Duruoz, and J. S. Harris. Scanned potential microscopy of edge and bulk currents in the quantum Hall regime. *Phys. Rev. B*, 59(7):4654–4657, Feb 1999.

[36] B. D. Terris, J. E. Stern, D. Rugar, and H. J. Mamin. Contact electrification using force microscopy. *Phys. Rev. Lett.*, 63(24):2669–2672, Dec 1989.

[37] M. A. Salem, H. Mizuta, and S. Oda. Probing electron charging in nanocrystalline Si dots using Kelvin probe force microscopy. *Applied Physics Letters*, 85(15):3262–3264, 2004.

[38] D. M. Schaadt, E. T. Yu, S. Sankar, and A. E. Berkowitz. Charge storage in Co nanoclusters embedded in SiO_2 by scanning force microscopy. *Appl. Phys. Lett.*, 74(3):472–474, 1999.

[39] T. Melin, D. Deresmes, and D. Stievenard. Charge injection in individual silicon nanoparticles deposited on a conductive substrate. *Appl. Phys. Lett.*, 81(26):5054–5056, 2002.

[40] M. A. Eriksson, R. G. Beck, M. Topinka, J. A. Katine, R. M. Westervelt, K. L. Campman, and A. C. Gossard. Cryogenic scanning probe characterization of semiconductor nanostructures. *Appl. Phys. Lett.*, 69(5):671–673, 1996.

[41] M. T. Woodside and P. L. McEuen. Scanned probe imaging of single-electron charge states in nanotube quantum dots. *Science*, 296(5570):1098–1101, May 2002.

[42] Y. Martin, D. W. Abraham, and H. K. Wickramasinghe. High-resolution capacitance measurement and potentiometry by force microscopy. *Appl. Phys. Lett.*, 52(13):1103–1105, 1988.

[43] M. Stark, C. Moller, D. J. Muller, and R. Guckenberger. From images to interactions: High-resolution phase imaging in tapping-mode atomic force microscopy. *Biophys. J.*, 80(6):3009–3018, 2001.

[44] C. Vidal P. Bergé, Y. Pomeau. *L'ordre dans le chaos.* Hermann, Oct 1997.

[45] N.W. MacLachlan. *Theory and applications of Mathieu functions.* Oxford University Press, 1951.

[46] U. Rabe, K. Janser, and W. Arnold. Vibrations of free and surface-coupled atomic force microscope cantilevers: Theory and experiment. *Rev.of Sci. Inst.*, 67(9):3281–3293, 1996.

[47] Joseph A. Turner, Sigrun Hirsekorn, Ute Rabe, and Walter Arnold. High-frequency response of atomic-force microscope cantilevers. *J. of Appl. Phys.*, 82(3):966–979, 1997.

[48] R. W. Stark, G. Schitter, M. Stark, R. Guckenberger, and A. Stemmer. State-space model of freely vibrating and surface-coupled cantilever dynamics in atomic force microscopy. *Phys. Rev. B*, 69(8):085412, 2004.

[49] T. Zambelli X. Bouju J. Polesel-Maris, A. Piednoir and S. Gauthier. An experimental investigation of resonance curves on metallic surfaces in dynamic force microscopy: the influence of frozen versus mobile charges. *Nanotechnology*, 15(2):S24–S29, 2004.

[50] A R Lee and T M Kalotas. Solution of the one-dimensional schrödinger equation in an arbitrary periodic potential. *Physica Scripta*, 44(4):313–320, 1991.

[51] S. Hudlet, M. Saint Jean, B. Roulet, J. Berger, and C. Guthmann. Electrostatic forces between metallic tip and semiconductor surfaces. *J. of Appl. Phys.*, 77(7):3308–3314, 1995.

[52] M. Nonnenmacher, M. P. O'Boyle, and H. K. Wickramasinghe. Kelvin probe force microscopy. *Appl. Phys. Lett.*, 58(25):2921–2923, 1991.

[53] H. O. Jacobs, P. Leuchtmann, O. J. Homan, and A. Stemmer. Resolution and contrast in Kelvin probe force microscopy. *J. of Appl. Phys.*, 84(3):1168–1173, 1998.

[54] J. Rammer. Quantum transport theory of electrons in solids: A single-particle approach. *Rev. Mod. Phys.*, 63(4):781–817, Oct 1991.

[55] M. F. Crommie, C. P. Lutz, and D. M. Eigler. Imaging standing waves in a two-dimensional electron gas. *Nature*, 363(6429):524–527, 1993.

[56] M. A. Topinka, B. J. LeRoy, R. M. Westervelt, S. E. J. Shaw, R. Fleischmann, E. J. Heller, K. D. Maranowski, and A. C. Gossard. Coherent branched flow in a two-dimensional electron gas. *Nature*, 410(6825):183–186, 2001.

[57] S. H. Tessmer, P. I. Glicofridis, R. C. Ashoori, L. S. Levitov, and M. R. Melloch. Subsurface charge accumulation imaging of a quantum hall liquid. *Nature*, 392(6671):51–54, Mar 1998.

[58] N. B. Zhitenev, T. A. Fulton, A. Yacoby, H. F. Hess, L. N. Pfeiffer, and K. W. West. Imaging of localized electronic states in the quantum hall regime. *Nature*, 404(6777):473–476, Mar 2000.

[59] A. Bachtold, M. S. Fuhrer, S. Plyasunov, M. Forero, E. H. Anderson, A. Zettl, and P. L. McEuen. Scanned probe microscopy of electronic transport in carbon nanotubes. *Phys. Rev. Lett.*, 84(26):6082–6085, Jun 2000.

[60] R. Akis David K. Ferry Y. Ochiai N. Aoki, C. R. Da Cunha. Scanning gate microscopy investigations on an ingaas quantum point contact. *Applied Physics Letters*, 87(22):223501, 2005.

[61] G. Finkelstein, P. I. Glicofridis, R. C. Ashoori, and M. Shayegan. Topographic mapping of the quantum Hall liquid using a few-electron bubble. *Science*, 289(5476):90–94, Jul 2000.

[62] Z. Barticevic, G. Fuster, and M. Pacheco. Effect of an electric field on the Bohm-Aharonov oscillations in the electronic spectrum of a quantum ring. *Phys. Rev. B*, 65(19):193307, May 2002.

[63] A. Lorke, R. J. Luyken, A. O. Govorov, J. P. Kotthaus, J. M. Garcia, and P. M. Petroff. Spectroscopy of nanoscopic semiconductor rings. *Phys. Rev. Lett.*, 84(10):2223–2226, Mar 2000.

[64] S. Datta. *Electronic Transport in Mesoscopic Systems*. Cambridge University Press, 1995.

[65] Y. Aharonov and D. Bohm. Significance of electromagnetic potentials in the quantum theory. *Phys. Rev.*, 115(3):485–491, Aug 1959.

[66] D.Frustaglia F. Giazotto L. Sorba F. Carillo, G. Biasiol and F. Beltram. $In_0.75Ga_0.25As$ on GaAs submicron rings and their application for coherent nanoelectronic devices. *Physica E*, 32(1-2):53–56, May 2006.

[67] A. van Oudenaarden, M. H. Devoret, Y. V. Nazarov, and J. E. Mooij. Magneto-electric Aharonov-Bohm effect in metal rings. *Nature*, 391(6669):768–770, 1998.

[68] R. Crook, C. G. Smith, C. H. W. Barnes, M. Y. Simmons, and D. A. Ritchie. Imaging diffraction-limited electronic collimation from a non-equilibrium one-dimensional ballistic constriction. *J. of Phys.: Condens. Matter*, 12(8):L167–L172, 2000.

[69] R. Crook, C. G. Smith, M. Y. Simmons, and D. A. Ritchie. Imaging cyclotron orbits and scattering sites in a high-mobility two-dimensional electron gas. *Phys. Rev. B*, 62(8), 2000.

[70] M. A. Topinka, B. J. LeRoy, S. E. J. Shaw, E. J. Heller, R. M. Westervelt, K. D. Maranowski, and A. C. Gossard. Imaging coherent electron flow from a quantum point contact. *Science*, 289(5488):2323–2326, 2000.

[71] B. J. LeRoy, M. A. Topinka, R. M. Westervelt, K. D. Maranowski, and A. C. Gossard. Imaging electron density in a two-dimensional electron gas. *Appl. Phys. Lett.*, 80(23):4431–4433, 2002.

[72] R. M. Westervelt, M. A. Topinka, B. J. LeRoy, A. C. Bleszynski, S. E. J. Shaw, E. J. Heller, K. D. Maranowski, and A. C. Gossard. Imaging coherent electron flow in a two-dimensional electron gas. *Physica E*, 18(1-3):138–140, May 2003.

[73] R. Crook, C. G. Smith, A. C. Graham, I. Farrer, H. E. Beere, and D. A. Ritchie. Imaging fractal conductance fluctuations and scarred wave functions in a quantum billiard. *Phys. Rev. Lett.*, 91(24), 2003.

[74] R. Akis, D. K. Ferry, and J. P. Bird. Wave function scarring effects in open stadium shaped quantum dots. *Phys. Rev. Lett.*, 79(1):123–126, Jul 1997.

[75] http://www.iemn.univ-lille1.fr/ Oct, 2007.

[76] http://www.uclouvain.be/ Oct, 2007.

[77] B. Hackens. *Coherent and ballistic transport in InGaAs and Bi mesoscopic devices*. PhD thesis, Université Catholique de Louvain, 2005.

[78] G. Farhi G. Faniel C. Gustin B. Hackens, J.P. Minet and V. Bayot. Weak antilocalization and ucfs in an open bismuth quantum dot. *Phisica E*, 17:156–158, April 2003.

[79] P. Swinehart S. Courts. Review of cernox^{TM} (zirconium oxynitride) thin-film resistance temperature sensors. In AIP Conference Proceedings, editor, *Temperature: Its Measurement and Control in Science and Industry*, volume VII, pages 393–398. American Institute of Physics, 2003.

[80] B. Hackens, F. Martins, T. Ouisse, H. Sellier, S. Bollaert, X. Wallart, A. Cappy, J. Chevrier, V. Bayot, and S. Huant. Imaging and

controlling electron transport inside a quantum ring. *Nat. Phys.*, 2(12):826–830, Dec 2006.

[81] F. Martins, B. Hackens, M. G. Pala, T. Ouisse, H. Sellier, X. Wallart, S. Bollaert, A. Cappy, J. Chevrier, V. Bayot, and S. Huant. Imaging electron wave functions inside open quantum rings. *Phys. Rev. Lett.*, 99(13):136807, 2007.

[82] A. Yacoby, U. Sivan, C. P. Umbach, and J. M. Hong. Interference and dephasing by electron-electron interaction on length scales shorter than the elastic mean free path. *Phys. Rev. Lett.*, 66(14):1938–1941, Apr 1991.

[83] M. Pala and G. Iannaccone. Statistical model of dephasing in mesoscopic devices introduced in the scattering matrix formalism. *Phys. Rev. B*, 69(23):235304, 2004.

[84] K. Hess M. Macucci. Conditions for the additivity of conductance for parallel mesoscopic constrictions. *Phys. Rev. B*, 46(23):15357–15364, Dec 1992.

[85] J-C Weeber C. Chicane T. David A. Dereux G. Colas des Francs, C. Girard and D. Peyrade. Optical analogy to electronic quantum corrals. *Phys. Rev. Lett.*, 86(21):4950–4953, May 2001.